COMPUTATIONAL STUDIES OF THE ELECTRONIC STRUCTURES AND MECHANISMS OF LATE TRANSITION METAL SYSTEMS

A Dissertation

by

AMANDA LAUREN PITTS

Submitted to the Office of Graduate and Professional Studies of
Texas A&M University
in partial fulfillment of the requirements for the degree of

DOCTOR OF PHILOSOPHY

Chair of Committee,	Michael B. Hall
Committee Members,	Timothy R. Hughbanks
	Oleg V. Ozerov
	Perla B. Balbuena
Head of Department,	David H. Russell

December 2013

Major Subject: Chemistry

ABSTRACT

Late transition metal species are heavily studied because of their diverse applications in industrial, synthetic, and biological processes. Transition metals can alter the thermodynamic aspects of a reaction by creating an alternative, lower-energy pathway, which is not accessible without a metal. Numerous investigations have been performed to better understand the elementary steps within these reactions. The significant increase in available computing power coupled with the further development of transition-metal friendly quantum chemical methods has assisted in making computational chemistry an important method in predicting transition-metal mechanisms. This dissertation is divided into four parts, one for each of the transition-metal systems that were studied.

The first system focuses on the formation of a carbon-bromine bond from the reaction of Ni(Ar)(Br)(pic) (Ar = 2-phenylpyridine, pic = 2-picoloine) with Br_2. Unlike the typical behavior of heavier group 10 metals that have a wider range of stable oxidation states, Ni was found to undergo a change multiplicity during this reaction. The mechanism proceeds through a triplet state pathway that is stabilized by a Br_2^-/Ni^{III} interaction instead of the Ni^{IV} singlet state pathway. The second two systems are concerned with inter- and intramolecular carbon-hydrogen bond activation, respectively. In the second system the lifetimes of carbon-hydrogen activation of four cycloalkanes with the Cp'Rh(CO) fragments (Cp'= η^5-C_5H_5 or η^5-C_5Me_5) were calculated. The lifetimes were found to be dependent of the size of the cycloalkane reacting and the

number of possible reaction paths associated with the specific cycloalkane. A intramolecular carbon-hydrogen bond activation mechanism was calculated for the $Ru^{II}(SC_6H_3Me_2\text{-}2,6\text{-}\kappa^1S)_2(PMe_3)_3$ species for the third system. The dominant pathway was predicted to be the equatorial mechanism which proceeds through a σ-bond metathesis reaction. The final transition-metal system involves the transfer of Cu^I from the Atox1 metal binding site to a metal binding domain on the ATP7A or ATP7B proteins. This system was found to proceed through a dissociative pathway wich each two-coordinate and three-coordinate species stabilized by adopting the optimized the S lone pair/Cu 3d π-overlap.

ACKNOWLEDGEMENTS

I would first like to thank my advisor, Dr. Michael Hall, for his guidance in both chemistry and life over the past four years. He was always available to help solve my latest chemistry problem even if he was out of the office. I believe it will be very hard for me to find another advisor who is as genuinely invested in my understanding and appreciation of chemistry as he is.

I would also like to thank Dr. Lisa Perez who also helped me become the chemist that I am today. I thank her for her patience in my first year of graduate school and her willingness to continually help me as I moved on through the years.

A special thanks to my friends Monica Gonzales, Sam Timpa, Jill Davidson, and Jacob Bloom for supporting me during both the good and the frustrating times of graduate school. Thank you for lending an ear on each coffee trip and for helping me through my hardest benchmarks in graduate school. Thank you to my brother who helped me with scripts throughout my four years and reminded me that learning to code would be good for me. Also, thank you to the many group members of the Hall group that have come and gone throughout my tenure and the only one who has been with me the whole time, Zhenggang Xu.

Finally, thank you to my husband Derek who supported me through the last years in my degree. Thank you for listening to me talk about my chemistry projects endlessly and for giving me the opportunity to see where this degree can take me.

TABLE OF CONTENTS

Page

ABSTRACT…… ii

ACKNOWLEDGEMENTS…… iv

TABLE OF CONTENTS…… v

LIST OF TABLES……... viii

LIST OF FIGURES…….. ix

CHAPTER I INTRODUCTION…….. 1

1.1 Introduction…… 1
1.2 Computational Methods…….. 4
1.2.1 Schrödinger Equation…… 4
1.2.2 Hartree-Fock Theory……..... 6
1.2.3 Variational Methods…….. 12
1.2.4 Perturbation Methods…… 13
1.2.5 Coupled-cluster Methods…….. 15
1.2.6 Density Functional Theory……... 16

CHAPTER II NICKEL INDUCED CARBON-BROMINE BOND FORMATION IN A SPIN-CROSSING MECHANISM…….. 21

2.1 Introduction……..... 21
2.2 Computational Details…… 24
2.2.1 Functionals and Basis Sets…….. 24
2.2.2 Calibration and Methodology…….. 25
2.3 Results and Discussion……... 27
2.4 Conclusion……..... 47

CHAPTER III CARBON-HYDROGEN ACTIVATION OF CYCLOALKANES WITH CYCLOPENTADIENYLCARBONYLRHODIUM - A LIFETIME ENIGMA..... 49

3.1 Introduction..... 49
3.2 Computational Details……... 52

3.2.1 Methods…….. 53
3.2.2 Chemical Kinetics Simulator…….. 54
3.3 Results and Discussion…….. 55
3.3.1 Reaction Scheme…… 55
3.3.2 Reactants…… 56
3.3.3 CpRh(CO) Reactions…….. 59
3.3.4 Cp*Rh(CO) Reactions…… 72
3.4 Mechanisms……... 74
3.4.1 Static Mechanism…… 74
3.4.2 Migration Mechanism..... 78
3.5 Conclusion..... 80

CHAPTER IV INTRAMOLECULAR CARBON-HYDROGEN BOND ACTIVATION OF *BIS*(2,6-DIMETHYLBENZENETHIOLATO)TRIS(TRIMETHYLPHOSPHINE) RUTHENIUM(II)…….. 82

4.1 Introduction…….. 82
4.2 Computational Details…….. 86
4.3 Results and Discussion…… 87
4.3.1 $Ru^{II}(SC_6H_3Me_2\text{-}2,6\text{-}\kappa^1S)_2(PMe_3)_3$……... 87
4.3.2. Reaction Mechanisms……... 91
4.3.3 Solvent Influence……... 107
4.4 Conclusion……..... 112

CHAPTER V CALCULATING A COPPER(I) TRANSFER MECHANISM FOR ATOX1 WITH DENSITY FUNCTIONAL THEORY…….. 115

5.1 Introduction……... 115
5.2 Computational Details……... 119
5.3 Results and Discussion…….. 121
5.3.1 $[Cu(I)(SCH_3)_2]^{1-}$…….. 121
5.3.2 $[Cu(I)(SCH_3)_3]^{2-}$……..... 125
5.3.3 $[Cu(I)(SCH_3)_4]^{3-}$……. 126
5.3.4 Transfer Mechanism……... 127
5.5 Conclusion…… 133

CHAPTER VI CONCLUSION…….. 135

6.1 Conclusion…… 135

6.2 Future Work…….. 137

REFERENCES……... 138

APPENDIX A…… 148

APPENDIX B…… 162

APPENDIX C…… 171

APPENDIX D…… 173

LIST OF TABLES

Table		Page
2.1.	Experimental Values and Theoretical Values from Complex 1^S Bond Lengths (Å) and Angles (°)..……	29
2.2.	Calculated Relative Gas-Phase Electronic Energies, Enthalpies, Free Energies and Solvent Corrected Free Energies (kcal/mol) for Singlet PES...	32
2.3.	Calculated Relative Gas-Phase Electronic Energies, Enthalpies, Free Energies and Solvent Corrected Free Energies (kcal/mol) for Triplet PES...	33
3.1.	DFT Calculated Free Energies for the Cyclohexane Reaction with CpRh(CO)……..	53
3.2.	Bond Distances Between Rh and Ligands on CpRh(CO) and Cp*Rh(CO)...	58
3.3.	Bond Distances for C-H Bonds in the Separated Cycloalkanes……..	61
3.4.	Relative Free Energies (kcal/mol) for the Seven σ-complexes in the Cycloheptane Reaction…….……	67
3.5.	Experimental and Calculated Lifetimes (ns) for the Migration and Static Mechanisms……	76
4.1.	The Bond Distances (Å) and Angles (°) of the Crystal Structure and Calculated Geometry of Complex 1……..……..	89
4.2.	Electronic Energies, Enthalpies, and Free Energies for the Axial and Equatorial Mechanisms……..	94
4.3.	Bond Distances (Å) and Angles (°) for Complex 1 Optimized in the Gas Phase and in Methanal…….....	111

LIST OF FIGURES

Figure		Page
2.1.	The Closed Shell, Square Planar BP86 Geometry of Complex $\mathbf{1}^{S}$……	28
2.2.	Solvated Free Energy Diagram. The Lowest Energy Structures are Shown for Each Intermediate or Transition State.……	30
2.3.	The Singlet and Triplet State Structures of Complex **2**...……..	34
2.4.	The Antibonding (LUMO), Non-bonding (HOMO-4), and Bonding (HOMO-21) Molecular Orbitals of the 3-center, 4-electron Bond Formed in $\mathbf{2}^{S}$.……	35
2.5.	Singly Occupied Molecular Orbital (SOMO) and Spin Density of $\mathbf{2}^{T}$……	37
2.6.	The Singlet and Triplet State Geometries for **3-TS**..……...	38
2.7.	SOMOs and Spin Density of $\mathbf{3}^{T}$**-TS**……	39
2.8.	The Singlet State Geometry of $\mathbf{4}^{S}$……	41
2.9.	Geometry of $\mathbf{4}^{T}$. Bond Distances (Å)……..	42
2.10.	Geometries of Intermediate $\mathbf{6}^{T}$ and Transition State $\mathbf{7}^{T}$**-TS**……	44
2.11.	Geometries of Intermediates $\mathbf{8}^{S}$ and $\mathbf{8}^{T}$……..…	45
2.12.	Structures $\mathbf{9}^{S/T}$ and **10**……...……	46
2.13.	Structures of Final Products $\mathbf{11}^{S}$ and $\mathbf{11}^{T}$……	48
3.1.	Optimized Geometries for the CpRh(CO) and Cp*Rh(CO) Fragments...…..	57
3.2.	The Lowest Energy Confirmations for Each Cycloalkane……	60
3.3.	Cyclopentane Only Activates One Unique C-H Bond…...……	62
3.4.	The Optimized Geometries for the Cyclohexane Reaction with CpRh(CO).…….....	64
3.5.	The Most Stable and the Least Stable Cycloheptane σ-complexes……	66

3.6. (a) The 1,1-migration, a Transfer Between the Two Hydrogen Atoms on One Carbon. (b) The Inside 1,2-migration a Transfer Between Two Adjacent C-H Bonds with a H-C-C-H Dihedral Angle Less than 60°. (c) The Outside 1,2-migration, a Transfer Between Two Adjacent C-H Bonds with a H-C-C-H Dihedral Angle Larger than 60°. (d) The 1,3-migration and (e) 1,4-migration is a Transfer Across the Face of the Cycloalkane….. 69

3.7. A Side and Top View of the Highest Energy Cycloheptane (a) and Cyclooctane (b) σ-complexes are Shown to Compare the Steric Crowding Between the Cycloalkane and the Rh Fragment…..…….. 71

3.8. Comparison of the Cyclohexane Reaction with CpRh(CO) and Cp*Rh(CO)……...…… 73

3.9. Calculated Lifetimes for the Four Cycloalkane Reactions with CpRh(CO)…… 77

3.10. Calculated Lifetimes for the Four Cycloalkane Reactions with Cp*Rh(CO)……..…… 79

4.1. The Calculated Gas Phase Structure for Complex **1** Which Optimized to a Distorted Trigonal Bipyramidal Geometry…… 88

4.2. Calculated Geometry for Complex **1** and its Electronically Equivalent Mirror Image Complex, **1'**…….…… 92

4.3. Free Energy Axial and Equatorial Reaction Mechanism..…….. 93

4.4. In Complex **1** the Axial S LP is Interating with an Occupied Ru 4d Orbital (HOMO) While the Equatorial S LP is Interacting with an Unoccupied Ru 4d orbital (LUMO)……...…….. 96

4.5. In the Axial Mechansim C(5) Activates Because C(8) is Not Sterically Hindered by P(2)Me_3, but C(3) Does Not Activate Because C(10) is Sterically Hindered by the P(1)Me_3 Ligand. In the Equatorial Mechanim C(10) Activates Because C(5) is Not Sterically Hindered by P(1)Me_3, but C(8) Does Not Activate Because C(3) is Sterically Hindered by the P(2)Me_3 ligand…… 97

4.6. The Frontier Orbitals of Complex **1** and $\mathbf{2}^{\mathbf{A\text{-}TS}}$..……..... 100

4.7. The Calculated Geometries of Intermediate $\mathbf{5}^{\mathbf{A}}$, $\mathbf{6}^{\mathbf{A\text{-}TS}}$, and $\mathbf{7}^{\mathbf{A}}$..……..... 101

4.8. The Frontier Orbitals for $\mathbf{5}^{\mathbf{A}}$, $\mathbf{6}^{\mathbf{A\text{-}TS}}$, and $\mathbf{7}^{\mathbf{A}}$..……..... 103

4.9. Calculated Geometry of Intermediate $\mathbf{7^E}$, σ-bond Metathesis Transition State $\mathbf{8^{E\text{-}TS}}$ and Intermediate $\mathbf{9^E}$……..…… 106

4.10. Calculated Geometires for the Explicit Solvent Method....…… 108

4.11. Calculated Geometies of Complex **1** Optimized in Methanol, $\mathbf{1_{ML}}$, and Benzene, $\mathbf{1_{BL}}$....……..……..…… 110

4.12. Calculated Geometies of $\mathbf{1_{ML}}$ with Explicit Methanol Molecules Interacting with the Open Binding Site on the Distorted Square-Based Pyramidal Geometry...…….. 114

5.1. The Calculated Minimum Energy Geometries for the Cu(I) Methylthiolate Model Complexes...……..... 122

5.2. The Potential Energy for the Scan of the C-S-S-C Dihedral Angle of $[Cu(SCH_3)_2]^{-1}$…….. 123

5.3. Molecular Orbital Diagrams for the 2-coordinate Methylthiolate Copper Complexes....…… 124

5.4. The Optimized Geometries for the Doubly Anionic Diasteromers (a) R,R and (b) R,S Confirmations of the DTT Ligand...……..…….. 129

5.5. Enthalpy Surface for the Transfer of Cu(I) from the Atox1 Binding Site Model to the DTT Ligand..…… 130

CHAPTER I

INTRODUCTION

1.1 Introduction

Late transition metal species are extensively studied because of their diverse applications in industrial, synthetic, and biological processes.[1] Transition metals can alter the kinetics of a reaction by creating an alternative, lower-energy pathway, which is not accessible without the metal. Examples of this catalytic prowess of transition metal systems are highlighted in enzymatic reactions,[2] hydrocarbon bond functionalization reactions,[3] and small molecule activations.[4] Significant increases in available computing power coupled with the development of quantum chemical methods suitable for transition metals has increased the size of systems that can be studied by computational means.[5] The details of transition metal reaction mechanisms and electronic structure can now be accurately predicted, which has benefitted our understanding of chemical problems that could not have been elucidated previously by experimental methods alone. Here, the electronic structure, bonding, thermodynamics, and kinetics of four different late transition metal systems are investigated with density functional theory to predict transition states and intermediates along possible reaction paths and used to determine the most plausible mechanism.

Due to the abundance and low cost of hydrocarbons, the synthesis of organic starting materials from simple hydrocarbon such as alkanes is of great importance. With the help of transition metal complexes C-H and C-C bonds and can converted into C-X,

where X is a heteroatom, bonds that can then be directly consumed as starting materials for 'value-added' products. One such reaction, which involves a nickel(II)-induced Ar-Br bond formation, is the first system studied in this work.[6] Unlike the typical behavior of their second and third row counterparts, the first row transition metals have smaller d orbital splitting energies, so high spin complexes are common. For the reaction of Ni(Ar)(Br)(pic) (Ar = 2-phenylpyridine, pic = 2-picoloine) with Br_2 density functional theory predicts that the nickel center undergoes a change in multiplicity to provide a low energy path for the reaction. The spin-crossing mechanism was calculated for the overall reaction and used to compare the thermodynamic properties of the two reaction surfaces.[7]

The second system studied here maintains the theme of bond functionalization at a metal center, but is focused on the details of oxidative addition instead of reductive elimination. The C-H bond activation of four cycloalkanes (C_5H_{10}, C_6H_{12}, C_7H_{14}, and C_8H_{16}) with Cp'Rh(CO) fragments (Cp' = η^5-C_5H_5 or η^5-C_5Me_5) was theoretically modeled and the calculated lifetimes were compared to the fast time-resolved infrared spectroscopic lifetimes. The reaction was previously assumed to proceed through a basic, two-step process, starting with the formation of a σ-complex intermediate and followed by oxidative addition. However, a more elaborate migration mechanism was also predicted to contribute to lifetimes. Both oxidative-addition and migration steps were calculated to determine which contributed most to hydrocarbon lifetimes.[8]

Carbon-hydrogen activation was again examined in the third transition metal system presented here with an emphasis on intramolecular instead of intermolecular C-H

activation. In this study the mechanistic details of the intramolecular C-H activation of the $Ru^{II}(SC_6H_3Me_2\text{-}2,6\text{-}\kappa^1S)_2(PMe_3)_3$ complex that was experimentally studied by Komiya and coworkers was computationally explored.[9] The intramolecular activation of an ortho methyl group on one of the 2,6-dimethylbenzenethiolato ligands occurred at room temperature and pressure in ~30 minutes in benzene and yielded the C-H activated product *cis*-$Ru[SC_6H_3\text{-}(2\text{-}CH_2)(6\text{-}Me)\text{-}\kappa^2S_2C](PMe_3)_4$. However, a change in solvent from benzene to methanol prevents the activation of the ortho methyl group and an the six-coordinate $Ru(SC_6H_3Me_2\text{-}2,6\text{-}\kappa^1S)_2(PMe_3)_4$ complex is formed. The reaction's mechanistic details and the product's dependence on the reaction medium were determined along with the electronic structure of the inactivated and activated octahedral products.

Copper, the third most abundant metal in the human body, is essential for proper function, and is the basis for the fourth portion of this work. Copper(I) is required for many chemical reactions, however, as an uncomplexed ion Cu(I) is highly reactive and potentially fatal to living cells, so understanding how the body maintains proper copper homeostasis is important in preventing or curing diseases associated with a build up or lack of copper.[10] In this study, three Cu(I) methylthiolate model complexes, $[Cu(SCH_3)_2]^{-1}$, $[Cu(SCH_3)_3]^{-2}$, $[Cu(SCH_3)_4]^{-3}$, were investigated to determine the bonding and electronic structure of these electron-rich systems. These conclusions were then applied to the calculation of the Cu(I) transfer from a truncated Atox1 metallochaperone to a model for the metal binding domain of the ATP7A or ATP7B proteins. The Atox1 Cu(I) binding site was modeled by abbreviating the full protein to the Cys-Gly-Gly-Cys

binding site, and the dithiotreitol ligand (DTT) was used as a model for the acceptor's metal binding domain.[11]

Treatment of these four systems with quantum chemical methods entails the calculation of reactants, products, and the critical points along each reaction mechanism. The accuracy of these calculations not only affects the optimized geometry of each species, but also the thermodynamics and kinetics of the overall reaction. Balancing chemical accuracy with computational cost is a critical part of a computational investigation, and because of its importance, a brief background on computational methods and basis sets is presented before delving into the details of the four chemical systems.

1.2 Computational Methods

1.2.1 Schrödinger Equation

The time-independent, non-relativistic Schrodinger equation is the basis for most quantum chemical electronic structure methods

$$\hat{H}\Psi = E\Psi, \tag{1}$$

where the Hamiltonian operator, $\hat{H}$, is equal to

$$\hat{H} = (T + V). \tag{2}$$

In equation (2) the first term represents the kinetic energy of the system, the second term is the potential energy, Ψ is the wavefunction, and E is the energy of the system. For the one-electron, hydrogen-like atomic system, the Schrodinger equation becomes

$$\left(-\frac{1}{2}\nabla_1^2 - \frac{Z_A}{r_1}\right)\Psi = E\Psi, \tag{3}$$

where the Hamiltonian is separated into the kinetic energy of the electron and the potential is coulombic, where r_1 is the distance between the nucleus and the electron, Z_A is the charge on the nucleus, and Ψ is atomic wavefunction. The Schrödinger equation for hydrogen and hydrogen-like atoms can be solved exactly because the variables can be separated and each of the three equations for the three coordinates can be solved independently. With the wavefunction appropriately defined, the total energy of the hydrogen atom can then be calculated. For chemical systems with more than one electron, the Schrödinger equation cannot be analytically solved because the variables are no longer separable. As shown in the equation for the helium atom,

$$\left(-\frac{1}{2}\nabla_1^2 - \frac{1}{2}\nabla_2^2 - \frac{Z_A}{r_1} - \frac{Z_A}{r_2} + \frac{1}{r_{12}}\right)\Psi = E\Psi. \tag{4}$$

The $1/r_{12}$ term prevents the separation of the equation into two solvable one-electron equations, so beyond the hydrogen atom and a few other one-electron systems, the Schrödinger equation is approximately solved.

1.2.2. Hartree-Fock Theory

The general Hamiltonian for a many-electron system, where *i* and *j* represent electrons and *A* and *B* represent nuclei, is given by

$$\hat{H} = -\sum_i \frac{1}{2}\nabla_i^2 - \sum_A \frac{1}{2}\nabla_A^2 - \sum_i \sum_A \frac{Z_A}{r_{iA}} + \sum_{i<j} \frac{1}{r_{ij}} + \sum_{A<B} \frac{Z_A Z_B}{r_{AB}}, \tag{5}$$

which is composed of the electrons' kinetic energy, the nuclei's kinetic energy, the nuclear-electronic attraction, the electron-electron repulsion, and the nuclear-nuclear repulsion. The first approximation made toward a solution is the Born-Oppenheimer approximation, which separates the nuclear-nuclear repulsion term from the electronic terms. These terms can be approximately separated because, with respect to the electrons, the nuclei in a system are moving slowly. Thus, one calculates the solution to the electronic motion with static nuclei with the electronic Hamiltonian:

$$\hat{H}_{el} = -\sum_i \frac{1}{2}\nabla_i^2 - \sum_i \sum_A \frac{Z_A}{r_{iA}} + \sum_{i<j} \frac{1}{r_{ij}}. \tag{6}$$

The nuclear-nuclear repulsions are calculated separately and then added to the electronic energy, which together becomes the potential energy in which the nuclei move.

The calculation of a system's wavefunction was initially approached by Hartree, who used the product of one-electron wavefunctions to write an approximate polyelectron wavefunction:

$$\Psi(r_1,r_2,r_3,...,r_n) = \psi_1(r_1)\psi_2(r_2)\psi_3(r_3)..\psi_n(r_n). \tag{7}$$

However, the Hartree product wavefunction suffers because it does not obey the Pauli Principle, the wavefunction is not antisymmetric with respect to exchange of the electrons. These deficiencies are corrected in the Hartree-Fock method (HF) by describing the wavefunction with a Slater determinant:

$$\Psi_{2n} = \frac{1}{\sqrt{(2n)!}} \begin{vmatrix} \psi_1(1)\alpha(1) & \psi_1(1)\beta(1) & \psi_2(1)\alpha(1) & \cdots & \psi_n(1)\beta(1) \\ \psi_1(2)\alpha(2) & \psi_1(2)\beta(2) & \psi_2(2)\alpha(2) & \cdots & \psi_n(2)\beta(2) \\ \vdots & \vdots & \vdots & \cdots & \vdots \\ \psi_1(2n)\alpha(2n) & \psi_1(2n)\beta(2n) & \psi_2(2n)\alpha(2n) & \cdots & \psi_n(2n)\beta(2n) \end{vmatrix}, \tag{8}$$

where the elements account for the spatial orbitals, *n*. The Slater determinant ensures that there are only two electrons in each spatial orbital and that the wavefunction is antisymmetric with respect to exchange. Each spatial orbital element, also known as molecular orbitals (MO) when being applied to a molecular system, is a linear combination of atomic orbitals, which are described by basis functions.

Currently, the most commonly used functions to describe atomic orbitals in the Slater determinant are Slater and Gaussian functions. Slater functions are defined as

$$\phi_s = Nr^{n-1}e^{-\varsigma r}Y_l^m(\theta,\phi), \tag{9}$$

whereas Gaussian functions are defined as

$$\phi_s = Nr^{(2n-2-l)}e^{-\varsigma r^2}Y_l^m(\theta,\phi). \tag{10}$$

Although Slater functions more accurately describe the shape of the atomic orbitals, they are implemented less in computational software because the mathematics of the two-electron integrals is significantly more complicated then that of Gaussian functions. Because Gaussian functions are less accurate in describing chemical aspects more Gaussian functions are needed to equate to one Slater function. An example of this is shown in the STO-3G basis set, which signifies that three Gaussian functions are being used to describe one Slater function for the specified atom. For the chemical systems in this dissertation Pople-type basis sets, which utilize Gaussian functions, are mainly used.

When calculating transition metal systems, the core electrons of the transition metals are often replaced by an effective core potential (ECP). This is done for two reasons, to reduce the overall number of two-electron integrals, and to include relativistic effects into the calculation. An ECP replaces the two-electron integrals that stem from the interaction between the valence and core electrons with a one-electron

operator that takes into account the complete interaction between these two sets of electrons. This can be effectively implemented because the core electrons are less involved in the chemistry in a system. An ECP includes relativistic effects on the effect of the core electrons on the shape of the valence orbitals by including the mass-velocity and Darwin corrections of the core electrons, but it cannot represent the spin-orbit coupling of the valence electrons. For this dissertation the respective fully-relativistic Stuttgart ECP is applied to each metal and is coupled with the double- or triple-ζ Stuttgart basis set, depending on the computational efficiency required.

Returning back to the single Slater determinant molecular wavefunction in equation (8), as defined in quantum theory, one could calculate any physical observable of the system by applying the appropriate operator to the wavefunction. However, a method for determining a molecular wavefunction for a specific system is not as concisely defined, but, as previously stated, the wavefunction can be described by a Slater determinant where each element is a MO described by a linear combination of atomic orbitals. The energy of a trial wavefunction can then be calculated by

$$E = \frac{\int \Psi^* \hat{H} \Psi d\tau}{\int \Psi^* \Psi d\tau}, \tag{11}$$

According to the variation principle, which states that for a wavefunction, which depends on certain parameters, the parameters can be varied until the energy of the system reaches a minimum. This theorem ensures that any variationally calculated

energy of a system will be greater than the true energy because, in practice, any wavefunction inserted into equation (11) is an approximation of the true wavefunction. In practice, a wavefunction with a lower energy in a better wavefunction.

The MOs that comprise the Slater determinant in HF theory can be varied independently of each other to determine the minimum electronic energy. Since they can be separated, a system of equations can be used to minimize the energy of each MO, and therefore the total electronic energy for the system. This system of equations are referred to as the HF equations, which have the form

$$\hat{F}\psi_i = \varepsilon_i\psi_i, \tag{12}$$

where $\hat{F}$ is the Fock operator:

$$\hat{F} = \hat{H}^{core} + \sum_{j=1}^{n}(2\hat{J}_j - \hat{K}_j), \tag{13}$$

ψ_n is a specific MO and ε_n is the energy of the MO. The first term in equation (13) includes the electron's kinetic energy and the potential energy from the electron's attraction to the nuclei.

$$\hat{H}^{core} = -\frac{1}{2}\nabla^2 - \sum_{A=1}^{M}\frac{Z_A}{r}, \tag{14}$$

The second term incorporates the electron-electon interactions with the coulomb and exchange integrals. The coulomb integral represents the electrostatic repulsion between an electron in ψ_i and an electron in ψ_j:

$$J_{ij} = \int \psi_i^*(1)\psi_j^*(2)\left(\frac{1}{r_{12}}\right)\psi_i(1)\psi_j(2)dv_1 dv_2 \tag{15}$$

.

The exchange integral arises mathematically from the antisymmetric character of the wavefunction:

$$K_{ij} = \int \psi_i^*(1)\psi_j^*(2)\left(\frac{1}{r_{12}}\right)\psi_i(2)\psi_j(1)dv_1 dv_2 \tag{16}$$

.

The total Hartree-Fock electronic energy is therefore calculated by:

$$E_{HF} = 2\sum_{i=1}^{n} H_{ii} + \sum_{i=1}^{n}\sum_{j=1}^{n}(2J_{ij} - K_{ij}) \tag{17}$$

,

where there are *n* filled MOs and *2n* electrons in the system. The total energy is not calculated by simply summing the individual MO energies because then each electron-

electron interaction would be counted twice, since each orbital energy includes the repulsion with all the other electrons. Instead, as shown in equation (17), the double-counting is corrected by subtracting the superfluous electron-electron interactions from the sum.

Since Hartree-Fock (HF) theory[12] uses a single Slater determinant to describe the wavefunction of a system, it does not correlate the motion of the electrons with opposite spins (these electrons are not prevented from being in the same place at the same time by the form of the wavefunction), but the antisymmetric property of the Slater determinant does incorporate some correlated motion for electrons of the same spin, which is called exchange correlation. Post-HF theory calculations incorporate electron correlation for all the electrons traditionally through configuration interaction, which can be divided into three categories depending on the utilized approach, variational methods, perturbation methods, and coupled cluster methods. All three of these methods will be described herein.

1.2.3 Variational Methods

Traditionally, the variational approach to configuration interaction (CI) describes the wavefunction of a system as a linear combination of Slater determinants:

$$\Psi = a_0\Psi_{HF} + \sum_{i}^{occ.}\sum_{r}^{vir.} a_i^r\psi_i^r + \sum_{i<j}^{occ.}\sum_{r<s}^{vir.} a_{ij}^{rs}\psi_{ij}^{rs} + ... \qquad (18)$$

In equation (20) *i* and *j* are occupied MOs in the Hartree-Fock reference wavefunction, Ψ_{HF}, and *r* and *s* are virtual MOs in Ψ_{HF}, thus the second term in equation (20) includes all of the single electronic excitations and the third term includes all of the double electronic excitations, etc. Describing the wavefunction of a system in this manner adds electron correlation for electrons with opposite spin, which is not included in the HF method. A full CI calculation would be the most accurate theoretical method, but the computational cost associated with this type of calculation is too large for all but the smallest molecules, so truncated versions of the full CI method, which include only the single, double, or triple excitations are normally used. Other variational methods include more than just the Hartree-Fock reference wavefunction. These methods are referred to as multireference methods and include multireference CI (MRCI), multiconfigurational SCF (MCSCF), and complete active space SCF (CASSCF).

1.2.4 Perturbation Methods

Perturbation methods incorporate electron correlation by separating the electronic Hamiltonian into two pieces:

$$\hat{H} = \hat{H}_0 + \lambda \hat{H}', \tag{19}$$

where the first term is the unperturbed Hamiltonian for which one has an exact solution, and the second term is the perturbed Hamiltonian. The Møller-Plesset method,[13] MPX, where X stands for the order of the correction, is the most commonly used perturbation

method. The MP approach sets $H^{(0)}$ equal to the sum of the one-electron Fock operators. The zero-order electronic energy, $E^{(0)}$, counts each electron-electron repulsion twice, since each orbital energy includes the repulsion with all the other electrons. This error is corrected with the first order correction, $H^{(1)}$, which removes the double-counted electron-electron repulsions, therefore the energy calculated through the first-order correction is equal to the Hartree-Fock energy. The second-order energy correction, MP2, moves beyond the Hartree-Fock energy and incorporates correlation energy into the given system by including double electronic excitations from the reference Ψ_{HF} to virtual orbitals in Ψ_{HF}. For a two-electron/two-orbital system

$$E^{(2)} = \frac{\left[\int\int \psi_1(1)\psi_1(2)\frac{1}{r_{12}}\psi_2(1)\psi_2(2)dv_1dv_2\right]^2}{2(\varepsilon_1 - \varepsilon_2)}, \qquad (20)$$

where ψ_1 is the doubly occupied orbital the two electrons are being promoted from, ε_1 is the energy of this occupied orbital, ψ_2 is the unoccupied orbital in which they are being promoted, and ε_2 is the energy of the unoccupied orbital. For systems larger than two-electron/two-orbital the energies of all the second-order excitations are summed. MP3 corrections include only double excitations also, but the doubly excited states interact with one another in MP3 whereas for MP2 excited states only interact with the ground state. Fourth-order perturbation, MP4, can include single, double, triple, and quadruple excitations depending on the specific calculation chosen. All three of these methods are

used in this work, and are compared to higher level *ab initio* calculations and density functional theory (DFT) calculations.

1.2.5 Coupled-cluster Methods

Coupled-cluster methods[14] account for electron correlation by including a series of excitation operators that act on the HF wavefunction. The general form of couple-cluster theory is defined as

$$\Psi_{CC} = e^{\mathbf{T}}\Psi_{HF}. \tag{21}$$

The operator **T** is defined as

$$\mathbf{T} = \mathbf{T}_1 + \mathbf{T}_2 + \mathbf{T}_3 + \ldots + \mathbf{T}_n \tag{22}$$

where n is the number of electrons in the system and each $\mathbf{T}_i$ operator generates all the possible i excitations. Using $\mathbf{T}_2$ as an example yields coupled-cluster doubles (CCD):

$$\Psi_{CCD} = e^{T}\Psi_{HF} = \left(1 + \mathbf{T}_2 + \frac{\mathbf{T}_2^2}{2!} + \frac{\mathbf{T}_2^3}{3!} + \ldots\right)\Psi_{HF}. \tag{23}$$

The $\mathbf{T}_2$ operator generates double excitations while the square of $\mathbf{T}_2$ generates related quadruple excitations and the cube of $\mathbf{T}_2$ generates related sextuple excitations and so on. CCD is equivalent to taking the double excitations to infinite order of perturbation theory. Coupled-cluster singles and doubles with perturbative triples (CCSD(T)) is widely used for benchmarking energies of systems because it calculates highly accurate electronic energies when paired with a large basis set.

1.2.6 Density Functional Theory

Using only the ground-state electron density to exactly predict the properties of many-electron systems without deriving an appropriate wavefunction was the initial aspiration of DFT. Until the Kohn-Sham implementation of DFT,[15] where orbitals were introduced into the theory, the application of DFT to chemical problems was not largely successful. The reason for the failure of orbital-free methods was that they gave a poor representation of the kinetic energy. However, the Kohn-Sham formulation corrects the calculation of the kinetic energy by separating the ground state density, $\rho(\mathbf{r})$, for any real system into two parts, interacting and non-interacting. Where $\rho(\mathbf{r})$ for a system with ϕ_i orbitals and N electrons is calculated by

$$\rho = \sum_{i=1}^{Nelec} |\phi_i|^2 . \tag{24}$$

As shown below, the non-interacting part uses the identical formulas from HF theory for the kinetic energy, the electron-nuclear potential, and the electron-electron coulombic potential, and the interacting part includes the exchange-correlation energy:

$$E_{DFT}[\rho] = T_s[\rho] + E_{ne}[\rho] + J[\rho] + E_{xc}[\rho]. \tag{25}$$

The first three terms are calculated exactly for the non-interacting system, but the last term, the exchange-correlation energy, is the interacting part defined by

$$E_{xc}[\rho] = (T[\rho] - T_s[\rho]) + (E_{ee}[\rho] - J[\rho]). \tag{26}$$

The first term in this equation contains the kinetic correlation energy, which is the correction to the HF kinetic energy, and the second term contains the exchange and correlation potential energy that is left when the non-interacting coulombic potential is subtracted. Since each term, aside from the E_{xc} term, is calculated excatly, the only difference between the various DFT functionals is the form for the E_{xc} term.

The first type of DFT functionals used ini this work are called Generalised Gradient Approximation (GGA) functionals, which inlcude electron density and its first

derivative. One of the earliest GGA functionals was proposed by A. D. Becke and was a correction for the LDA exchange functional:[17]

$$\varepsilon_x^{B88} = \varepsilon_x^{LDA} + \Delta\varepsilon_x^{B88}, \tag{27}$$

where

$$\Delta\varepsilon_x^{B88} = -\beta\rho^{1/3}\frac{x^2}{1+6\beta x\sin(h^{-1}x)}, \tag{28}$$

The B88 exchange functional can be used alone, but is normally coupled with a correlation functional to form a complete exchange-correlation functional. The most common correlation functional paired with B88 is Lee-Yang-Parr (LYP) which corrects the VWN correlation formulation:[18]

$$E_{xc}^{B88LYP} = aE_x^{LSDA} + bE_x^{B88} + (1-c)E_c^{LSDA} + cE_c^{LYP}. \tag{29}$$

There are many exchange and correlation functionals that can be coupled together to form GGA functionals. The second category of functionals are the hybrid GGA which

Incorporate a percentage of HF exchange into the exchange term of the functional. The most popular functional, to date, is the B3LYP hybrid GGA functional[18,19]:

$$E_{xc}^{B3LYP} = (1-a)E_x^{LSDA} + aE_x^{HF} + b\Delta E_x^B + (1-c)E_c^{LSDA} + cE_c^{LYP}, \qquad (30)$$

where a, b, and c are equal to 0.20, 0.72, and 0.81 respectively. The B3LYP functional is used consistently throughout the four chapters, but other hybrid GGA functionals are also used including BMK[20] and M06[21]. A third type of functionals, called meta-GGA, includes not only the first derivative of electron density but also the second derivative of the electron density or a dependence on the kinetic-energy density. Since the second derivative has numerical instabilities, many of the meta-GGA functionals only incorporate the kinetic-energy dependence. The TPSS meta-GGA functional[22] is used for several reactions herein.

The final type of DFT functionals used in this work are the dispersion-corrected functionals, which have just recently been implemented into mainstream software. Dispersion-corrected functionals correct the energy of system by adding an empirical correction to account for the electron correlations that is responsible for the London dispersion forces, the attractive part of the van der Waals interactions, to the total energy. The energy for the B97-D dispersion-corrected functional[23] is calculated by

$$E_{B97D} = E_{B97} + E_{dispersion}, \tag{31}$$

where E_{B97} is the energy from the Becke 1997 GGA functional[24] and $E_{dispersion}$ is calculated by

$$E_{dispersion} = -s_6 \sum_{i=1}^{N_{at}-1} \sum_{j=i+1}^{N_{at}} \frac{C_6^{ij}}{R_{ij}^6} f_{damp}(R_{ij}), \tag{32}$$

and N_{at} is the number of atoms in the system, C_6^{ij} is a calculated dispersion coefficient for the atom pair ij and for transition metals is the average of the C_6 coefficients for the preceding rare gas and the following group III element, s_6 is a global scaling factor that is determined by B97, R_{ij} is the interatomic distance between i and j, and f_{damp} is

$$f_{damp} = \frac{1}{1 + e^{-d(R_{ij}/R_r - 1)}} \tag{33}$$

The damping function prevents double counting of the medium- and short-range interactions in the system. A second dispersion-corrected functional is also used in this work, ωB97X-D,[25] which has nonexponential denominator for the damping function and does not include the s_6 scaling factor to calculate the dispersion energy.

CHAPTER II

NICKEL INDUCED CARBON-BROMINE BOND FORMATION IN A SPIN-CROSSING MECHANISM

2.1 Introduction

Reductive elimination of two ligands (R, R′) from a metal catalyst to form and release the new species R-R′ often completes many industrial and laboratory reactions.[26] The formation of C-C bonds by reductive elimination is a well studied process[27] that can be initiated by the oxidative addition of a C-X (X = halogen) to the metal center.[28] Although many catalytic cycles involve C-X bond activation, there has been significantly fewer studies of catalytic C-X bond forming reactions. However, metal-catalyzed formation of a C-X bond could provide facile synthetic routes to important organic halides.[29] The C-X bond forming reactions are typically supported by metals that can access a variety of oxidation states, such as ones that can be easily oxidized from II to IV and then reduced back to II by the final reductive elimination step. Group 10 metals, especially Pt and Pd, are the most commonly used transition metals for these reactions because of their variety of stable oxidation states, coordination numbers, and molecular geometries. Palladium has been shown to form C-X bonds by reductive elimination from octahedral Pd^{IV} structures,[30] trigonal planar Pd^{II} species,[31] and bimetallic Pd^{III} complexes.[32] These complexes typically involve nitrogen-carbon bidentate ligands in which the latter coordinated atom can interact with neighboring halogen ligands and reductively eliminate from the metal center. Although the bulk of

this work utilizes iodine, bromine, or chlorine, recently catalytic C-F bond forming reactions have been reported.[33] Platinum has been used less extensively, but in a like manner to Pd; Pt^{IV} octahedral complexes with similar nitrogen-containing, bidentate ligands have been shown to produce similar reductively eliminated products.[34] Milstein has also reported a C-I bond forming system using a Rh^{III} pincer-type complex.[35]

Nickel, even though it is in group 10 along with Pd and Pt, has not been utilized as often for these reactions.[36] The d orbitals of first transition row metals, such as Ni, are more contracted making complexes with an oxidation state II much more stable than III or IV.[37] Nickel's decreased flexibility in this regard has deterred its use in C-X bond forming reactions. However, its low cost in comparison to its expensive second- and third-row counterparts, make it an attractive alternative. Recently, the Sanford group reported the first C-X (X=halogen) bond-forming reaction from a $Ni^{II}(Ar)(X)$ complex.[6] Complex **1** was reacted with excess bromine to yield the reductively eliminated carbon-bromide product **10**.

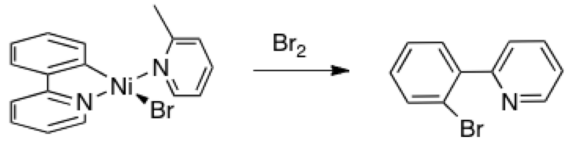

1 **10**

Several possible mechanisms were suggested for the formation of **10**: (1) electrophilic cleavage of the Ni-C bond and C-Br bond formation without a change in the Ni^{II} oxidation state, (2) Br radical attack to form a Ni^{III} 5-coordinate intermediate,

followed by reductive elimination of the product, and (3) oxidative addition of Br_2 onto the Ni^{II} precursor to form Ni^{IV}, followed by the loss of Br^- to form a Ni^{IV} cation intermediate which then reductively eliminates the Ar-Br product (**Scheme 1)**. A definitive mechanism was not established in the study because attempts to isolate a Ni intermediate were unsuccessful. To characterize the Ni byproduct, diphenyphosphinoethane, (dppe), was added to trap the reactive Ni complexes. This addition changed the Ni byproduct from a paramagnetic mixture to the diamagnetic complex, **11**.[6] This observation led the authors to conclude that the reaction proceeded through an intermediate with a high oxidation state for Ni.[38] The present work reports density functional theory (DFT) calculations on the mechanism and energetics of this reaction.

Scheme 1. Proposed pathways[6] for C-Br bond formation from the reaction of **1** with molecular bromine.

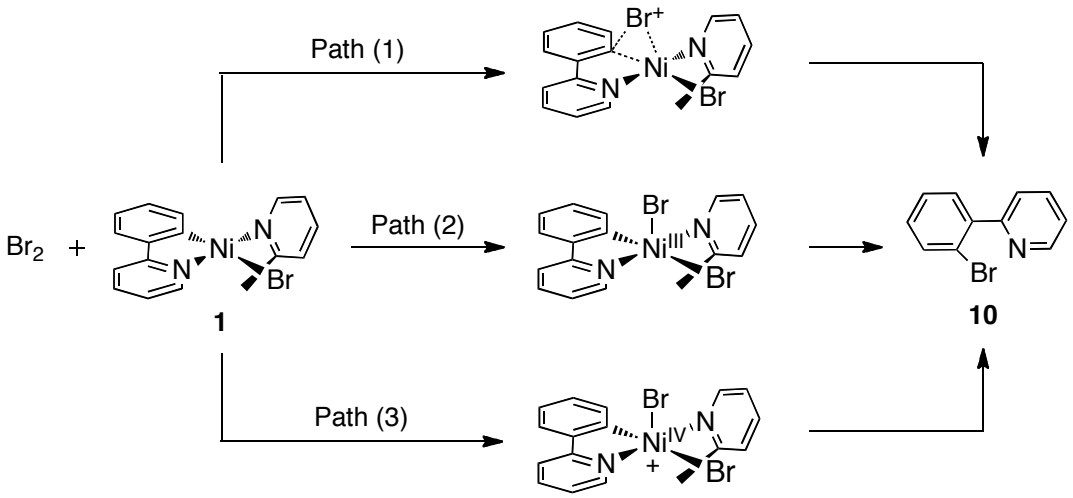

2.2 Computational Details

2.2.1 Functionals and Basis Sets

All theoretical calculations were performed with the Gaussian09 program.[39] Differing functionals were used to examine their accuracy, including BP86,[40] B3LYP,[18,19] BMK,[20] TPSS,[22] and M06.[21] With each functional, two different basis sets were used. Both basis sets used the Pople 6-31G*[41,42] basis set for all carbon, nitrogen, and hydrogen atoms, and the Stuttgart restricted small core 1997 basis set with effective core potential (ECP) for Ni.[43] The two basis sets differed with regards to the Br atoms. The first, smaller basis set used the LANL2DZ ECP and basis set for Br[44], the second, larger basis set used the Stuttgart restricted large core ECP and basis set with an additional d polarization function[45] in the basis set. The BP86 density functional, along with the larger basis set was used for all geometry optimization and frequency calculations herein. The PES of both the triplet and singlet paths are mapped and fully characterized. All structures were fully optimized, and analytical frequency calculations were performed on all structures to ensure that either a minimum or first-order saddle point was achieved. The solvation energies were calculated on the geometries from BP86 gas-phase optimizations via the polarizable continuum model (PCM)[46] with the radii and non-electrostatic terms for Truhlar and coworkers' SMD solvation model[47] with solvation parameters corresponding to benzene. *Ab initio* calculations including MP2, MP3,[48] MP4(SDTQ), CCSD,[49] and CCSD(T)[50] were used to confirm the BP86 results. With the *ab initio* calculations two basis sets were used, the larger basis set with SDD on the Br atoms, and an all-electron 6-311++g(2d,p)[51] Pople basis set on all the

atoms. The 3D molecular structures displayed in this article were drawn by the JIMP2 molecular visualization and manipulation program.[52]

2.2.2 Calibration and Methodology

Initial investigations used the smaller LANL2DZ ECP and basis set for Br to calculate the PES. However, with the realization that the Br_2^- and Ni^{III} interaction on the triplet surface was a important factor in the mechanism, the basis set was expanded for Br to the Stuttgart restricted large core ECP and basis set with an added d function. With the smaller basis set the transition states for the singlet state could only be calculated as unrestricted singlets. While with the larger basis set the restricted, singlet transition states could be calculated. The latter calculations gave a more accurate picture of the singlet and triplet energy differences.

With the multiple crossings of the triplet and singlet surfaces in this mechanism, a density functional had to be chosen that would correctly minimize the multiplits energy. Since the final product, Ni(dppe)Br_2 (**11**), is experimentally known to be a diamagnetic, square planar complex,[53] functionals were tested for accuracy by comparing the energy difference between the triplet and singlet confirmations of **11** (Appendix A). BMK and B3LYP predicted the solvated free energy for the triplet state to be lower than the singlet state by 19.25 and 13.36 kcal/mol, respectively. The percentage of Hartree-Fock (HF) exchange in these two functionals parallels the degree of error in favoring the triplet state. M06 has a smaller percentage of HF exchange when compared with B3LYP and BMK, and its results aligned more with the experimental

results. TPSS and BP86, both pure functionals, predicted the electronic energies and enthalpies of the singlet state to be lower in than the triplet. However, the free energy of the triplet state was lower than the singlet state for TPSS. With BP86 the free energy of the singlet state was still lower than the triplet, so BP86 was chosen as the functional to be reported herein because it provided results that best matched the experiment.

Additional MP2, MP3, MP4(SDTQ), CCSD, and CCSD(T) single-point calculations were done with an abbreviated model of **11** and the geometry from the BP86 optimizations. The abbreviated model had hydrogen atoms in place of the phenyl rings on the dppe ligand. The energy values for these calculations are shown in supplemental information. Since these levels of theory are more sensitive to the basis set, the basis set was expanded to the all-electron 6-311++g(2p,d) Pople basis set. With the larger Pople basis set the single point energies calculated at the CCSD(T) level of theory resembled the experimental results. However, the MP energies were diverging with the increase in perturbation order. This leads us to the conclusion that the CCSD(T) has a sufficiently precise cancellation of errors to yield accurate results with respect to the experimental results. The geometries of the abbreviated **11** model were also optimized at the MP2 level of theory for both the singlet and triplet state. The calculations for the singlet state geometry predicted the bond lengths between the metal and ligands to be too short, while the triplet state geometry dissociated the dppe ligand from the Ni center leaving a $NiBr_2$ and an unbound dppe ligand as the lowest energy (Appendix A).

2.3 Results and Discussion

Of the three originally proposed possible pathways, the Sanford group experimentally disproved pathway (1), **Scheme 1**. This path requires a bromine cation to electrophilically attack and form the Ar-Br bond while simultaneously breaking the Ar-Ni bond. The direct attack of Br^+ was proposed because the Ni oxidation state would be static in this reaction. In this pathway the Br species that forms the Ar-Br bond must come from the oxidant. This pathway was disproved when the Ar-Br product was be isolated when using a chlorine-containing oxidant. They also reported that the cation Ni species in pathway (3) is the least probable because Ni^{IV} is highly unstable. As we will show below pathway (2), which proceeds through a Ni^{III} intermediate, and reductively eliminates Ni-bound ligands to form the Ar-Br product is similar to our predicted mechanism. The complete predicted mechanism involves several intermediates and crossings of singlet and triplet surfaces not obvious from the simple description in **Scheme 1**. Herein, a singlet-state structure will be denoted with an S superscript and a triplet-state structure will be denoted with a T superscript.

Reactant $\mathbf{1}^S$**,** the initial low-energy, closed shell, square planar structure, is shown in **Figure 2.1**. The experimental structure reported by the Sanford group[6] and theoretical geometry of $\mathbf{1}^S$ are compared in **Table 2.1**. The triplet state, complex $\mathbf{1}^T$, takes on a distorted tetrahedral geometry (Appendix A) and has a solvated free energy 18.7 kcal/mol higher in energy than $\mathbf{1}^S$. The energy diagram for the reaction mechanism of complex $\mathbf{1}^S$ plus unreacted molecular bromine[54] as zero relative energy is shown in **Figure 2.2**. The electronic energies, enthalpies, gas-phase free energies, and solvent

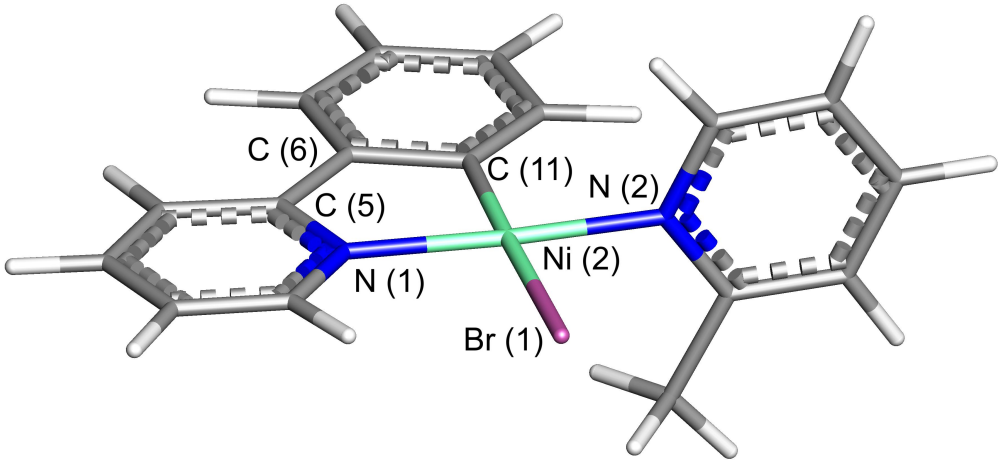

Figure 2.1. The closed shell, square planar BP86 geometry of complex $\mathbf{1}^{S}$. Molecular bromine and $\mathbf{1}^{S}$ are the zero relative energy for the mechanism.

Table 2.1. Experimental values[a] and theoretical values from complex $\mathbf{1}^{S}$. Bond lengths (Å) and angles (°).

Bond Lenths/Angles	Experimental	Theoretical
Br (1) – Ni (2)	2.4035(3)	2.4281
Ni (2) – N (2)	1.8894(13)	1.8891
Ni (2) – C (11)	1.8944(15)	1.9057
Ni (2) – N (1)	1.9168(13)	1.9253
N (2) – Ni (2) – C (11)	91.19(6)	91.9
N (2) – Ni (2) – N (1)	174.66(5)	176.3
C (11) – Ni (2) – N (1)	84.36(6)	84.9
N (2) – Ni (2) – Br (1)	87.54(4)	86.4
C (11) – Ni (2) – Br (1)	172.27(4)	178.2
N (1) – Ni (2) – Br (1)	97.27(4)	97.0

[a] Higgs, Andrew J.; Zinn, Paul J.; Simmons, Sarah J.; Sanford, Melanie S. *Organometallics* **2009**, *28*, 6142.

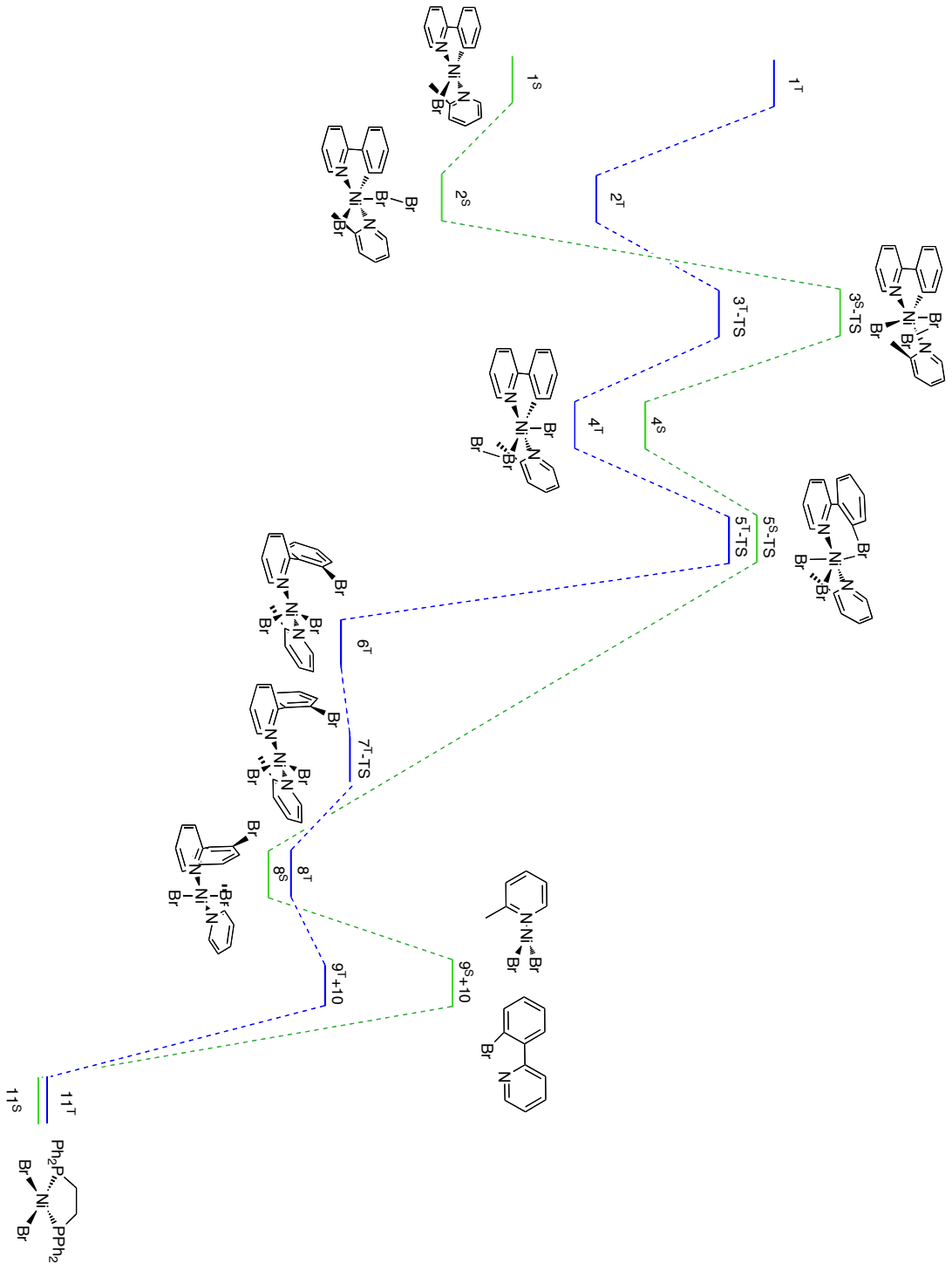

Figure 2.2 Solvated free energy diagram. The lowest energy structures are shown for each intermediate or transition state.

corrected free energies for the singlet and triplet states are shown in **Tables 2.2** and **2.3**, respectively.

The attachment of Br_2 to complex $\mathbf{1}^S$ was calculated for several geometries to determine the lowest energy species. These include η^1 axial addition to the Ni center, η^1 axial addition to the equitorial bromide, and η^2 addition across the Ni-C bond. Each attachment was calculated from both sides of complex $\mathbf{1}^S$, top-side away from the methyl group on the picoline and bottom-side near the methyl group. Attachment of Br_2 to the Ni on the bottom-side of the complex was higher in energy for both the η^1 and η^2 cases because of the steric hinderance associated with the methyl group. Attachment near the equitorial bromide resulted in the formation of $[Br_3^-]$ attached to the Ni by the center Br. Although this species was a stable intermediate, the intermediate was not on the reaction pathway. The lowest energy attachment was the η^1 axial addition to the Ni center on the side without the methyl gorup. This attachment formed complex **2** and stabilized the solvated free energy of complex $\mathbf{1}^S$ by 5.02 kcal/mol. Both singlet and triplet state structures are shown in **Figure 2.3.** In the singlet state Br_2 binds to the Ni by forming a 3-center, 4-electron (3-c, 4-e) bond between the Ni d_z^2 orbital and the two Br p_z orbitals. In other words, the HOMO of $\mathbf{1}^S$ (d_z^2) donates into the LUMO (σ^*) of Br_2 leaving the fully antibonding (between all three atoms Ni-Br-Br) orbital as the LUMO, shown in **Figure 2.4**. This bonding interaction between the Br_2 and the Ni elongates the Br-Br bond distance to 2.54 Å (~halfway between the distance for Br_2 and Br_2^-) and produces a nearly linear Ni-Br-Br angle (164.8°). This closed-shell singlet state is lower in energy than the triplet state. The difference in solvated free energy between the two states is

Table 2.2. Calculated Relative Gas-Phase Electronic Energies, Enthalpies, Free Energies and Solvent Corrected Free Energies (kcal/mol) for Singlet PES

Structure	ΔE	ΔH	ΔG	ΔGsol
1^S	0.00	0.00	0.00	0.00
2^S	-15.40	-14.30	-4.56	-5.02
3^S-TS	10.90	11.20	22.4	23.6
4^S	-4.40	-3.37	8.79	9.49
5^S-TS	4.86	5.01	17.1	17.6
8^S	-28.8	-27.5	-18.2	-17.3
9^S+10	1.86	1.42	-2.57	-4.35
10+11^S+2-picoline	-31.6	-31.9	-33.3	-34.7

Table 2.3. Calculated Relative Gas-Phase Electronic Energies, Enthalpies, Free Energies and Solvent Corrected Free Energies (kcal/mol) for Triplet PES

Structure	ΔE	ΔH	ΔG	ΔGsol
1^T	23.2	22.5	19.7	18.7
2^T	-2.05	-1.11	7.04	6.03
3^T-TS	3.45	3.74	14.2	14.9
4^T	-3.94	-2.98	5.44	4.77
5^T-TS	4.25	4.16	14.3	15.6
6^T	-20.5	-19.5	-12.1	-12.0
7^T-TS	-19.9	-19.5	-11.3	-11.5
8^T	-24.3	-23.3	-15.5	-15.2
9^T+10	-7.06	-8.83	-11.6	-13.3
10+11^T+2-picoline	-27.9	-28.3	-32.4	-33.3

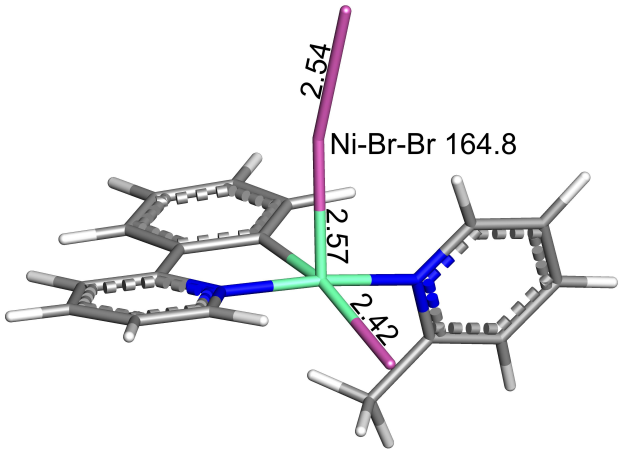

Singlet state $\mathbf{2}^{S}$

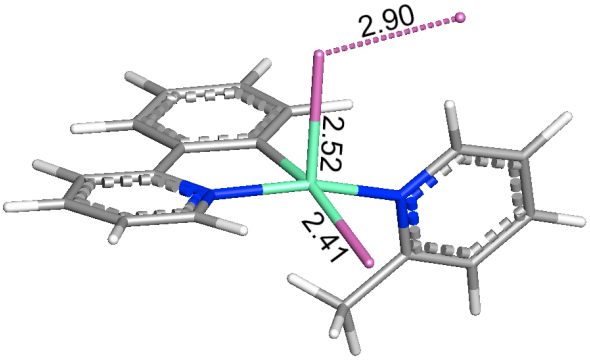

Triplet state $\mathbf{2}^{T}$

Figure 2.3. The singlet and triplet state structures of complex **2**. At this intermediate $\mathbf{2}^{S}$ is forming a 3-center, 4-electron bond and is lower in energy than $\mathbf{2}^{T}$. Bond distances (Å) and angles (deg).

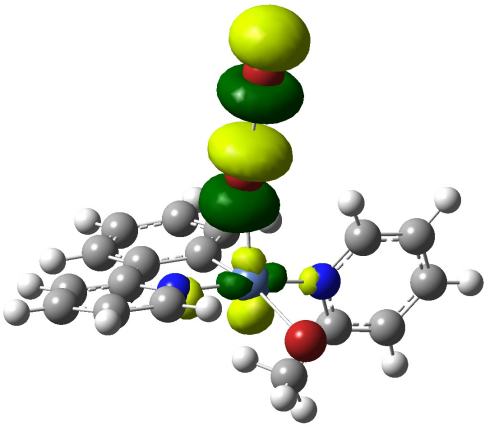

LUMO

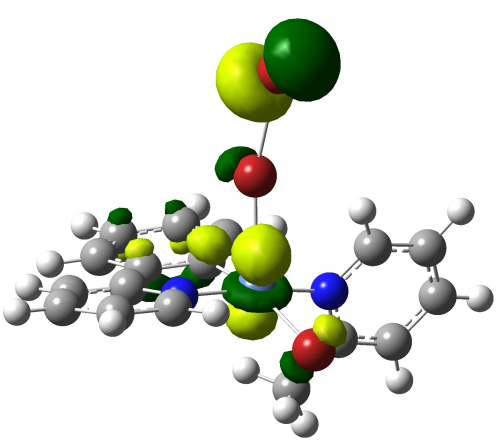

HOMO-4

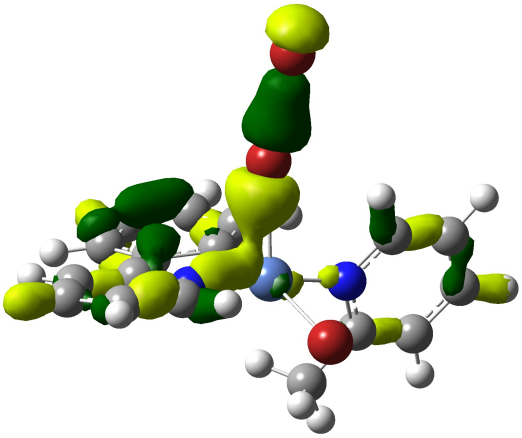

HOMO-21

Figure 2.4. The antibonding (LUMO), non-bonding (HOMO-4), and bonding (HOMO-21) molecular orbitals of the 3-center, 4-electron bond formed in **2**^{S}.

11.05 kcal/mol, a smaller difference than between the singlet and triplet states of **1**. The spin density of $\mathbf{2}^{T}$ shows the unpaired electron density on the Ni and the molecular bromine, **Figure 2.5**. Thus, it would appear that in $\mathbf{2}^{T}$ Br_2 has oxidized the Ni^{II} to Ni^{III}. Consistent with this conclusion, the Br-Br bond distance has increased to 2.90 Å, nearly equal to that calculated for Br_2^-, and the SOMO appears to be the Br_2 σ^*, **Figure 2.5**. The Ni-Br_2 bond now consists of an electron pair in the Br_2 π^* orbital donating to the half-occupied Ni d_z^2 orbital, a 3-center, 3-electron bond with a Ni-Br-Br angle of 114.1°.

In **3-TS** the previously unbound Br in Br_2 begins to migrate towards and interact with the Ni center. This new Ni-Br interaction forms in the equitorial position while the original Ni-Br equitorial bond is pushed into the axial position. In the singlet state the Br_2 bond elongates from 2.54 Å in complex **2** to 2.80 Å in **3-TS**, while in the triplet state the bond decreases slightly from 2.90 Å to 2.88 Å. The reaction coordinate also moves from the singlet PES to the triplet PES here. **Figure 2.6** shows similarities in the geometries of $\mathbf{3}^{S}$**-TS** and $\mathbf{3}^{T}$**-TS**. The 3-c, 4-e bond which stabilized complex $\mathbf{2}^{S}$ is broken because of the Br_2 rearrangement, so the singlet has a large increase in free energy. In comparison, the movement from $\mathbf{2}^{T}$ to $\mathbf{3}^{T}$**-TS** does not perturb the stabilizing properties of the Br_2^- and Ni^{III} interaction of the triplet state as much as the Br-Br bond is still quite close to that for Br_2^-. The singly occupied molecular orbitals (SOMOs) and spin density of $\mathbf{3}^{T}$**-TS**, shown in **Figure 2.7**, also resembles those seen for $\mathbf{2}^{T}$.

Intermediate $\mathbf{4}^{S}$ has a distorted octahederal geometry: the original Br-Br bond is broken, and the new Ni-Br bond is the equitorial position. Thus, the three Br atoms are bound in a meridinal fashion to the octahedrally coordinated Ni in this singlet structure.

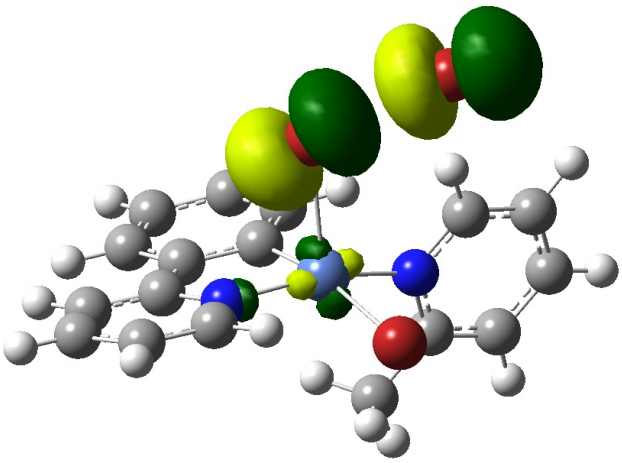

SOMO

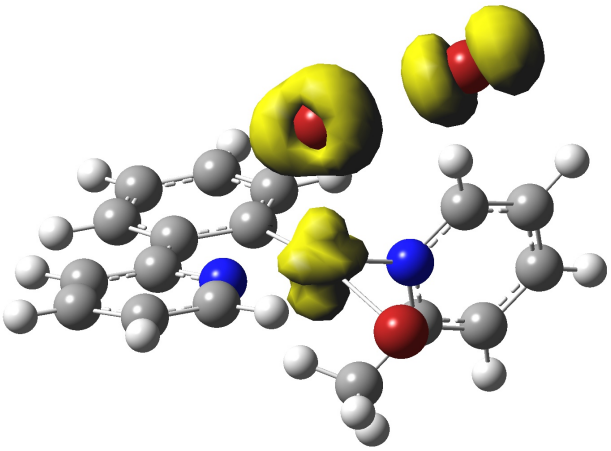

Spin Density

Figure 2.5. Singly occupied molecular orbital (SOMO) and spin density of $\mathbf{2}^{T}$. The SOMO shows the occupied Br_2 σ^* interaction. The unpaired electrons in spin density reside on the Ni center and the axially bound Br_2. Isovalue 0.05.

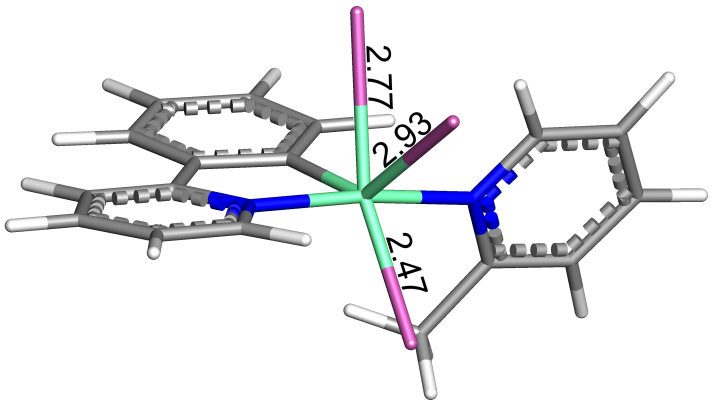

3^{S}-TS

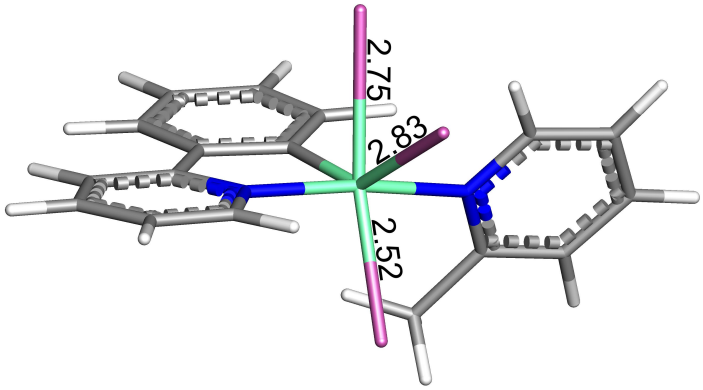

3^{T}-TS

Figure 2.6. The singlet and triplet state geometries for **3-TS**. Both structures assume a distorted octahedral geometry. At this transition state **3^{T}-TS** is lower in energy than **3^{S}-TS**. Bond distances (Å).

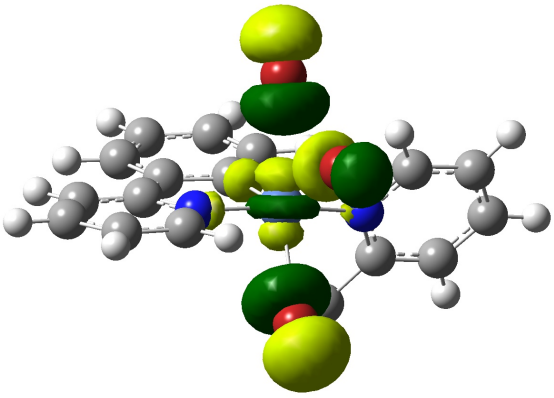

SOMO (1)

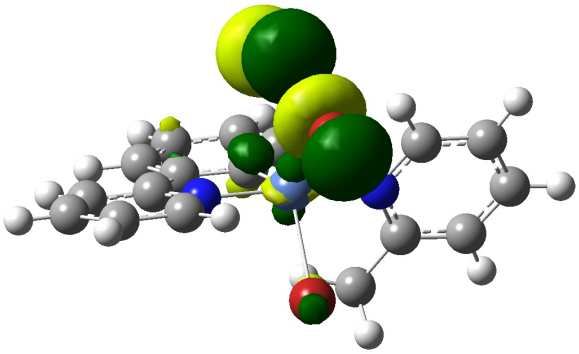

SOMO (2)

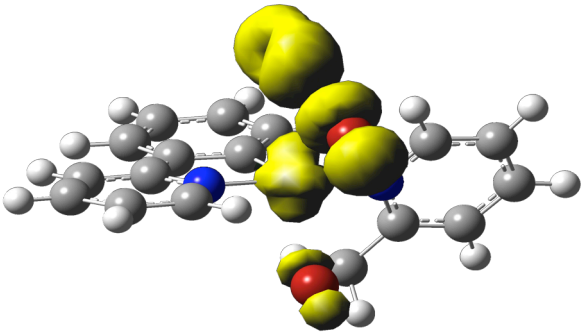

Spin Density

Figure 2.7. SOMOs and spin density of **3^{T}-TS**. The SOMO still has a large amount of Br_2 σ^* character alone with d-orbital character. The spin density shows the unpaired electrons are largely localized on the Ni and Br atoms. Isovalue 0.05

The singlet state solvated free energy drops when forming intermediate $\mathbf{4}^{S}$ because a new 3-c, 4-e bond is established between the Ni and the two axial bromides, **Figure 2.8**. Despite the stability increase on the singlet surface, the reaction remains on the triplet surface as the Br_2^- and Ni^{III} combination is still more stable but has now switched to include the original Br. In intermediate $\mathbf{4}^{T}$ a new Br_2^- interaction is established between the newly bound Br and the original Ni bound Br from complex **1**. This interaction is reflected in the new Br-Br bond distance of 2.95 Å, SOMO(1), and the spin density of $\mathbf{4}^{T}$ shown in **Figure 2.9**. SOMO(1) is the new Br_2 σ^* orbital which was previously on the axially bound Br_2 in complex $\mathbf{2}^{T}$. The spin density also shows unpaired electron density on these two newly interacting bromides, while the other unpaired electron density is localized on the other Br and the Ni center which has a Ni^{III} oxidation state. The positioning of the three bromides in $\mathbf{4}^{T}$ suggests that the original addition of Br_2 could have I equitorially, leading directly to 4^{T} instead of 2^{T}. However, calculations described above suggest that bringing in Br_2 on the bottom-side would be higher in energy. Although less likely, we cannot exclude the formation of 4^{T} by this route. An unrestricted singlet was also calculated for intermediate **4**, but the geometry and energy were only slightly different and less stable than the triplet state. Thus the triplet surface is the most stable at this point in the mechanism.

In **5-TS** the rotation of the bidentate ligand begins so that the axial bromide opposite the methyl group on the 2-picoline group can "reductively eliminate" with the C atom. The formation of an Ar-Br interaction while the Br and C are still bound to the Ni increases the energy to 15.6 kcal/mol on the triplet surface. The strain on the Ni in

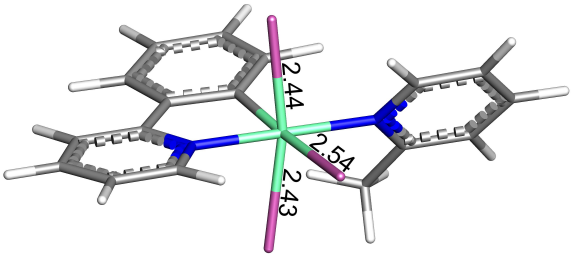

4^{S}

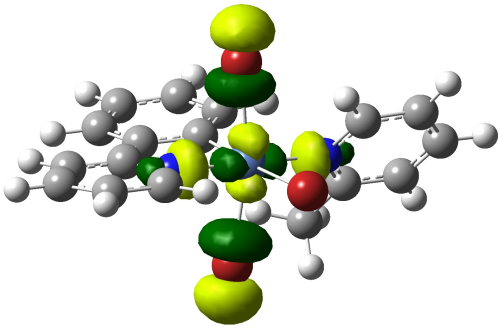

LUMO

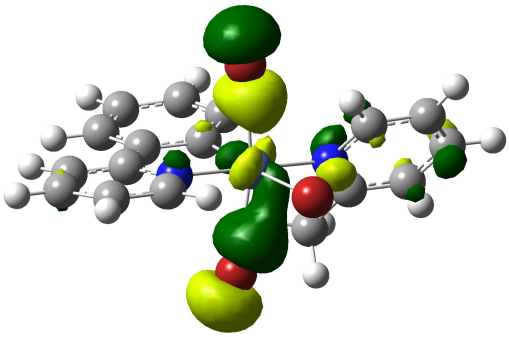

HOMO-10

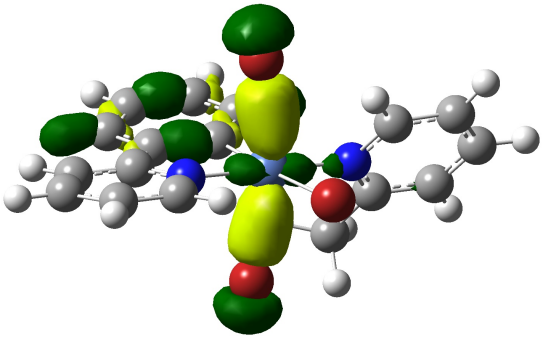

HOMO-19

Figure 2.8. The singlet state geometry of **4**^{S}. The intermediate is in a distorted octahedral geometry forming a 3-center, 4-electron bond interaction with the axial bromides. The LUMO is the 3-center, 4-electron antibonding orbital, HOMO-10 is the non-bonding orbital, and the HOMO-19 is the bonding orbital

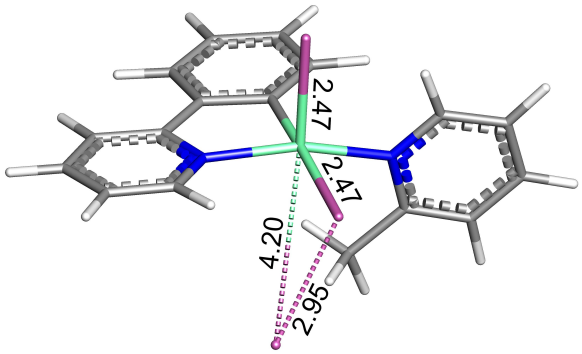

4^{T}

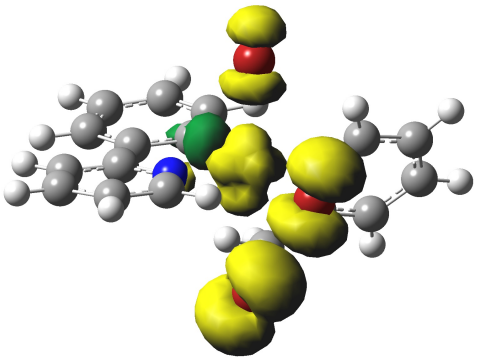

Spin Density

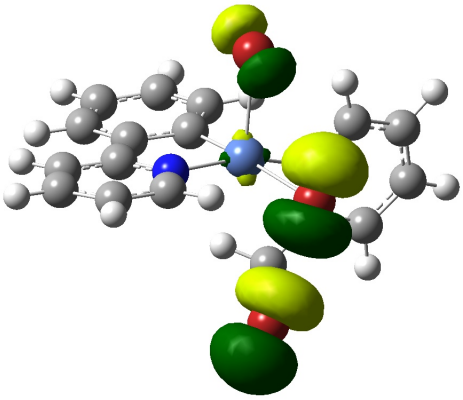

SOMO(1)

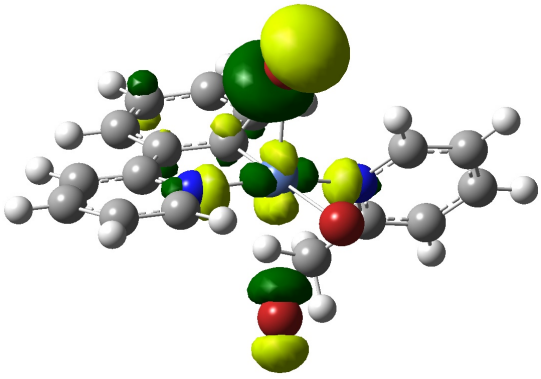

SOMO(2)

Figure 2.9. Geometry of **4**^{T}. Bond distances (Å). SOMOs and spin density of complex **4**^{T}. The highly distorted octahedral geometry allows for the Ni^{III} and Br_2^- interaction. Isovalue 0.05

this geometry is relieved when the bidentate ring system bends out of the plane breaking the Ni-C bond and completing the Ar-Br bond, as shown in intermediate $\mathbf{6}^{T}$ and complex $\mathbf{8}^{S}$.

The singlet surface does not have an intermediate that resembles $\mathbf{6}^{T}$ because **6** has a tetrahedral geometry that would not be stable on the singlet surface.[55] In $\mathbf{7}^{T}$**-TS** the rotation of the 2-picoline ligand completes the breaking of the long-range Br-Ni interaction in $\mathbf{6}^{T}$. $\mathbf{7}^{T}$**-TS** is also only found on the triplet surface since there is no intermediate **6** on the singlet surface. Structures of $\mathbf{6}^{T}$ and $\mathbf{7}^{T}$**-TS** are shown in **Figure 2.10.**

On the triplet surface intermediate $\mathbf{8}^{T}$ decreases in energy by 3.66 kcal/mol from $\mathbf{7}^{T}$**-TS**. The triplet structure remains in a distorted tetrahedral geometry, while the singlet of $\mathbf{8}^{S}$, 2.17 kcal/mol lower in energy, adopts a slightly distorted square planar geometry, **Figure 2.11**. The singlet surface drops lower in energy here because the Ni environment is allowed to return to the Ni^{II} d^{8} environment like that of $\mathbf{1}^{S}$. The triplet is also reminiscent of the distorted tetrahedral geometry of $\mathbf{1}^{T}$, but the change in anionic ligands from the aryl group to the Br stabilizes $\mathbf{8}^{T}$ so that the energy difference between the triplet and singlet states is smaller here. As the carbon ring of the phenylpyridine ligand rotates further away from the Ni center, the N-Ni bond lengthens until the bond is broken. This leaves the trigonal planar Ni product **9** and the Ar-Br product **10**, **Figure 2.12**. The trigonal planar $\mathbf{9}^{T}$ is more stable than $\mathbf{9}^{S}$ by 8.93 kcal/mol.

Sanford's group could not determine the nature of the nickel byproducts because of the paramagnetic characteristics associated products which may reflect the production

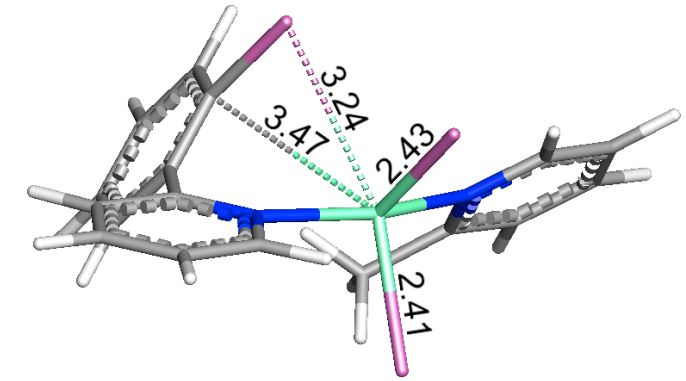

7^{T}-TS

6^{T}

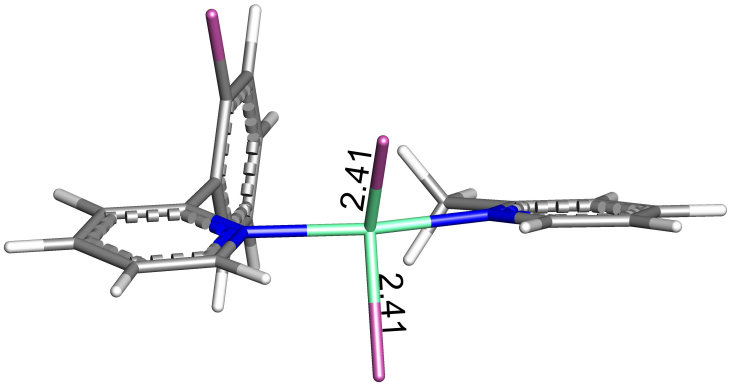

7^{T}-TS

Figure 2.10. Geometries of intermediate **6^{T}** and transition state **7^{T}-TS**. There are no sinlget state structures that correspond to **6^{T}** and **7^{T}-TS**. Bond distances (Å).

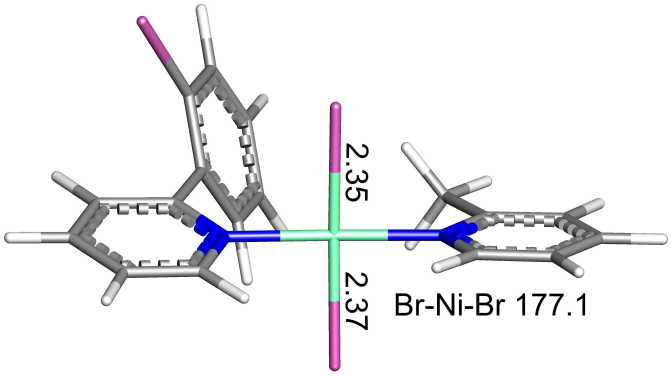

8^{S}

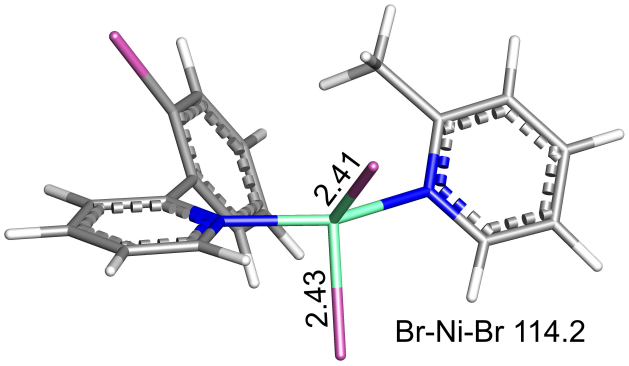

8^{T}

Figure 2.11. Geometries of intermediates **8**^{S} and **8**^{T}. At this intermediate the lower energy state is the singlet because of its square planar geometry, which is more stable than tetrahedral for a Ni^{II} complex. Bond distances (Å).

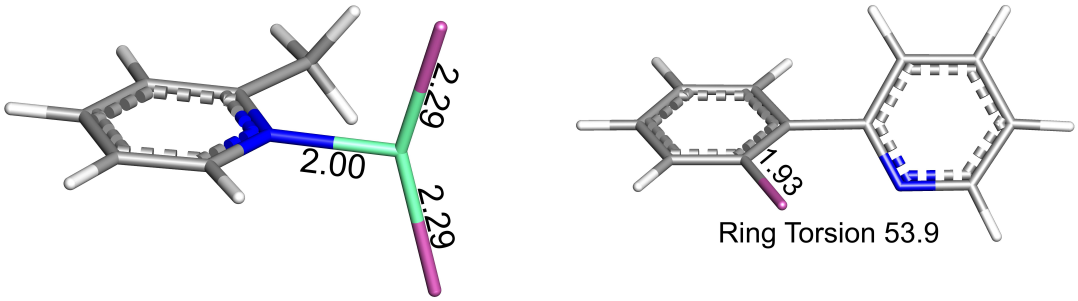

Figure 2.12. Structures $\mathbf{9}^{S/T}$ and **10**. Complex **9** on the singlet and triplet surface are identical, and this geometry is more stable in a triplet state, so the mechanism moves to the triplet surface here. Bond distances (Å).

of $\mathbf{9}^{T}$. When dppe was added to trap the unknown Ni byproduct, complex **11 (Figure 2.13**) was formed. Because dppe is a bidentate ligand, the 2-picoline group was also displaced in the formation of **11**. Here, the reaction moves back onto the singlet PES as $\mathbf{11}^{S}$ adopts a square planar, closed-shell geometry, as shown by the experimental data.

2.4 Conclusion

The mechanistic pathway producing a Ar-Br bond by reductively eliminating complex **10** from the singlet, square planar Ni complex $\mathbf{1}^{S}$ has been fully characterized. The Ni pathway differs from similar Pd and Pt paths because the instability associated with highly oxidized Ni states means that the Ni^{IV} oxidation state is avoided during the reaction by moving onto the triplet PES with a Ni^{III} interacting with Br_2^-. Through the use of the triplet state and 3-c, 4-e bonds, Ni was able to accomplish the bond-forming reaction and avoid the oxidative addition step that seem essential in similar Pd and Pt derivatives. Understanding and exploting this singlet/triplet flexibility should encourage the use of Ni in a wider range of reactions.

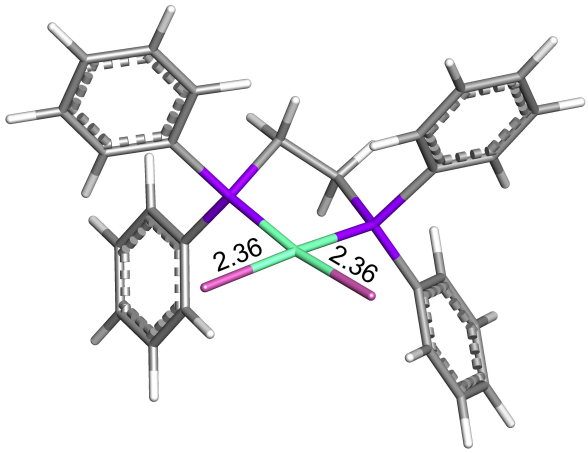

11^{S}

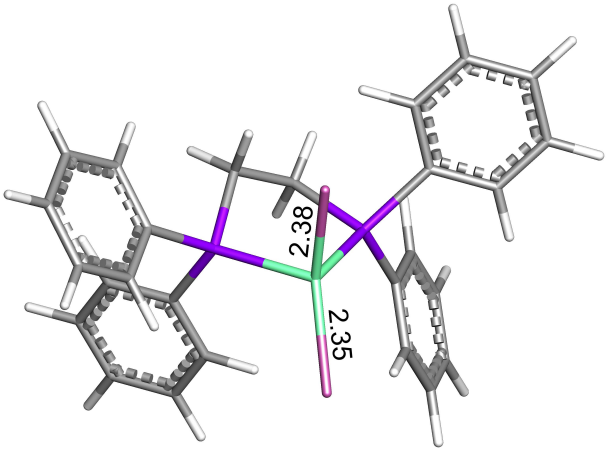

11^{T}

Figure 2.13. Structures of final products **11**^{S} and **11**^{T}. The more stable product is the singlet, square planar complex **11**^{S} which is shown both experimentally and theoretically. Bond distances (Å).

CHAPTER III

CARBON-HYDROGEN ACTIVATION OF CYCLOALKANES WITH CYCLOPENTADIENYLCARBONYLRHDOIUM - A LIFETIME ENIGMA

3.1 Introduction

The C-H bonds in hydrocarbons are all strong, localized bonds. From a molecular orbital perspective there are no low energy, unoccupied or high energy, occupied molecular orbitals that could easily participate in a chemical reaction, and this bonding scheme is what gives alkanes their notorious inertness.[56] Alkanes would be readily used as starting materials in many organic reactions due to their large abundance and cheapness, but the strength of the C-H bonds prevent this from being a reality. Determining a method to utilize alkanes as starting materials has been regarded as one of the "Holy Grails" of C-H activation.[57] Aside from overcoming their inertness, the ability to control the selectivity of activation is also necessary to be able to effectively use them. Improvements on the efficiency of activation and control of selectivity were made with the implementation of transition metal species as homogenous catalysts.[58-60] Starting with Chatt's report of cyclometallation via the activation of napthalene by the zerovalent $Ru(dmpe)_2$ complex in 1965,[61] the use of transition metal species for C-H activation has been widely investigated.[62,63] In the early 1980's the first C-H activation products from methane (the alkane with the strongest C-H bond) were isolated from the coordination with the 16-electron, Cp'ML fragment (Cp' = η^5-C_5H_5 or η^5-C_5Me_5; M = Rh or Ir; L = PMe_3 or CO).[64-67]

Infrared (IR) spectroscopy became an important experimental technique for monitoring C-H activation in species with CO groups because the stretching frequencies are useful for characterizing stable intermediates along the reaction pathway.[68,69] Although monitoring stretching frequencies has given insight into the overall reaction mechanisms, computational methods are needed to resolve the detailed mechanistic picture. Initial calculations explored the electronic structure and bonding in the Cp'ML fragment[70] and comparative strengths of the M-H, M-CH_3, M-L, and M-CO bonds.[71] Density functional theory (DFT)[72] and *ab initio*[73] calculations were then preformed on the full oxidative addition pathway for the activation of methane by the Cp'ML fragment. In addition, computational methods were also been applied to C-H activation of methane with other homogeneous transition metal catalysts.[74-76] As computational power and efficiency increased, the level of theory and the specific alkane being activated also increased from methane to larger hydrocarbons and cycloalkanes.[77,78] Eisenstein and coworkers published free energy values for propane reacting with a TpRh(CNR) fragment in 2007. They reported a lower activation barrier for the terminal C-H bonds than the secondary C-H bonds on propane, which was assumed to be due to larger steric effects associated with the methylene activation. However, a low barrier for the 2,1-migration from the methylene to the methyl group led to the conclusion that the methylene activation would occur less frequently than a migration from the methylene to the methyl group.[79] This migration mechanism was then applied to butane through decane, and similar conclusions were found in regards to the migration mechanism. Until the recent study of George et al.[80] it was assumed that the migration in longer

alkanes proceeded by a series of 1,2-migrations. However, 1,3-migrations were found to have lower energy barriers than 1,2-migrations. Due to the lower barriers, 1,3-migrations were predicted to occur more readily in the C-H activation mechanism than 1,2-migrations for these longer alkanes. Also, for propane and longer alkanes, the methyl group activation barrier's were calculated to be constant, so the lifetime trends were a reflection of the varying migration rates not the C-H activation rates.[80] Since the CH_3 groups on linear alkanes were the dominant group being activated, attention was turned toward cycloalkanes because they do not have any CH_3 groups available for activation. One could naively hypothesize that all cycloalkanes should have the same activation barriers since they are comprised of CH_2 groups only, and that their lifetimes might simply scale linearly with ring size because of sterics. Although these hypotheses would compliment the conclusions found for the linear alkane activations, the lifetime trends determined by fast, time-resolved IR spectroscopic measurements for cyclopentane[81] through cyclooctane did not support such a simple conclusion.

The four cycloalkanes reacting with two Rh fragments (CpRh(CO) and Cp*Rh(CO)) yielded eight reactions to calculate and analyze. The migration mechanism and a second reaction path referred to as the static mechanism, where no migration transfers are included, were calculated for all eight reactions. The calculated lifetimes for both mechanisms were then compared with the experimental lifetimes to determine which mechanism accurately describes the C-H activation of each cycloalkane.

3.2 Computational Details

3.2.1 Methods

All theoretical calculations were performed with the Gaussian 09 suite of programs.[39] A survey of functionals was conducted for the cyclohexane reaction with BMK,[20] B3LYP,[18,19] ωB97XD,[25] TPSS,[22] BP86,[40] PBE,[82] B97D,[23] and M06-L[83] and the 6-311++G**[84-86] basis set for the C, H, and O atoms and the Stuttgart quasi-relativistic basis set and effective core potential for Rh, **Table 3.1**.[87] The cyclohexane reaction was chosen because it was the smallest cycloalkane that had more than one type of σ-complex and activation barrier, axial and equatorial. BP86 and B3LYP calculated the equatorial σ-complex to be more stable than axial, PBE, ωB97XD, B97D, M06-L, and BMK calculated the axial σ-complex to be more stable than equatorial, and TPSS calculated the two σ-complexes to be equal in energy. Since it was unknown which σ-complex was experimentally more stable and the functionals did not consistently calculate the axial/equatorial energy difference, single point CCSD(T)[50] calculations were performed for the cyclohexane reaction with starting geometries from the converged BMK and TPSS geometry optimization calculations. The CCSD(T)//BMK and CCSD(T)//TPSS single point calculations predicted the axial σ-complex to be more stable than the equatorial species, and of the five functionals that predicted this trend, BMK paralleled the relative energy of the CCSD(T) single point calculations the best. The BMK functional was thus chosen to calculate the reaction mechanisms for this work. Although the BMK functional calculated accurate free energy trends, the relative barrier heights were not accurate when compared to the CCSD(T) calculations. The

Table 3.1. DFT calculated free energies for the cyclohexane reaction with CpRh(CO).

	CpRh(CO)-c-hexane					
	σ-complex		Activation Barrier		Product	
	Axial	**Equitorial**	**Axial**	**Equitorial**	**Axial**	**Equitorial**
BP86	-0.24	-0.32	5.12	4.39	-2.44	-4.13
BMK	-0.02	0.37	10.97	9.95	-0.09	-2.79
B3LYP	2.52	2.43	10.73	9.79	3.19	1.22
B97D	-4.44	-3.73	4.97	4.97	-3.92	-5.02
M06-L	-2.73	-2.15	9.64	9.68	1.83	1.14
ωB97XD	-5.15	-4.55	9.29	8.89	2.39	0.81
PBE	-1.82	-1.76	4.78	4.03	-2.70	-4.26
TPSS	-0.38	-0.38	6.10	5.36	-2.78	-4.30
CCSD(T)*	-6.78	-6.34	6.64	6.40	-8.04	-9.46

*Free energies calculated by adding BMK's free energy correction to the CCSD(T) electronic energies.

BMK free energies were therefore scaled with a multaplicative scaling factor from the BMK to CCSD(T)//BMK electronic energy ratio for the respective barrier. The activation barriers were scaled by a factor of 0.68 and the migration barriers by a factor of 1.24. The initial barrier between the separated species and the σ-complex, referred to here as the attachment barrier, was calculated by assuming it is all entropic, which would be expected to be an upper bound in this case. The attachment barrier was reduced by a factor of 0.45 in order to bring the overall simulated lifetimes into the experimental range. All reported values are scaled gas phase free energies, unless otherwise noted, and no corrections for concentration or standard-state units were made. Each species was optimized in the gas phase with tight convergence criteria and on an ultrafine grid as specified in Gaussian 09. Analytical frequency calculations were performed on all optimized structures to ensure that either a minimum or a first-order saddle point was achieved. The 3D molecular structures displayed in this article were drawn with the JIMP2 molecular visualization and manipulation program. [52]

3.2.2 Chemical Kinetics Simulator

The kinetics simulator[88] used a stochastic algorithm to propagate a reaction and produce an output of the reaction species' concentration versus time. The reaction rates were calculated from transition state theory, **Equation 3.1**, and were put into the simulator, then the lifetimes were computed with the proportional relationship between the product's half-life and lifetime**, Equation 3.2**.

$$k = k_b T/h \exp(-\Delta G^{\pm}/RT) \quad (3.1)$$

$$t_{1/2} = \ln(2)\tau \quad (3.2)$$

The separated species were used as the initial reactants with a attachment barrier specific to each reaction, and the reverse, dissociation reaction was not included in the simulation because of arguments presented previously.[81] For each cycloalkane reaction the final products were added together in the simulation, and the half-life was determined by the concentration of the summed final products.

3.3 Results and Discussion

3.3.1 Reaction Scheme

Basically, there are two steps in the C-H activation of cycloalkanes with the Cp'Rh(CO) fragments, **Scheme 3.1**. The first step proceeds over a mostly entropic barrier to form a C-H σ-complex from the separated cycloalkane and Cp'Rh(CO) fragment, and the second step is the oxidative addition which breaks the C-H bond and forms the Rh-C and Rh-H bonds. However, as seen with linear alkane activation, ring migrations can occur between σ-complexes before activation occurs, which transforms this basic two-step mechanism into a multi-step mechanism. For migrations to be energetically important the energy barrier for the migration should be lower than the energy barrier of activation, and for migrations to affect the calculated lifetime there need to be different activation energies for different C-H bonds on the cycloalkanes. The

free energy of the ring migration barriers relative to those for activation and the plausibility of ring migrations altering the lifetime were addressed for all eight reactions.

Scheme 3.1. Two-step C-H Activation of Cycloalkanes with Cp'Rh(CO)

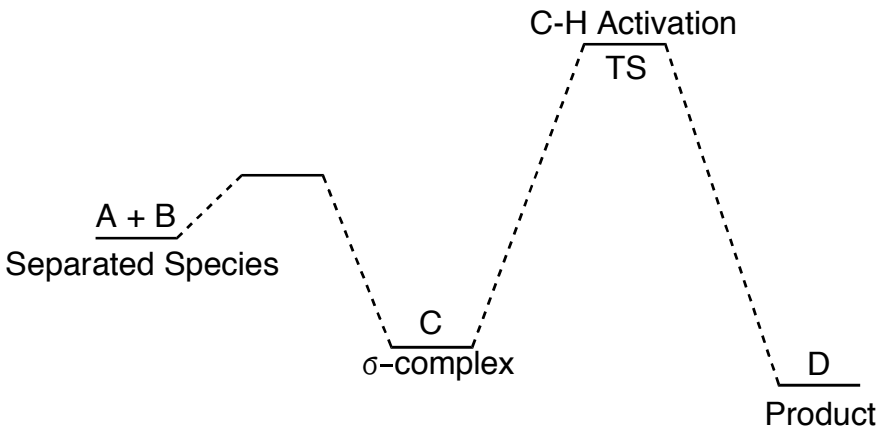

3.3.2 Reactants

All six reactants were optimized individually to determine their lowest energy confirmations and to compare their electronic structures. The two Rh fragments, which only differ by additional methyl groups on the Cp ligand, are shown in **Figure 3.1**. Because of the methyl groups, Cp* is a stronger donor than Cp. This difference is reflected in stronger and shorter Rh-C bonds and by a longer C-O bond in the Cp* fragment, **Table 3.2**. In the reaction, the Cp* fragment could form a more stable σ-complex because the Rh can back-donate more into the C-H σ antibonding orbital, but the Cp* fragment is more sterically crowded which offsets the stabilizing effect. The

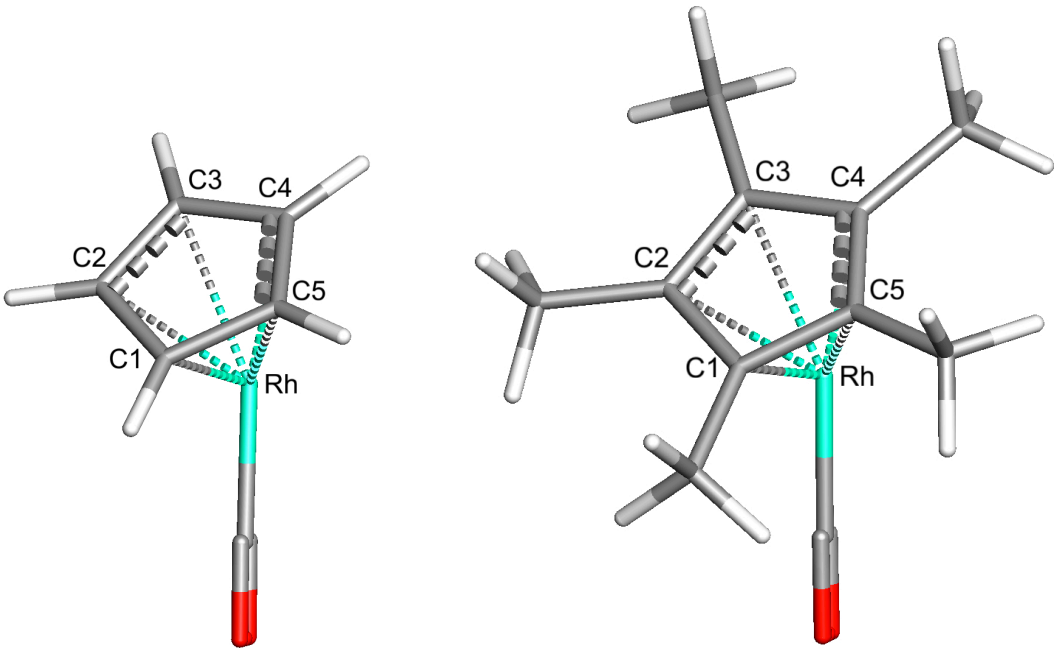

CpRh(CO) Cp*Rh(CO)

Figure 3.1. Optimized geometries for the CpRh(CO) and Cp*Rh(CO) fragments. The C-Rh bond distances on the Cp*Rh(CO) fragment are shorter than the CpRh(CO) species because the methyl groups are electron donating which forms stronger bonds between the Rh and the ligand.

Table 3.2. Bond distances between Rh and ligands on CpRh(CO) and Cp*Rh(CO)

Bond	CpRh(CO)	Cp*Rh(CO)
Rh-C1	2.113	2.099
Rh-C2	2.271	2.274
Rh-C3	2.300	2.291
Rh-C4	2.298	2.292
Rh-C5	2.277	2.274
Average	2.252	2.246
Rh-C	1.866	1.864
C-O	1.144	1.148

four cycloalkanes were individually optimized in their most stable confirmation, **Figure 3.2**. The cyclopentane's lowest energy confirmation is the envelope, which has C_s symmetry and six different C-H bonds. The chair confirmation is the most stable geometry for cyclohexane, which has two different C-H bonds, axial and equatorial. Cycloheptane maintains a C_2 axis in the twisted chair confirmation, which has seven different C-H bonds, and cyclooctane has C_s symmetry in the boat chair geometry which has ten unique C-H bonds. **Table 3.3** lists the various C-H bond lengths for the cycloalkanes; the stability of the complexes is strongly influenced by the C-H bond strength, which parallels the distance.

3.3.3 CpRh(CO) Reactions

A σ-complex structure was calculated for each C-H bond for all four c-alkanes to confirm that the unique C-H bonds form distinct intermediates. For cyclohexane, cycloheptane, and cyclooctane distinct intermediates were formed, but the six different C-H bonds in cyclopentane all converged to the same σ-complex. Cyclopentane's lowest energy confirmation is the envelope, which has four CH_2 groups in the same plane and the fifth group puckered out of the plane. When any C-H bond binds to the Rh, the cyclopentane rearranges by puckering the CH_2 group opposite from the bound C-H bond, **Figure 3.3**. Unlike the rest of the calculated cycloalkanes, the cyclopentane activates one of two electronically unique C-H bonds on the ring, so ring migrations will not affect the lifetime because they are redundant in this reaction. The free energy activation barrier was predicted to be 5.94 kcal/mol, so the activation barrier along with

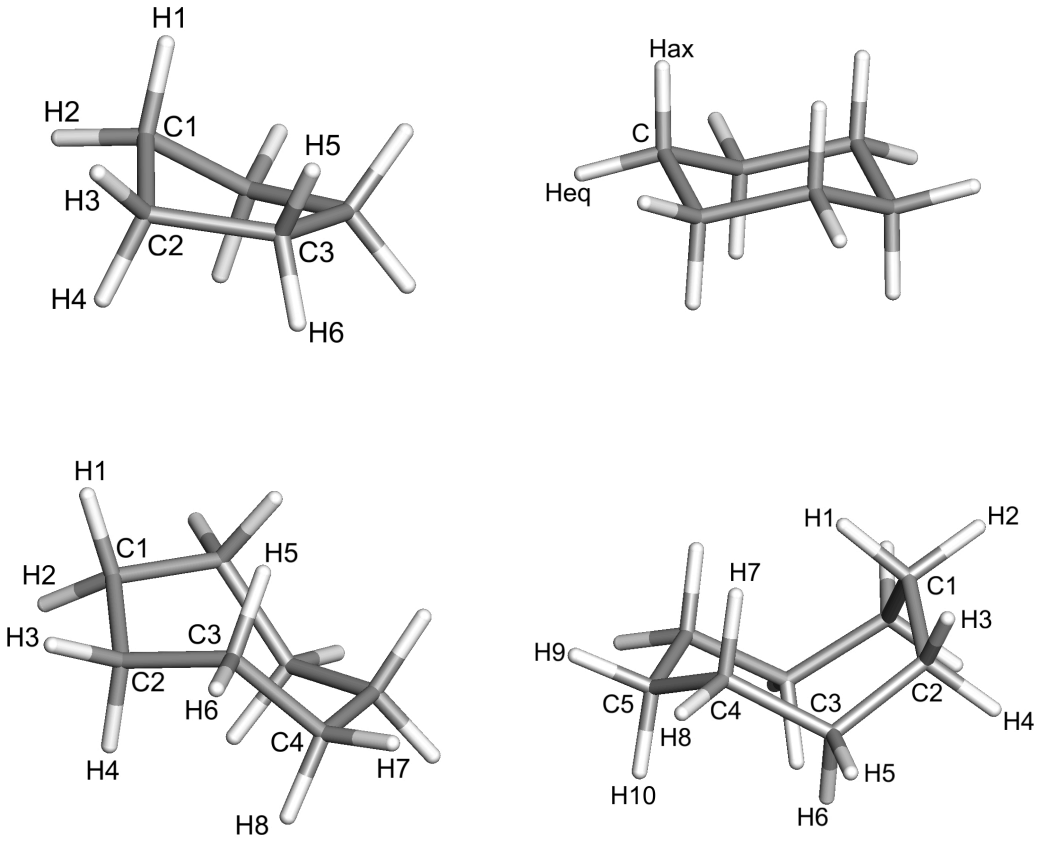

Figure 3.2. The lowest energy confirmations for each cycloalkane. The different C-H groups are denoted.

Table 3.3. Bond distances for the C-H bonds in the separated cycloalkanes

cyclopentane		cyclohexane		cycloheptane		cyclooctane	
C1-H1	1.097	**C-Hax**	1.099	**C1-H1,C1-H2**	1.097	**C1-H1**	1.096
C1-H2	1.094	**C-Heq**	1.096	**C2-H3**	1.096	**C1-H2**	1.097
C2-H3	1.094			**C2-H4**	1.097	**C2-H3**	1.098
C2-H4	1.096			**C3-H5**	1.099	**C2-H4**	1.098
C3-H5	1.094			**C3-H6**	1.096	**C3-H5**	1.096
C3-H6	1.093			**C4-H7**	1.099	**C3-H6**	1.094
				C4-H8	1.097	**C4-H7**	1.097
						C4-H8	1.096
						C5-H9	1.097
						C5-H10	1.099

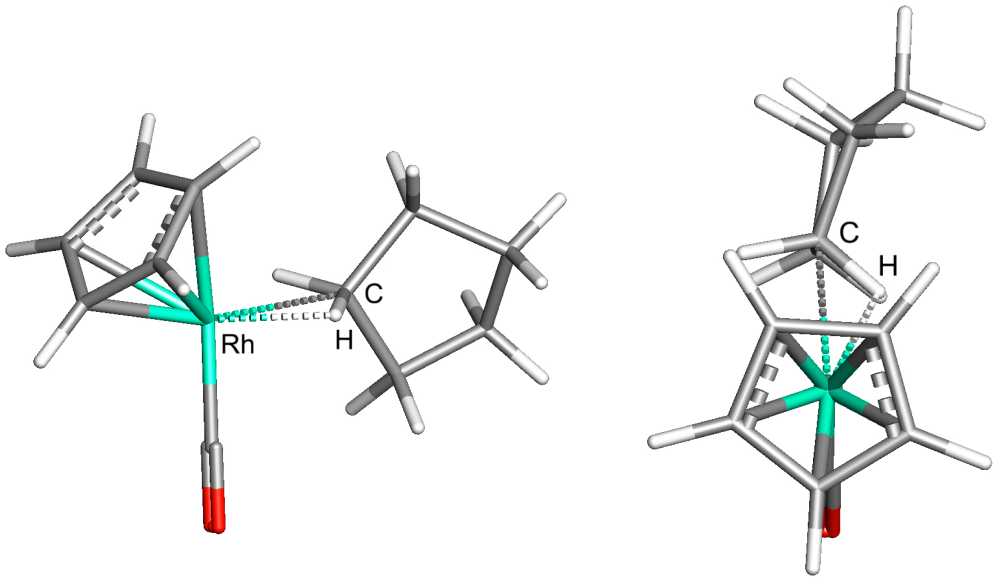

Figure 3.3. Cyclopentane only activates one unique C-H bond. When any C-H bond forms an interaction with the Rh center the cyclopentane relaxes into the same geometry where the CH_2 group opposite the bound C-H is the puckered, out-of-plane carbon. A side view and a top view are shown for the same σ-complex.

the attachment barrier of 5.09 kcal/mol are the main influences on the lifetime of this reaction.

The cyclohexane reaction could proceed through two different C-H bonds, axial and equatorial. The equatorial bond is the stronger C-H bond in cyclohexane with a calculated bond distance of 1.096 Å, while the axial bond is weaker and longer at 1.099 Å. Because of the difference in bond strengths, the σ-complexes that form from these two bonds are not energetically equivalent. The axial species was determined to be 0.07 kcal/mol more stable on the free energy surface than its equatorial counterpart. This energy difference is reflected by the shorter, less activated C-H bond in the equatorial intermediate, **Figure 3.4**. The longer C-H bond in the axial complex relates to more electron density transfer between the two fragments, as the longer C-H bond is effectively a better donor (less stable occupied MO) and better acceptor (more stable unoccupied MO). The transition states that follows the σ-complexes also vary in energy, however, the equatorial transition state is lower in energy than the axial one, 6.52 kcal/mol to 6.97 kcal/mol, respectively. This difference is due to decreased steric repulsion associated with binding to the equatorial position over the axial position. The equatorial path also has an earlier transition state, denoted by the shorter C-H bond distance of 1.528 Å compared to the axial one of 1.561 Å, which is consistent with the lower energy activation barrier. Since the two σ-complexes have different activation barriers this reaction could be influenced by a ring migration. The two types of ring migrations that were calculated in cyclohexane are the 1,1-migration and the 1,2-migration. The first type is the transfer between the two C-H bonds on the same carbon.

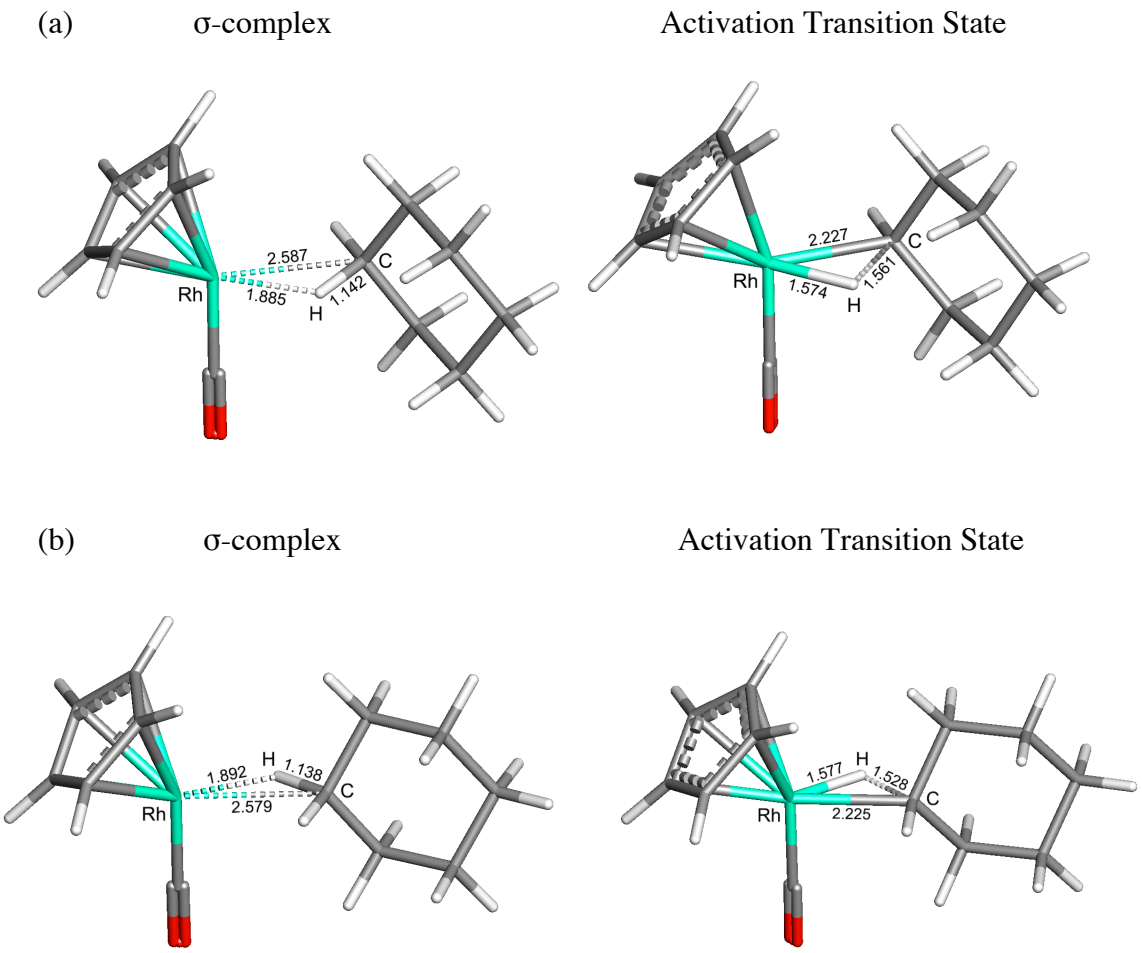

Figure 3.4. The optimized geometries for the cyclohexane reaction with CpRh(CO). (a) The axial reaction forms the more stable σ-complex which is shown by the longer C-H bond and shorter Rh-H bond. (b) The equitorial reaction has a lower energy barrier because it is earlier on the reaction surface and the equatorial position is less sterically hindered, which is shown in the transition state by the shorter C-H and Rh-C bond.

This migration is a conversion between the axial and equatorial σ-complexes and has a barrier of less than 1 kcal/mol in either direction. The second type of migration is a transfer between adjacent CH_2 groups on the ring, which only occurs between equivalent C-H bonds as axial to equatorial (or vice versa) has too much steric repulsion. The barriers for these transfers were calculated to be higher in energy than either of the activation barriers, 7.97 kcal/mol and 12.00 kcal/mol for equatorial and axial 1,2-migrations, respectively. Therefore, the energetics predict that 1,2-migrations will be slow and 1,1-migrations will be rapid in the cyclohexane reaction.

Increasing the cyclohexane ring by one CH_2 group increases the number of possible σ-complexes from two to seven, and, like cyclohexane, the σ-complexes have different stabilities. Although the energies of the cyclohexane σ-complexes can be rationalized by the strengths of the interacting C-H bonds, the cycloheptane σ-complex stabilities are not as straightforward. Two factors determine the stability of each intermediate, the strength of the specific C-H bond and the sterics associated with the Rh fragment binding that C-H bond. Sterics play a larger role in the stability of cycloheptane σ-complexes because the twisted chair confirmation that is maintained in each intermediate causes the ring to have various proximities to the Rh fragment. Intermediates where the ring is turned into the Rh fragment are less stable than those with the ring pointed away, **Figure 3.5**. Coupling sterics with the varying C-H bond strengths creates the range of σ-complex energies shown in **Table 3.4** and the possibility for the cycloheptane lifetime to be altered by the addition of ring migrations. The free energies of activation for the seven σ-complexes average to 7.12 kcal/mol with a range

(a)

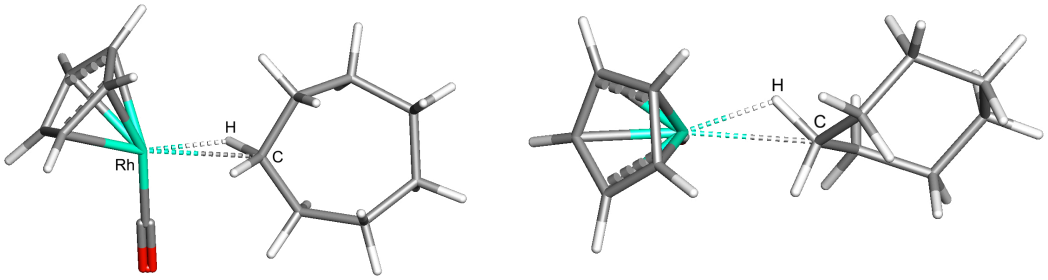

(b)

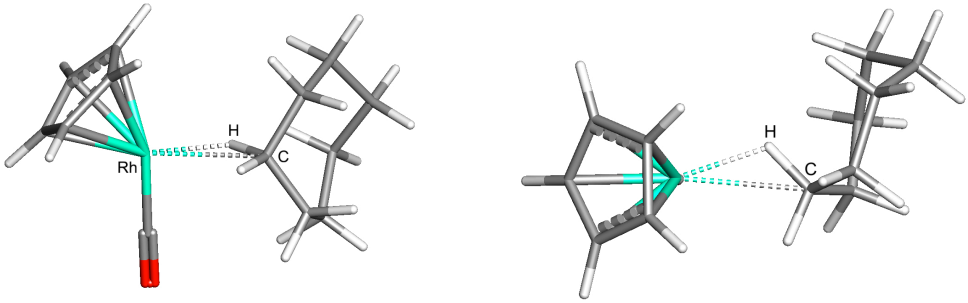

Figure 3.5. The most stable (a) and the least stable (b) cycloheptane σ-complexes. The energy difference between the most stable and the least stable is derived from the sterics incurred when binding to a specific C-H bond on the cycloheptane molecule. The most stable structure does not crowd the Rh fragment while the least stable geometry positions the ring in closer range of the Rh fragment. A top and side view are shown of the two σ-complexes

Table 3.4. Relative free energies (kcal/mol) for the seven σ-complexes in the cycloheptane reaction[a]

Activated C-H Bond	CpRh(CO)	Cp*Rh(CO)
C1-H1, C1-H2	0.00	0.00
C2-H3	0.14	0.87
C2-H4	0.20	0.86
C3-H5	0.43	1.47
C3-H6	0.35	0.79
C4-H7	0.31	0.72
C4-H8	0.24	1.39

[a]The zero relative energy is the most stable species, and the numbering scheme is shown in **Figure 3.1**.

from 6.88 to 7.46 kcal/mol. Ring migrations could decrease the lifetime of the overall reaction by populating the σ-complex with the 6.88 kcal/mol activation barrier and depopulating the intermediates with higher energy activation barriers. There are four different types of migrations that can occur for in the cycloheptane reaction, 1,1-migrations, 1,2-migrations, 1,3-migrations, and 1,4-migrations. The 1,1-migrations, transitions between the two C-H bonds on the same CH_2 group, again have low energy barriers of ~1 kcal/mol, and the two intermediates connected by a 1,1-migration are assumed to be in near equilibrium. Unlike cyclohexane, there are two types of 1,2-migrations in the cycloheptane mechanism and they depend on the orientation of the adjacent CH_2 units, **Figure 3.6**. If the H-C-C-H dihedral angle formed by the two C-H bonds involved in the migration is less than 60°, an inside 1,2-transition occurs, but if the angle is larger than 60° an outside 1,2-migration occurs. The inside 1,2-migrations barriers have a range from 7.54 to 7.72 kcal/mol, while the outside 1,2-migrations barriers range from 4.52 to 10.19 kcal/mol. The larger range for the outside 1,2-migrations is due to the lower stability of the outside σ-complexes, which are ~3-4 kcal/mol less stable than the inside σ-complexes. Migrating to an outside σ-complex has an energy range from 8.06 to 10.19 kcal/mol, while migrating from an outside σ-complex has a energy range from 4.52 to 7.34 kcal/mol. The 1,3-migrations and 1,4-migrations are similar in appearance because they require the Rh fragment to transfer across the face of the ring, and their energy barriers range between 7.06 and 7.93 kcal/mol. Overall the average migration free energy for cycloheptane is 7.26 kcal/mol which is higher than the average activation barrier of 7.12 kcal/mol. Because this

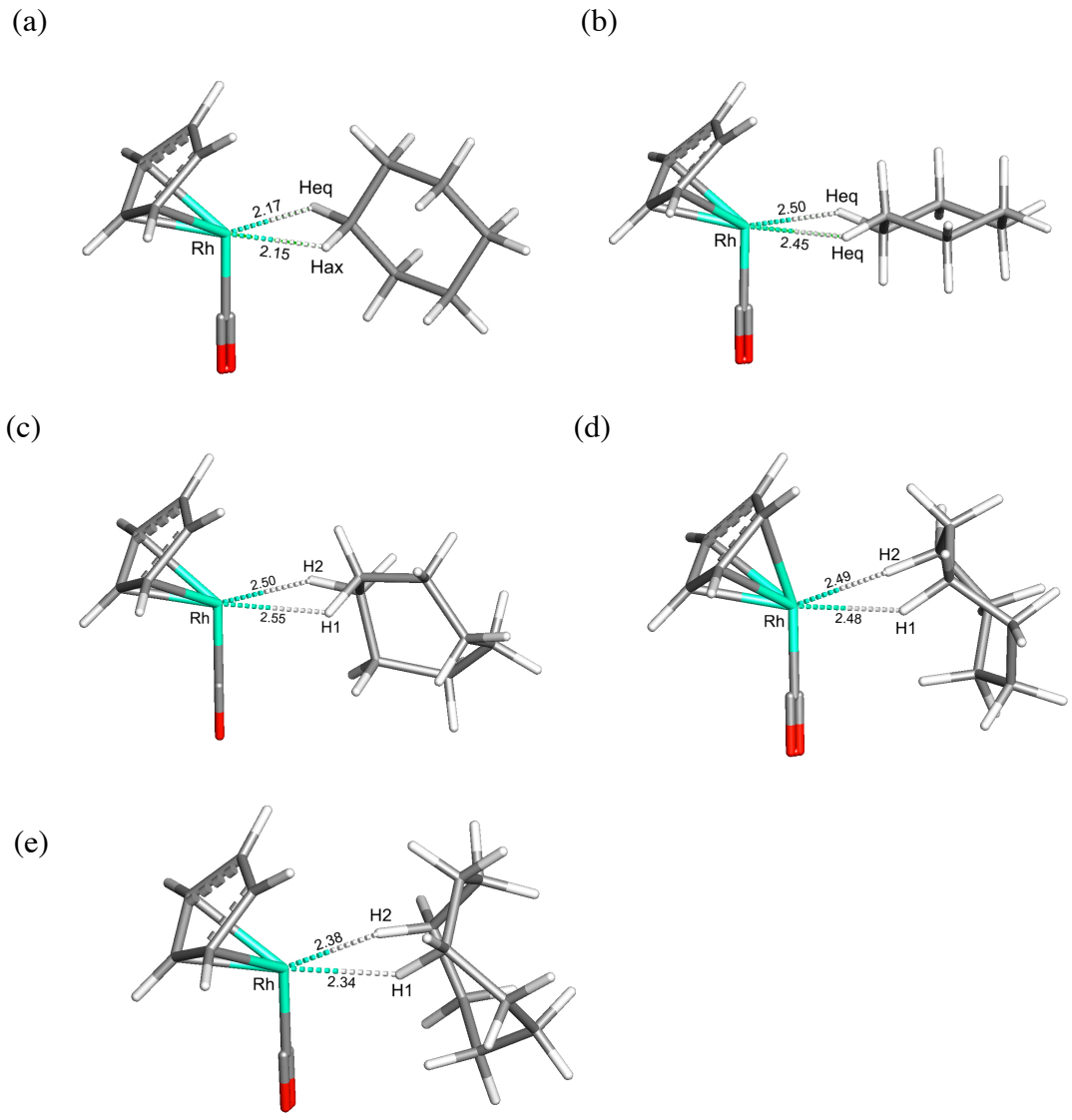

Figure 3.6. (a) The 1,1-migration, a transfer between the two hydrogen atoms on one carbon. (b) The inside 1,2-migration a transfer between two adjacent C-H bonds with a H-C-C-H dihedral angle less than 60°. (c) The outside 1,2-migration, a transfer between two adjacent C-H bonds with a H-C-C-H dihedral angle larger than 60°. (d) The 1,3-migration and (e) 1,4-migration is a transfer across the face of the cycloalkane.

difference is smaller here than in the cyclohexanes reaction these two rates will compete in the overall rate.

Moving from cycloheptane to cyclooctane increases the number of stable σ-complexes from seven to ten. Again, all ten σ-complexes have stabilities derived from sterics and the strengths of C-H bonds, and again there are the same four types of possible migrations 1,1-, 1,2-, 1,3-, and 1,4-migrations. The stabilities of these ten σ-complexes vary more than those of the previous cycloalkanes. For example the relative energy range from most stable to least stable σ-complex for cycloheptane was 0.29 kcal/mol while this range for cyclooctane was 0.90 kcal/mol. This difference is believed to be due to increased steric repulsion caused by the rigidity of the unbound portion of the cyclooctane ring, as shown in **Figure 3.7**. This larger variation in σ-complex stabilities could lead to an even more important effect because the migrations can depopulate the higher energy intermediates and populate the more stable intermediates depopulated by product formation. The migration barriers are similar in energy to the reported energies for the cycloheptane species, and have an average free energy of 7.18 kcal/mol. The 1,1-migrations have barriers ranging from 0.02 to 1.89 kcal/mol, so the two σ-complexes connected by a 1,1-migration are again assumed to be in equilibrium. Only outside 1,2-migrations could be determined with cyclooctane because of the H-C-C-H dihedral angles that are present in the boat-chair confirmation. The outside σ-complexes are again ~3-4 kcal/mol less stable than the inside complexes, and the free energy range for these migrations are from 4.30 to 6.10 kcal/mol from an outside σ-complex and from 7.81 to 10.32 kcal/mol to an outside σ-complex. The 1,3- and 1,4-

(a)

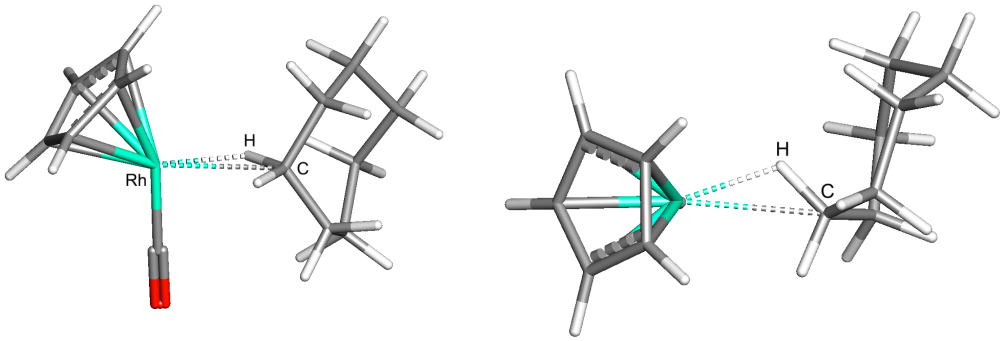

(b)

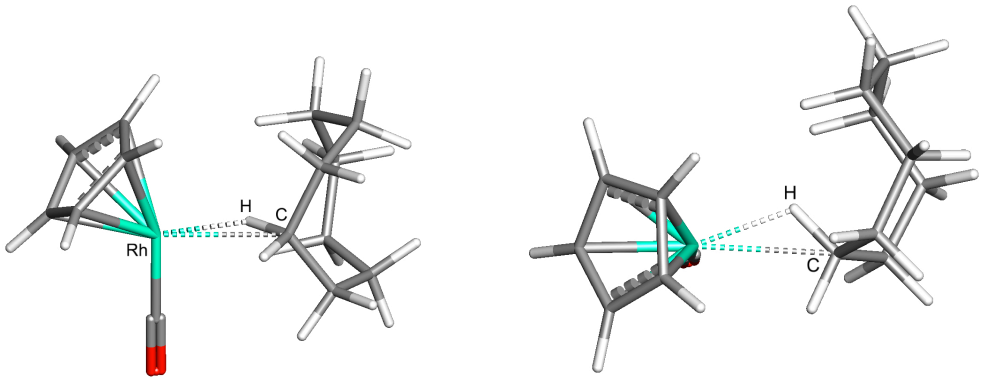

Figure 3.7. A side and top view of the highest energy cycloheptane (a) and cyclooctane (b) σ-complexes are shown to compare the steric crowding between the cycloalkane and the Rh fragment. As the cycloalkane rings get larger their ability to crowd the Rh fragment increases which causes a larger energy range of σ-complexes to form.

migrations have an energy range from 7.18 to 8.64 kcal/mol. The averaged activation barrier energy is 7.65 kcal/mol, with a range from 6.58 to 9.96 kcal/mol. This average barrier is the highest for the four cycloalkanes, but the range of activation energies is also the largest. This higher energy average is due to the steric repulsion increase associated with this reaction, but the larger range suggests that the difference between the static mechanism and the migration mechanism could be larger here.

*3.3.4 Cp*Rh(CO) Reactions*

The differences between the Cp*Rh(CO) and CpRh(CO) reactions lie in a competition between the Cp* fragment's higher electron density and the increased steric repulsion associated with the Cp* ligand, and these differences are reflected in the transition state barriers and the stability of the σ-complexes. The free energy loss upon formation of the σ-complex from the separated species is greater for the Cp*Rh(CO) reactions than the CpRh(CO) reactions, which causes the attachment barriers to be higher in energy for the Cp*Rh(CO) reactions. The cyclopentane attachment barrier is 5.58 kcal/mol which is a 0.49 kcal/mol increase from the CpRh(CO) reaction, and the other three cycloalkanes have an increase of 0.34 kcal/mol from their CpRh(CO) counterparts, which yields attachment barriers of 5.34, 5.38 and 5.70 for cyclohexane, cycloheptane, and cyclooctane, respectively. The σ-complexes for all four cycloalkanes have shorter C-H bonds and longer Rh-C and Rh-H distances with Cp*Rh(CO), **Figure 3.8**, which reflects a destabilized intermediate due to a decreased interaction between the C-H bond and the Rh. Since the σ-complexes are weaker, the energy required for ring

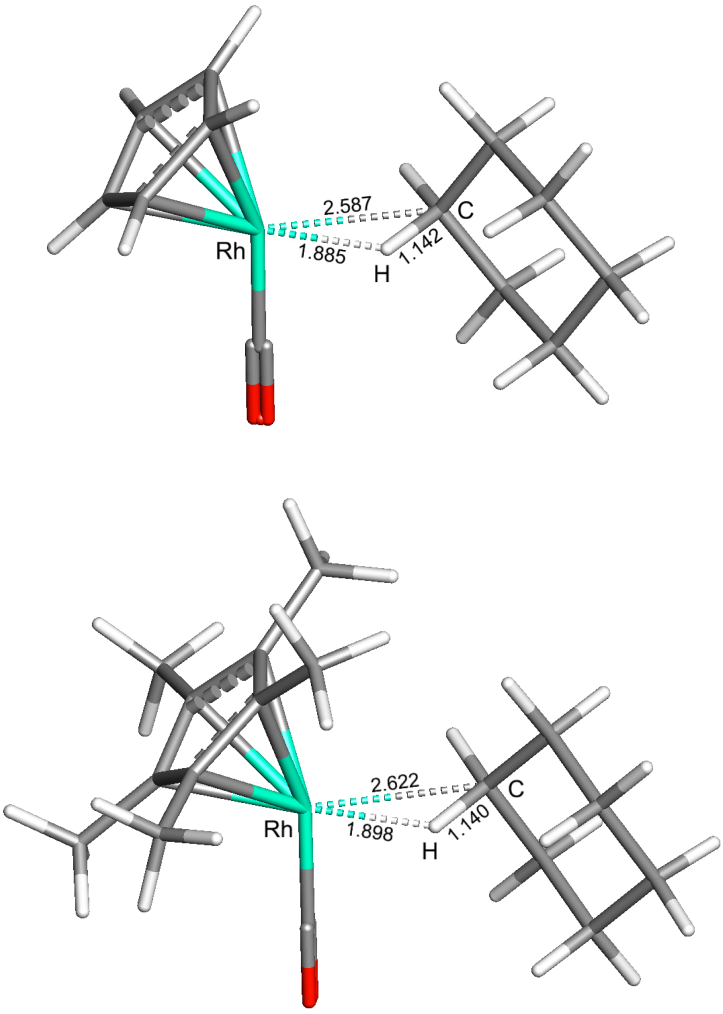

Figure 3.8. Comparison of the cyclohexane reaction with CpRh(CO) and Cp*Rh(CO). The Cp*Rh(CO) σ-complex is less stable than the CpRh(CO) counterpart because the methyl groups add steric crowding and the σ-bond interaction is less stable. This is denoted by the elongated Rh-C and Rh-H bond distances.

migrations between σ-complexes is decreased. The four types of ring migrations were calculated for the three rigid cycloalkanes, and their average free energies were 7.07, 7.24, and 6.53 kcal/mol for cyclohexane, cycloheptane, and cyclooctane, respectively. The migration barrier for cyclohexane is lower than the cycloheptane because only the lower energy equatorial 1,2-migration could be converged. The average activation barriers were calculated to be 5.74, 6.78, 7.47, and 7.90 kcal/mol for cyclopentane through cyclooctane. The activation barriers for the cycloalkanes are affected by the increase in sterics associated with Cp* and their activation barriers all show an increases from the CpRh(CO) barriers. Overall it appears as if the Cp*Rh(CO) reactions could be influenced more by ring migrations than the CpRh(CO) reactions because the σ-complexes are destabilized which causes the migration barriers to decrease in energy and the activation barriers to increase in energy.

3.4 Mechanisms

3.4.1 Static Mechanism

Initially the σ-complexes were assumed to be statistically populated by all proceeding over the same attachment barrier calculated for each cycloalkane. The static mechanism assumes that no ring migrations occur between σ-complexes, and each σ-complex proceeds over its own transition state, i.e. activations are much faster than migrations such that the latter can be neglected. The activation barriers for each pathway were calculated for individual σ-complex/transition state pairs where each σ-complex is its own zero relative energy. The calculated lifetimes for the static mechanism for all

four cycloalkanes and both Rh fragments are compared with the experimental lifetimes in **Table 3.5.**

For cyclopentane there is only one C-H bond to activate and therefore only one reaction mechanism can occur. The calculated lifetimes for the activation of cyclopentane with CpRh(CO) and the Cp*Rh(CO) are 6.6 and 7.4 ns, respectively, which are similar to the experimental lifetimes of 5.9 and 10.2 ns. Although the activation barrier from the σ-complex for the Cp*Rh(CO) reaction is lower than that for the CpRh(CO) reaction, the greater attachment barrier with Cp*Rh(CO) reproduces the experimental observations. The cyclohexane reaction with CpRh(CO) has two pathways, axial and equatorial, which have an activation energy difference of 0.45 kcal/mol. Although this energy difference is small, the calculated lifetime for the axial pathway alone was 25.0 ns, while the lower energy, equatorial pathway predicted a lifetime of 13.3 ns. Including both pathways in the simulation and assuming the static mechanism, the calculated lifetime is 16.2 ns. This shows that the majority of the product is initially formed by the equatorial species with a small contribution from the axial reaction late in the reaction. The 16.2 ns lifetime for the CpRh(CO) reaction is slower than the experimental lifetime of 8.6 ns, and the slope in **Figure 3.9** between the cyclopentane and cyclohexane lifetimes is therefore overestimated. The axial/equatorial free energy difference for the Cp*Rh(CO) reaction is 0.65 kcal/mol, so the small contribution from the axial pathway late in the reaction has a larger affect on the lifetime which was calculated to be 18.3 ns. The cycloheptane simulations calculated lifetimes of 28.4 and 50.9 ns for the CpRh(CO) and Cp*Rh(CO) reactions, and both are in good agreement

Table 3.5. Experimental and calulated lifetimes (ns) for migration and static mechanisms

	CpRh(CO)			Cp*Rh(CO)		
	Static	**Migration**	**Exp**	**Static**	**Migration**	**Exp**
cyclopentane	6.6	6.6	5.9	7.4	7.4	10.2
cyclohexane	16.2	16.0	8.6	18.3	17.2	25.8
cycloheptane	28.4	26.8	22.7	50.9	49.2	60.7
cyclooctane	47.0	40.9	31.7	69.7	56.4	74.3

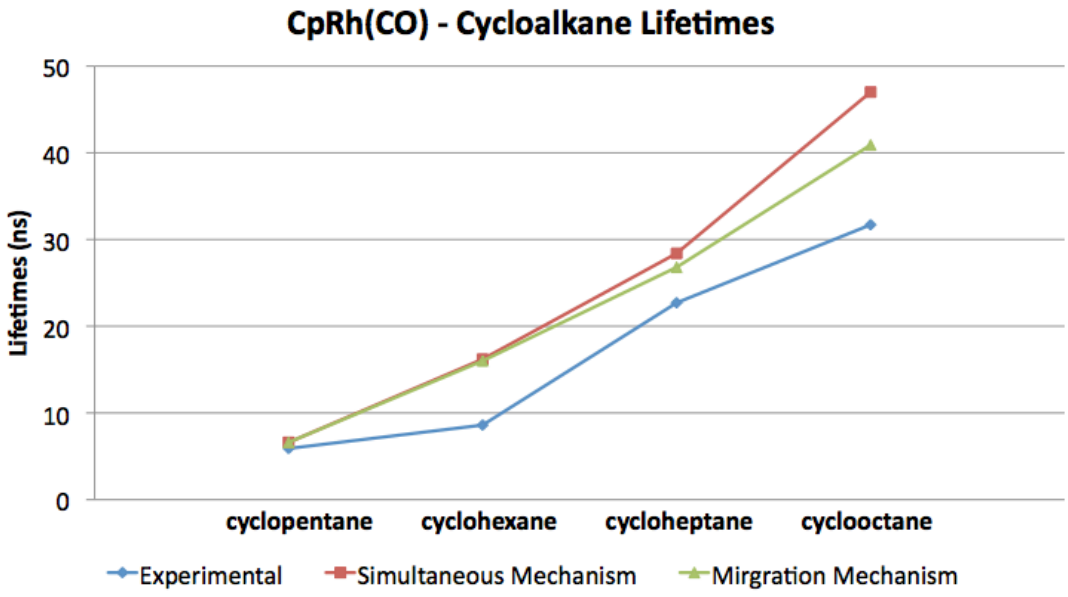

Figure 3.9. Calculated lifetimes for the four cycloalkane reactions with CpRh(CO). Cyclopentane undergoes one mechanism because ring migrations are redundant for this cycloalkane. The cyclohexane and cycloheptane reactions varying only slightly between the two reaction mechanisms. The lifetime for the cyclooctane reactions are more accurately predicted with the migration mechanism and are overestimated with the static mechanism.

with their respective experimental trends. Since the activation barriers and migration barriers are similar in energy for the two cycloheptane reactions the migration mechanism should lower the lifetimes of these reactions by depopulating the higher energy pathways. The lifetime slope between cycloheptane and cyclooctane is too large for both CpRh(CO) and Cp*Rh(CO) reactions because the cyclooctane lifetimes are overestimated. The calculated values of 47.0 and 69.7 ns predict the reactions to proceed too slowly with the static mechanism, however, because the average migration barrier is lower in energy than the average activation barrier for cyclooctane the migration mechanism will correct the lifetime overestimation.

3.4.2 Migration Mechanism

The migration mechanism incorporates the calculated ring-migrations between σ-complexes for each reaction into the overall activation mechanism. The attachment barriers and activation barriers used here were the same barriers calculated for the static mechanism. The migration barrier heights were calculated by the difference between the transition state energy and the σ-complex energy for each case. The calculated lifetimes for the migration mechanism for the eight reactions are compared to the experimental lifetimes in **Table 3.5**.

Cyclopentane was not recalculated with this mechanism because ring migrations are truly redundant (lead to the activation of an equivalent C-H bond). The calculated lifetimes for the cyclohexane and cycloheptane reactions show small decreases in the calculated lifetimes from the static mechanism, **Figure 3.10**. The decrease in the

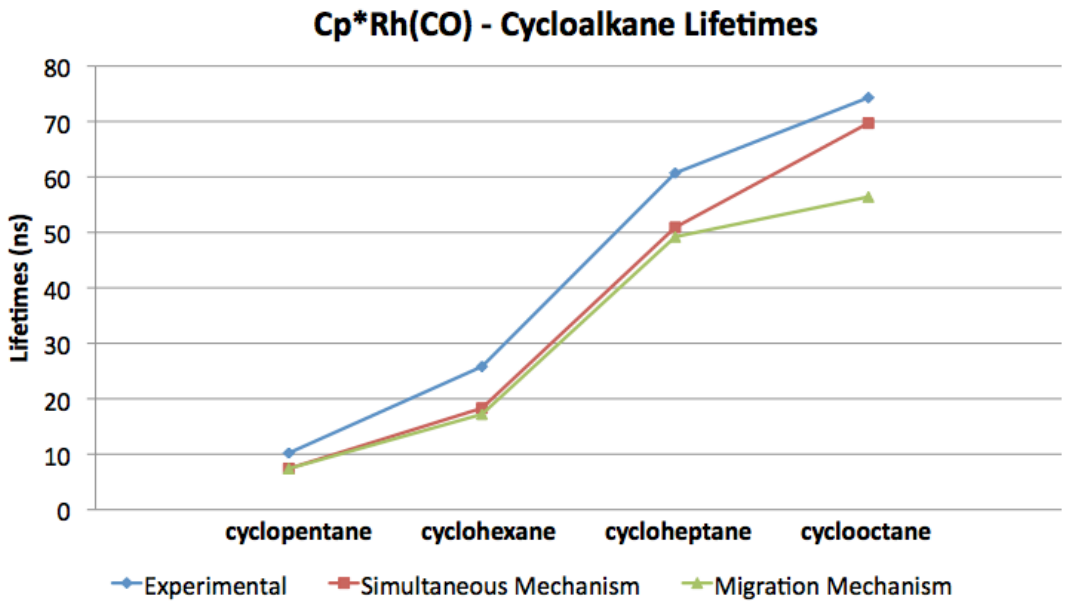

Figure 3.10. Calculated lifetimes for the four cycloalkane reactions with Cp*Rh(CO). Cyclopentane undergoes one mechanism because ring migrations are redundant for this cycloalkane. The cyclohexane and cycloheptane reactions varying only slightly between the two reaction mechanisms. The lifetime for the cyclooctane reactions are more accurately predicted with the migration mechanism and are overestimated with the simultaneous mechanism.

calculated lifetimes is dominated by the addition of the 1,1-migrations because they are the only migrations that are consistently lower in energy than the activation barriers. The lifetime decrease for the cycloheptane reactions could have a larger contribution from other types of migrations, but the difference is not significant enough to conclude the migration importance in these reactions. However, the migration mechanism correctly decreases the calculated static mechanism's lifetimes by 5.9 and 13.3 ns for the cyclooctane reaction with CpRh(CO) and Cp*Rh(CO). The larger lifetime correction, which brings the calculated lifetime into alignment with the measured ones, supports the conclusion that ring-migrations must be included in the overall activation mechanism for cyclooctane. The steric crowding destabilizes the σ-complexes in the cyclooctane reactions which results in lower energy migration barriers and the higher energy activation barriers, which allow the ring migrations to speed up the reaction.

3.5 Conclusion

Since cycloalkanes are only comprised of CH_2 groups, the assumption could be made that the activation energies of various-sized cycloalkanes should remain constant, and the reaction lifetimes should scale linearly with ring-size when sterics are neglected. The experimental lifetimes suggest that this is true only to a degree as the slope is not linear. Here calculations show that with an increase in cycloalkane ring size there is an increase in the number of unique C-H bonds that can be activated. The different C-H bonds form a range of σ-complex stabilities and activation barriers, a range which also increases with ring size. As the energy range increases the ring-migrations become more

important as a way to reach the lower energy pathway. Each of the cycloalkanes has a number of electronically unique C-H bonds that can form σ-complexes and then be activated. Populating the σ-complexes with the lowest energy activation barrier reduces the overall lifetime, but for this to be thermodynamically feasible the migration barriers must be lower in energy than the activation barriers. For cyclopentane, cyclohexane, and cycloheptane there is little to no decrease in lifetime with the inclusion of ring-migrations in the reaction mechanism because the energy of migrating around the ring is higher in comparison to the activation energies. Although the lifetimes for the smaller rings are not largely affected by the incorporation of ring-migrations in the mechanism, the cyclooctane reactions require the addition of ring-migrations to accurately predict reaction lifetimes. This difference with cyclooctane is a result of an increase in sterics, which leads to less stable σ-complexes and, therefore, higher energy activation barriers and lower energy migration barriers. The energy changes for these two types of barriers are large enough to allow the ring to migrate more rapidly between σ-complexes before activation in the cyclooctane reaction. Because the need to include ring-migrations to describe the overall mechanism appears to be related to the size of the cycloalkane, we propose that rings larger than cyclooctane would also proceed through a migration mechanism.

CHAPTER IV

INTRAMOLECULAR CARBON-HYDROGEN BOND ACTIVATION OF *BIS*(2,6-DIMETHYLBENZENETHIOLATO)TRIS(TRIMETHYLPHOSPHINE) RUTHENIUM(II)

4.1 Introduction

Developing systems to activate strong bonds, such as C-H or C-C bonds, has been an important topic of research for over half a century.[89,90] The potential use of hydrocarbons as a cheap resource for synthetic precursors has led to this interest, but the electronic structure of hydrocarbons prevents their bonds from being easily activated because there are neither low-lying unoccupied nor high-lying occupied orbitals with which to initiate a chemical reaction.[91] Transition-metals have proven to be successful at cleaving strong C-H bonds, and many studies have reviewed the catalytic prowess of such transition metal systems.[92] The two most familiar mechanisms for C-H bond activation are oxidative addition[93] and the σ-bond metathesis.[94] Oxidative addition is a bond activation mechanisms common for late transition metals that have electron-rich metal centers with stable higher oxidation states. The mechanism begins with coordination of the C-H bond to an open site on the metal center, and ends with the cleavage of the C-H bond and the formation of a M-H and M-C bond and a metal in a formally higher oxidation state by +2. For early transition metals that are high-valent or d^0 the oxidative addition mechanism is not a viable path, so these species generally undergo σ-bond metathesis, which involves the concerted formation of M-C and L-H

bonds and the breaking of M-L and C-H bonds without a change in the metal oxidation state. Several related reaction mechanisms that vary mainly in the activation transition state have been reported recently: metal-assisted σ-bond metathesis (MAσBM),[95] oxidative hydrogen migration (OHM),[96] σ-complex assisted metathesis (σ-CAM),[97] and oxidatively added transition state (OATS).[98] The interactions between the metal center and the C-H moiety during the activation defines these individual mechanisms.[99] However, prior to activation, all of these mechanisms require a vacant site on the metal center and close proximity of the C-H bond being activated to the metal center. Generally, the C-H bond to be activated will be bound to the metal center as a σ-complex,[100] which then undergoes an intramolecular C-H bond activation. The proximal advantage that intramolecular C-H bond activation has over intermolecular activation has led to its widespread occurrence and to its contribution to controlling the C-H bond to be activated.[101] Palladium complexes have been heavily investigated for intramolecular C-H activation due to their efficient ability to functionalize such bonds;[102] however, interest in intramolecular activation with ruthenium systems has increased over the last ten years because of the photophysical and electrochemical properties of cycloruthenated species.[103]

The first reports of cycloruthenation reactions via C-H bond activation were from Levison and Robinson[104] and Parshall, Knoth, and Schunn.[105] Both of the publications reported on the intramolecular activation of a phosphine ligand on the $(Ph_3P)_3Ru(H)(Cl)$ species, and the latter authors emphasized the reversibility of the cycloruthenation. This work was elaborated by Lewis[106] and James and coworkers[107] who expanded the number

of phosphine-containing hydridoruthenium complexes that could undergo intramolecular C-H activation. Recently, the mechanisms with which these ruthenacyclyes are produced have been under scrutiny in hopes of further exploiting the ruthenium chemistry. Isolation of a C-H-Ru agostic species was reported by Sabo-Etienne et al. for the cycloruthenation reaction of $RuH(H_2)L(P^iPr_3)_2$ [L = 2-phenylpyridine or benzoquinoline].[108] This ortho-metalation was also found to be reversible upon the exposure of the cycloruthenium species to acid and H_2.

Scheme 4.1. The five-coordinate, trigonal bipyramidal complex **1** reacts in benzene to produce the C-H activated product **10b**. In methanol C-H activation does not occur, and the final product is the six-coordinate, octahedral species **10m**.

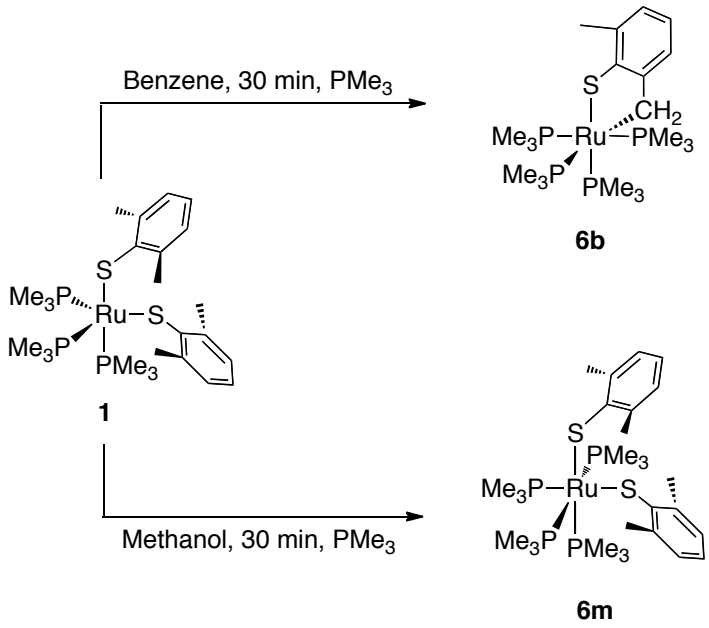

Komiya and coworkers also recently published an investigation of reversible ortho-metalation where an ortho-methyl C-H bond on a five-coordinate bis(2,6-dimethylbenzenethiolato)ruthenium(II) species is activated.[109] The activation occurred at room temperature and pressure in ~30 minutes in benzene and yielded the cyclometallated product *cis*-Ru[SC_6H_3-(2-CH_2)(6-Me)-κ^2S_2C](PMe_3)$_4$. However, a change in solvent from benzene to methanol prevented the activation of the ortho-methyl group and instead produced an unactivated six-coordinate Ru($SC_6H_3Me_2$-2,6-κ^1S)$_2$(PMe_3)$_4$ complex, **Scheme 4.1**. Plausible mechanisms for the intramolecular activation of this reaction were proposed, but a conclusion as to why the activation is hindered by methanol was not made.

Among the early computational studies of intramolecular C-H activation was the work by Jimeñez-Catano and Hall.[110] Their work compared the thermodynamics of the intramolecular activation versus the intermolecular activation of the CpML (M, L = Zr, Cl; Rh, PH_3; and Ir, PH_3) species in methane. The intermolecular activation of methane was predicted to be the most exothermic which was followed by the intramolecular activation of the phosphine and the Cp ligand, respectively. Following this work was a similar study on the inter- and intramolecular activation of CpIr(PMe_3)(CH_3)$^+$ by Niu and Hall.[111] Again, they found that intermolecular activation was a lower-energy process than the intramolecular counterpart. Overall, it was found that the competition between these two routes involves the balance between the entropic changes, which generally favor the intramolecular path, and the strain, which generally favors the intermolecular path. Presented here are the computational details of the density functional theory

investigation of the intramolecular C-H activation of the five-coordinate species $Ru(SC_6H_3Me_2\text{-}2,6\text{-}\kappa^1S)_2(PMe_3)_3$. The reaction's mechanistic details and the product's dependence on the reaction medium were computationally explored along with the electronic structure of the inactivated and activated octahedral products.

4.2 Computational Details

All theoretical calculations were performed with the Gaussian 09 suite of programs.[39] The long-range, dispersion corrected GGA functional, B97D,[23] was used to calculate critical points along the reaction pathways. This type of functional was used because the proximity of the large ligands is best described by a dispersion-corrected functional. Electronic energy calculations were also performed at the B97D optimized geometries with the long-range corrected hybrid functional with dispersion corrections, ωB97XD. Single points were only performed with this functional because of geometry convergence issues that occurred during optimizations. The ωB97XD functional uses the ωB97X functional when calculating the Kohn-Sham-DFT energy, which incorporates Hartree-Fock exchange and a long-range correction, which are not included in the B97D functional. ωB97XD also uses a different damping function than B97D when calculating the dispersion correction. The relative energies calculated by both functionals were very similar, so only the B97D energies are reported in the text (see Appendix C for ωB97XD energies). The Pople-style 6-311G*[112] basis set was used for all sulfur and phosphorous atoms, the 6-31++G**[84] basis set was used for four atoms on the ortho methyl group on the thiolate ligand being activated, the 6-31G*[41,42] basis set was used for the carbon and

hydrogen atoms in the rest of the system, and the Stuttgart, fully relativistic, triple-ζ basis set and effective core potential were used for Ru.[113] Initially, the two mechanisms were calculated in the gas phase. Two methods, explicit and implicit, were used to determine how methanol was influencing the overall reaction. The explicit method optimized the complex **1** in the gas phase with one explicit methanol molecule. The implicit method optimized the critical points with PCM, the radii and non-electrostatic terms for Truhlar and coworkers' SMD solvation model, and the solvation parameters for methanol. Analytical frequency calculations were performed on all optimized structures to ensure that either a minimum or a first-order saddle point was achieved. The energy values reported for the mechanisms are free energies, unless otherwise stated. The 3D molecular structures displayed in this article were drawn with the JIMP2 molecular visualization and manipulation program.[52]

4.3 Results and Discussion

4.3.1 $Ru^{II}(SC_6H_3Me_2$-2,6-$\kappa^1S)_2(PMe_3)_3$

Complex **1** was optimized in the gas phase and converged to a distorted trigonal bipyramidal (TBP) geometry as shown in **Figure 4.1**; a comparison of the experimental and calculated geometric parameters are given in **Table 4.1**. The TBP distortion is shown by the small P(1)-Ru-P(2) angle and large P(1)-Ru-S(2) and P(2)-Ru-S(2) angles. This type of TBP distortion is common in five-coordinate, d^6 transition-metal complexes with strong π-donor ligands in the equatorial plane. As shown in **Scheme 4.2**, having a strong π-donor in the equatorial plane causes the distortion of the TBP geometry from

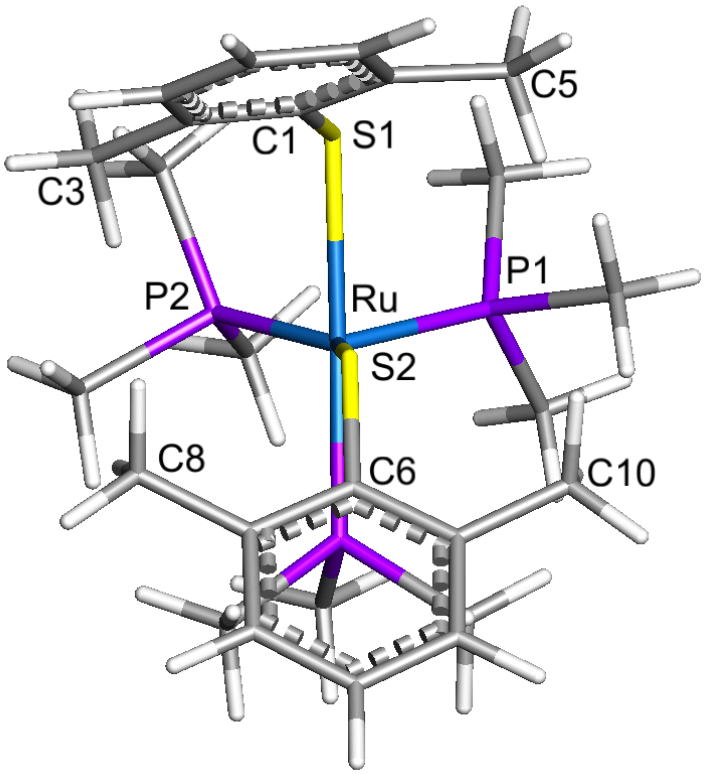

Figure 4.1. The calculated gas phase structure for complex **1** which optimized to a distorted trigonal bipyramidal geometry. The numbering scheme shown here will be used throughout the manuscript.

Table 4.1. The Bond Distances (Å) and Angles (°) of the Crystal Structure and Calculated Geometry of Complex **1**

	Crystal Structure	Calculated Geometry
Ru-S(1)	2.432	2.541
Ru-S(2)	2.341	2.354
Ru-P(1)	2.232	2.234
Ru-P(2)	2.248	2.280
P(1)-Ru-S(2)	127.9	121.6
P(2)-Ru-S(2)	137.1	142.9
P(1)-Ru-P(2)	92.4	93.4
C(6)-S(2)-S(1)-C(1)	157.1	135.1

the normal ~120° equatorial angles because the lone pair on the L ligand π-donates and the X ligands σ-donate into the empty $4d_{xy}$ orbital while the occupied Ru $4d_{x^2-y^2}$ orbital back-donates into the L π* orbital.

Scheme 4.2. Geometries of Five-coordinate, d^6 Ruthenium Complexes[114]

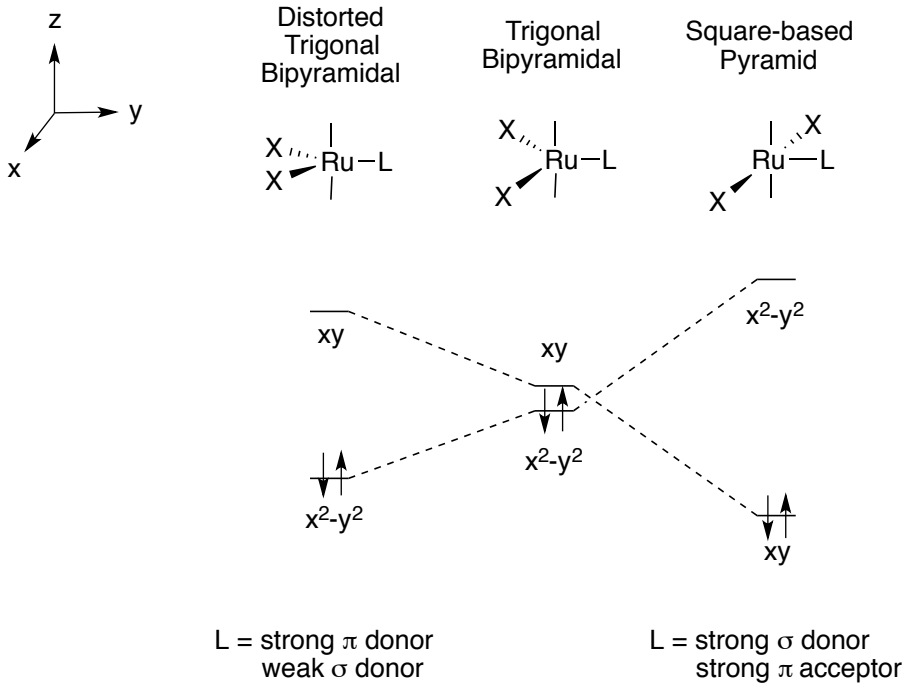

If complex **1** had only strong σ-donors in the equatorial plane the system would be expected to adopt a more square-based pyramidal geometry where the Ru $4d_{xy}$ orbital is occupied and the unoccupied $4d_{x^2-y^2}$ orbital accepts electron density from the three σ-donor ligands. The Ru-S(1) bond distance is longer than the Ru-S(2) bond distance in both the crystal structure and the calculated geometry. This difference is result of the

S(2) lone pair interacting with the unoccupied Ru $4d_{xy}$ orbital and the S(1) lone pair interacting with an occupied Ru $4d_{x^2-y^2}$ orbital. In the S(1) case the π-bonding and π-antibonding molecular orbitals are filled, which results in no net π-bonding in the Ru-S(1) bond. In the S(2) scenario only the π-bonding molecular orbital is filled, so the Ru-S(2) bond has π-bonding character along with the expected σ-bond, which results in a shorter bond for Ru-S(2).

The mirror image of complex **1**, **1'** has, of course, the same energy, and the two minima are connected through two transition states with a low free-energy barrier of 1.59 kcal/mol. Because the motion from **1** to **1'** involves both the PMe_3 methyl rotations and the thiolate movements, one might expect to find a symmetric transition state; however, there appear to also be two transition states, $\mathbf{1}^{TS}$ and $\mathbf{1}^{TS'}$ which are mirror images of each other and indicate that the thiolate move first on the way up to the TS then the PMe_3 groups relax on the way down to the mirror complex, **Figure 4.2**. The symmetric geometry is proposed to be a second order saddle point that connects **1**, **1'**, $\mathbf{1}_{TS}$, and $\mathbf{1'}_{TS}$. The mechanistic details and electronic structure of the two reaction paths are described below while the free energy reaction surfaces are shown in **Figure 4.3**, and the calculated energies are given in **Table 4.2**.

4.3.2 Reaction Mechanisms

In complex **1** there are four ortho methyl groups that could be activated to form the C-H activated product **10b**. The two that are in the closest proximity to the Ru center are the C(8) and C(3) methyl groups, but, unexpectedly, these methyl groups do not

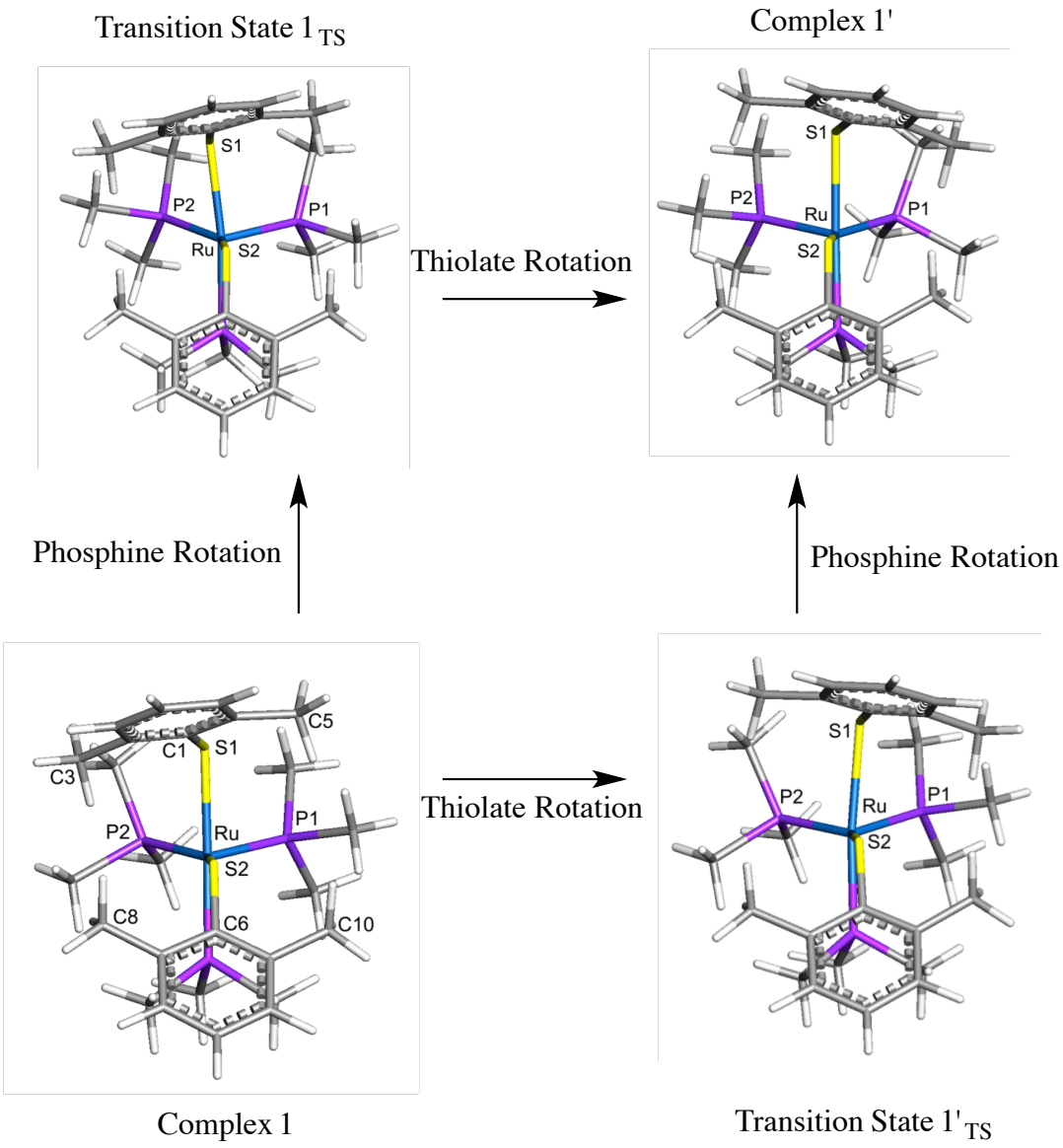

Figure 4.2. Calculated geometry for complex **1** and its electronically equivalent mirror image complex, **1-mirror**. The two minima are connected by the transition state, **TS**, shown here, which a barrier height of 1.59 kcal/mol.

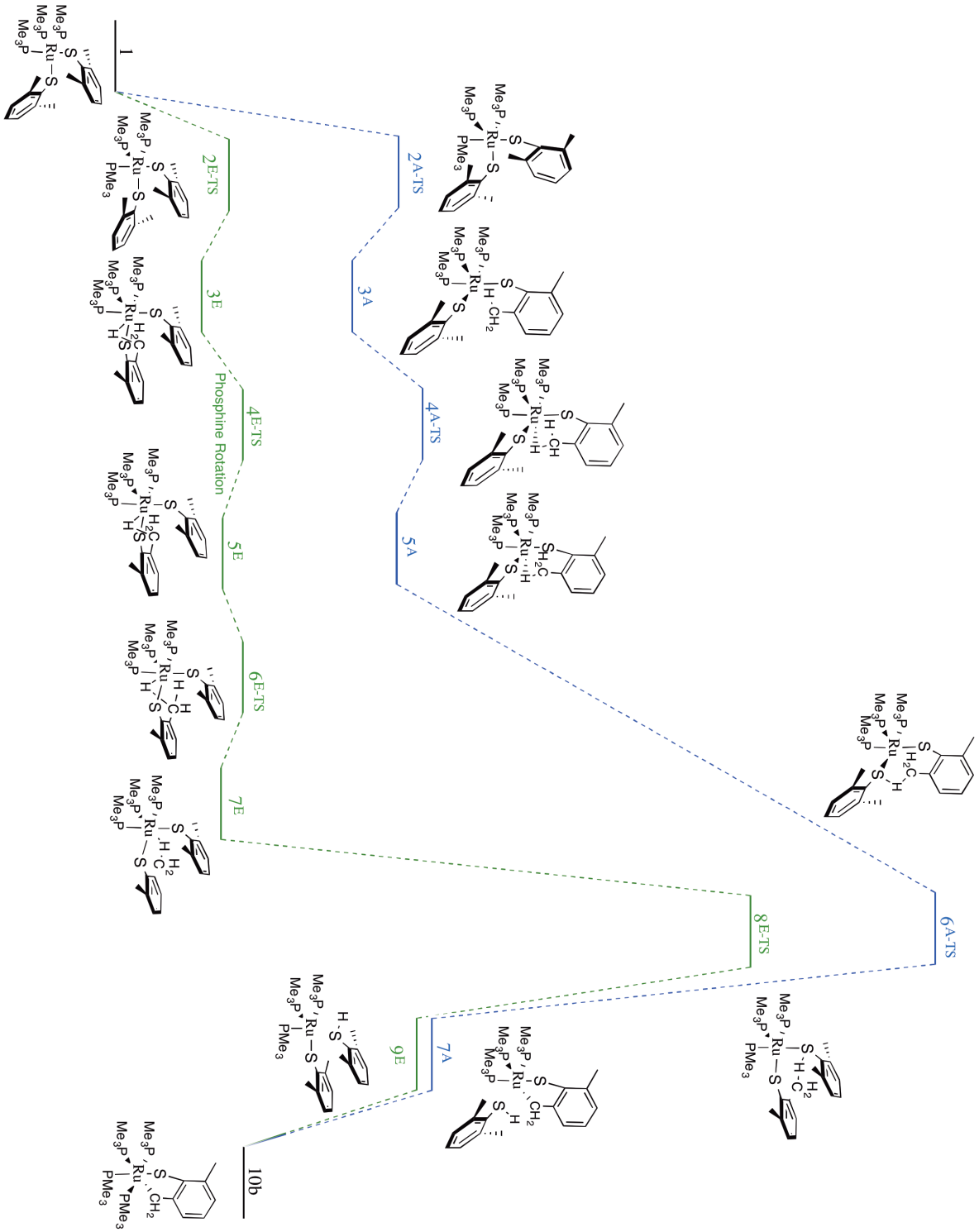

Figure 4.3. Free energy axial and equatorial reaction mechanism

Table 4.2. Electronic Energies, Enthalpies, and Free Energies for the Axial and Equatorial Mechanisms

	Axial Mechanism				Equatorial Mechanism		
	ΔE	**ΔH**	**ΔG**		**ΔE**	**ΔH**	**ΔG**
1	0.00	0.00	0.00	**1**	0.00	0.00	0.00
$2^{A\text{-}TS}$	7.38	7.18	8.98	**$2^{E\text{-}TS}$**	0.05	-0.08	3.62
3^{A}	5.09	5.69	7.56	**3^{E}**	-0.14	0.15	2.70
$4^{A\text{-}TS}$	6.70	6.64	9.86	**$4^{E\text{-}TS}$**	0.94	0.61	3.77
5^{A}	6.69	7.30	9.09	**5^{E}**	1.38	1.51	3.22
$6^{A\text{-}TS}$	26.99	23.52	26.68	**$6^{E\text{-}TS}$**	2.21	1.83	3.86
7^{A}	11.38	9.61	9.93	**7^{E}**	0.56	0.71	3.20
Separated Products	25.04	20.71	6.95	**$8^{E\text{-}TS}$**	19.86	16.57	20.72
10b	1.04	0.73	3.95	**9^{E}**	11.91	9.50	9.44
10m	-8.42	-3.51	14.62	**Separated Products**	25.04	20.71	6.95
				10b	1.04	0.73	3.95
				10m	-8.42	-3.51	14.62

undergo C-H activation. As shown in **Figure 4.4**, when a vacant site is formed on the Ru center the 3p lone pair (LP) on S(2) must interact with a filled Ru 4d orbital instead of the unoccupied $4d_{xy}$ it interacts with in the distorted trigonal bipyramidal geometry of complex **1**. When both S LPs are interacting with filled Ru 4d orbitals the most stable geometry for the complex is when each S LP is interacting with separate Ru 4d orbitals instead of both S LPs interacting with the same Ru 4d orbital. When the S LPs interact with the same Ru 4d orbital symmetric and antisymmetric combinations are formed, **Scheme 4.3**. On the other hand, when the S LPs interact with two Ru 4d orbitals, a pair of nearly degenerate symmetric and anitsymmetric molecular orbitals are formed, each S LP destabilizing one Ru 4d orbital. In this structure stability is gained by adopting a geometry that distributes this LP-4d orbital (Pauli) repulsion across a maximum number of orbitals. Although distribution destabilizes a greater number of 4d orbitals, the energy increment in which they are destabilized decreases, which leads to a more stable structure overall. To maintain the most stable S LP orientation the thiolate ligands must move in a concerted manner during the mechanism. Although the movement of the thiolate groups is concerted, the steric repulsion that is incurred during this movement by each ligand is not equal. For example, as the axial thiolate moves to form a σ-interaction with C(3), the C(10) methyl group on the equatorial ligand is sterically repelled by a $P(1)Me_3$ methyl group. Similarly, if the equatorial thiolate ligand rotates to form a σ-interaction with C(8), the C(3) methyl group on the axial thiolate is sterically repelled by a $P(2)Me_3$ methyl group, **Figure 4.5**. In both of these scenarios there is an increase in steric repulsion between the nonactivated thiolate and its adjacent PMe_3 ligand. This

Complex **1**
LUMO

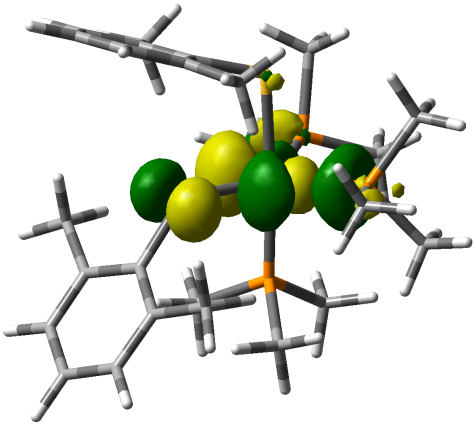

Complex **3**[A]
HOMO

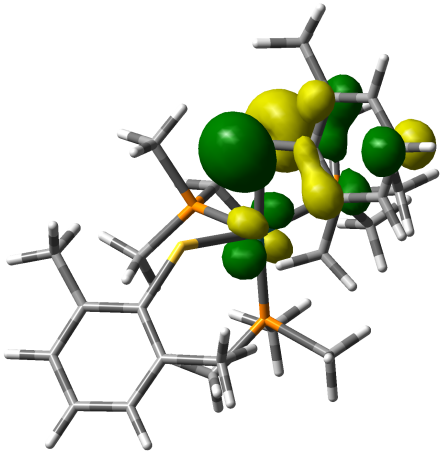

HOMO

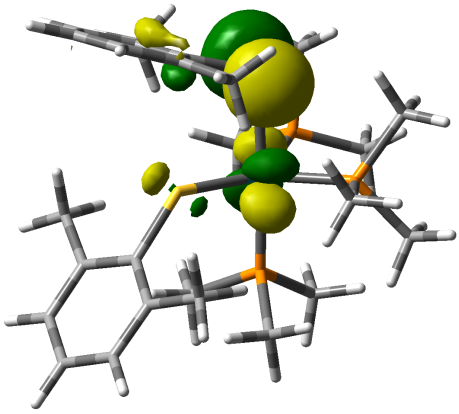

HOMO -1

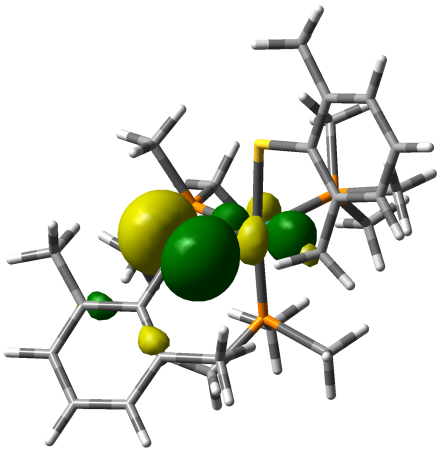

Figure 4.4. In complex **1** the axial S LP is interating with an occupied Ru 4d orbital (HOMO) while the equatorial S LP is interacting with an unoccupied Ru 4d orbital (LUMO). After the equatorial ligand moves to open the sixth coordination site on the Ru center, both the axial (HOMO) and equatorial (HOMO -1) S LPs interact with occupied Ru 4d orbitals.

Stable PMe_3 Orientation

Unstable PMe_3 Orientation

Axial Mechanism

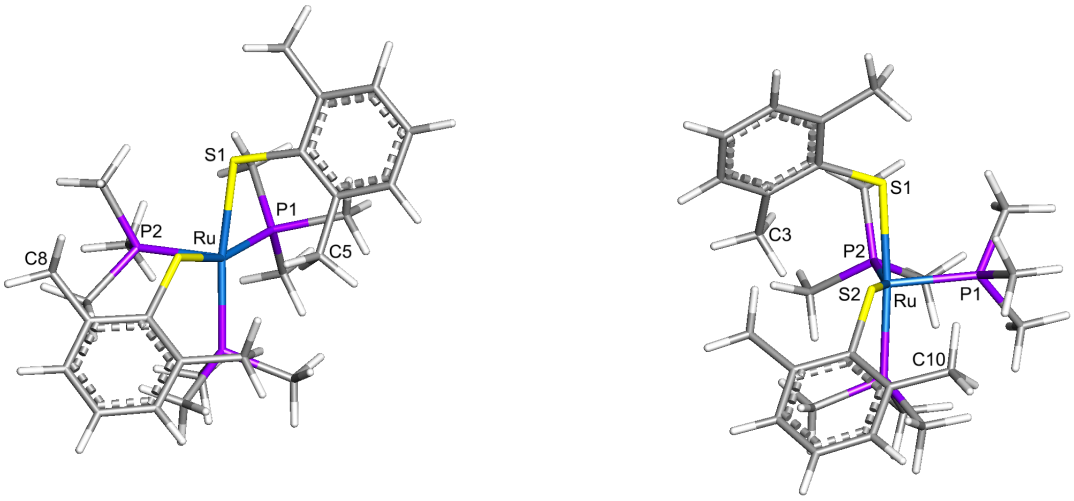

Equatorial Mechanism

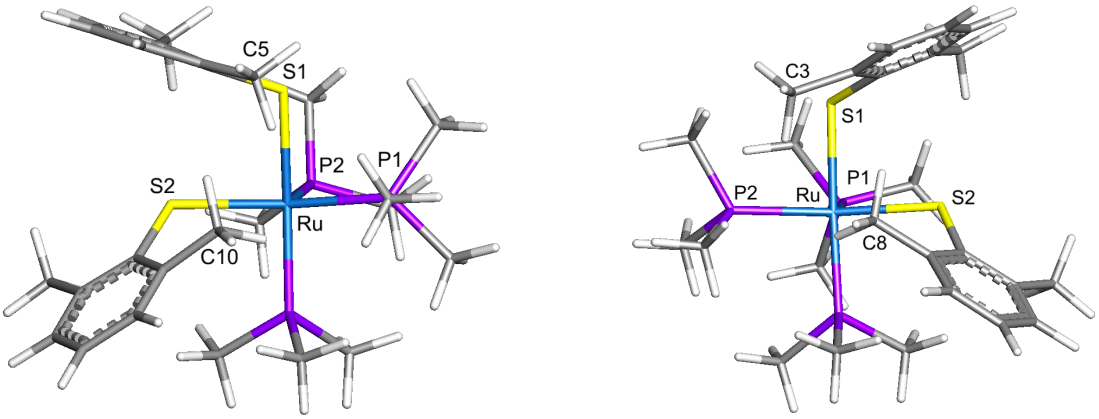

Figure 4.5. In the axial mechansim C(5) activates because C(8) is not sterically hindered by P(2)Me_3, but C(3) does not activate because C(10) is sterically hindered by the P(1)Me_3 ligand. In the equatorial mechanim C(10) activates because C(5) is not sterically hindered by P(1)Me_3, but C(8) does not activate because C(3) is sterically hindered by the P(2)Me_3 ligand.

steric repulsion prevents the activation of C(3) and C(8), but the orientation of the PMe_3 methyl groups allows for the activation of C(5) and C(10). These two activations are referred to as axial and equatorial, respectively.

Scheme 4.3. Molecular orbital diagram of the filled Ru 4d orbitals interacting with the filled sulfur lone pairs.

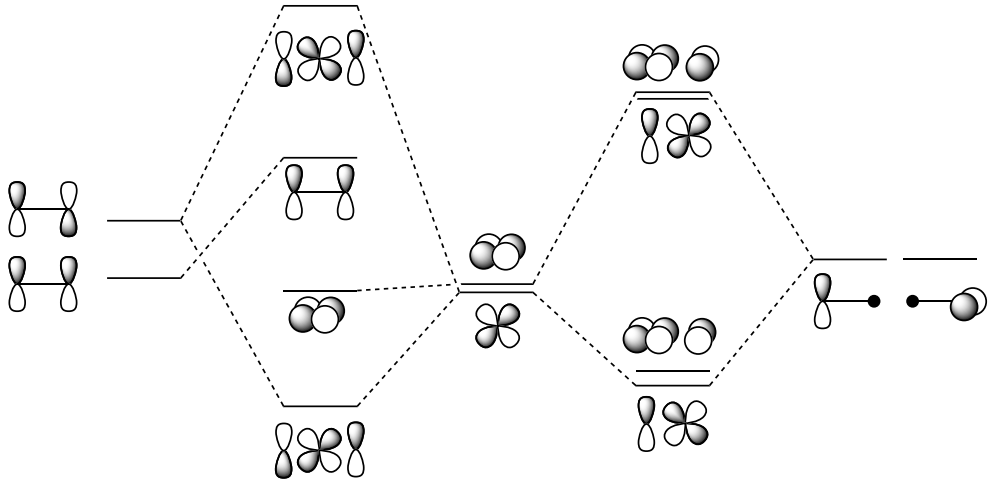

The first step in the axial mechanism is the formation of the σ-complex intermediate, $\mathbf{3^A}$, through transition state $\mathbf{2^{A\text{-}TS}}$, which is the transition state for the attachment of the C(5) C-H bond from complex **1**. This transition state has a free energy barrier of 8.98 kcal/mol relative to complex **1**, and the creation of this transition state involves the rotation of the axial thiolate toward the Ru center, while the equatorial thiolate ligand moves to open a vacant site on the Ru center the S(2)-Ru-P(2) angle

decreases from 142.8° to 91.4°, and the S(2)-Ru-P(1) angle increases from 121.6° to 159.5°. During this process the Ru-S(2) bond distance increases from 2.354 Å to 2.475 Å, because the S(2) lone pair interacts with a filled Ru 4d orbital during the rotation instead of the empty Ru 4d orbital in complex **1**. As shown in **Figure 4.6**, the empty Ru 4d orbital that was previously interacting with the S(2) lone pair in complex **1** is now open to accept electron density from the C-H bond as $\mathbf{2}^{\mathbf{A\text{-}TS}}$ proceeds to intermediate $\mathbf{3}^{\mathbf{A}}$, a stable σ-complex formed between the Ru and the C(5)-H bond that is adjacent to the P(1)Me_3 ligand. Transition state, $\mathbf{4}^{\mathbf{A\text{-}TS}}$ rotates the C(5) methyl group and transitions between the σ-complex in intermediate $\mathbf{3}^{A}$ and the σ-complex in intermediate $\mathbf{5}^{A}$. The C-H bond forming the σ-interaction in intermediate $\mathbf{5}^{A}$, **Figure 4.7**, has a bond distance of 1.116 Å, which is shorter than the 1.129 Å C-H bond length in intermediate $\mathbf{3}^{A}$. This decreased C-H bond length is a result of less electron density being donated into the C-H σ^* molecular orbital from a Ru 4d orbital and is related to the higher free energy of $\mathbf{5}^{A}$ in comparison to $\mathbf{3}^{A}$, 9.09 kcal/mol to 7.56 kcal/mol, respectively. The next step in the mechanism is the C-H activation transition state, $\mathbf{6}^{\mathbf{A\text{-}TS}}$, which has a calculated free energy of 26.68 kcal/mol relative to complex **1**, **Figure 4.7**. In this transition state the C(5)-H and Ru-S(2) bonds are breaking while the S(2)-H and Ru-C(5) bonds are being formed. The transition state shows the rotation of the C(5)H_2 group toward the Ru and the transfer of the activated H atom from the C(5)H_2 group to S(2). The equatorial Ru-S(2) bond bond distance has increased from 2.543 Å in complex $\mathbf{5}^{\mathbf{A}}$ to 2.643 Å in $\mathbf{6}^{\mathbf{A\text{-}TS}}$, which is a result of the weakening S(2)-Ru σ-bond. The Ru-H, C-H, and S-H bond distances are 1.833 Å, 1.615 Å, and 1.609 Å, respectively, and the C-H-S angle is 161.9°

Complex **1**

LUMO

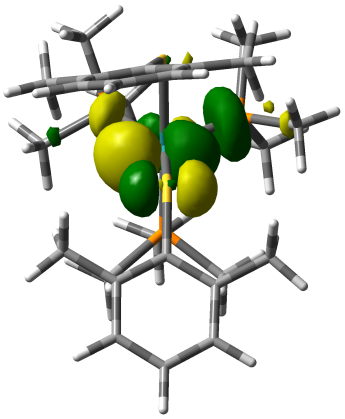

HOMO

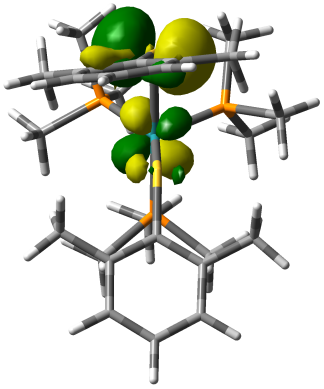

Transition State $\mathbf{2}^{\mathbf{A\text{-}TS}}$

LUMO

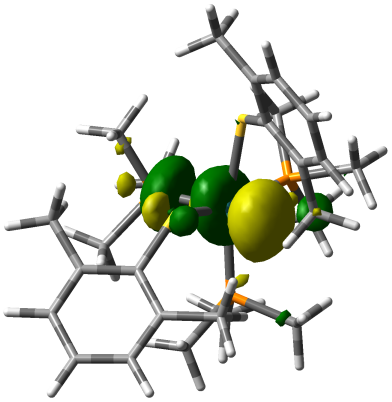

HOMO -1

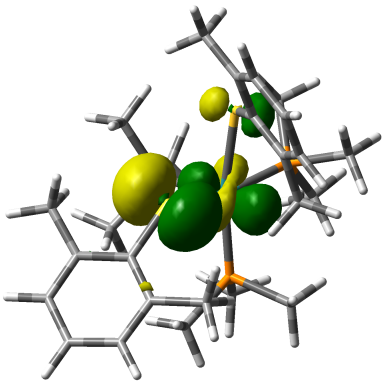

Figure 4.6. The frontier orbitals of complex **1** and $\mathbf{2}^{\mathbf{A\text{-}TS}}$. The LUMO in complex **1** is the antibonding character of the π-interaction between the S(2) lone pair and the unoccupied Ru $4d_{xy}$ orbital while the HOMO is the occupied π-interaction between S(1) and Ru. In $\mathbf{2}^{\mathbf{A\text{-}TS}}$ the S(2) ligand is rotated to open a vacant site on the Ru center. This rotation results in the LUMO becoming an unoccupied Ru 4d orbital that can form the σ-complex intermediate, while the HOMO -1 shows the S(2) lone pair interacting with an occupied Ru 4d orbital.

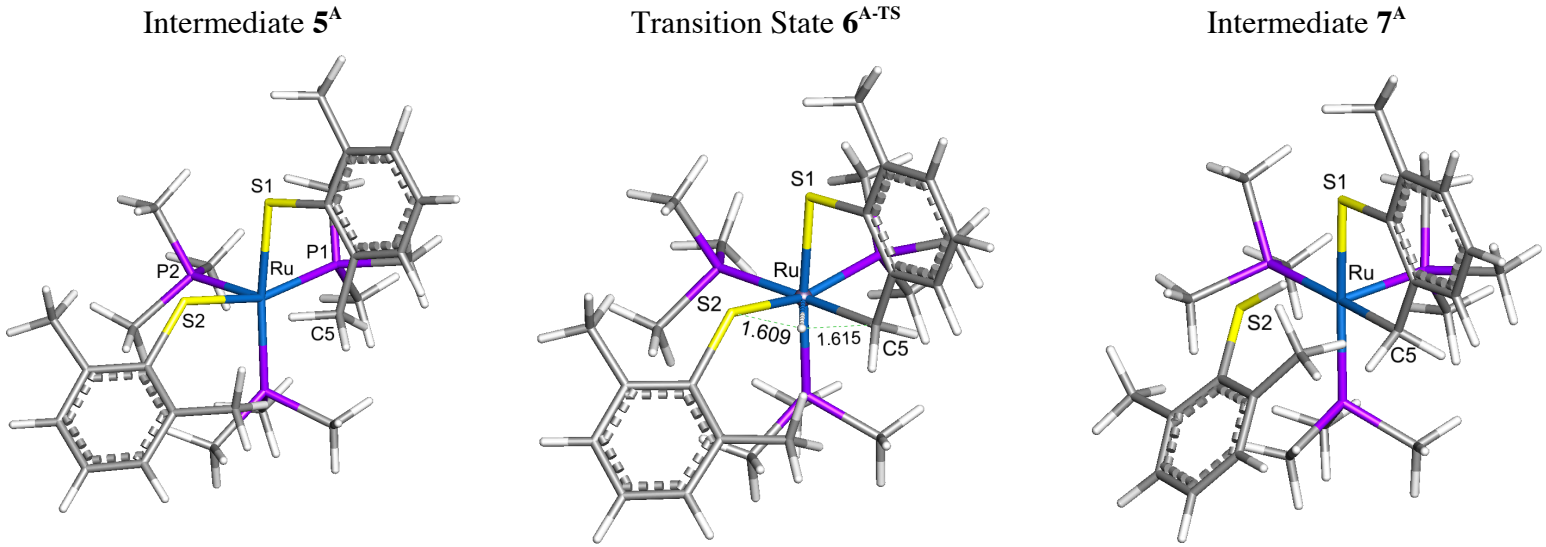

Figure 4.7. The calculated geometries of intermediate $\mathbf{5^A}$, $\mathbf{6^{A\text{-}TS}}$, and $\mathbf{7^A}$. Transition state $\mathbf{6^{A\text{-}TS}}$ is the activation transition state that connects the σ-complex $\mathbf{5^A}$ and the species after the hydrogen transfer $\mathbf{7^A}$.

in $\mathbf{6}^{\mathbf{A\text{-}TS}}$. These bond distance suggest that this is a σ-bond metathesis transition state, and that the Ru does not aid in stabilizing this transition state by interacting with the transferring H atom. A scan of the C(5)-H bond distance was performed to determine if the H would interact with the Ru before the S(2) and undergo an oxidative addition mechanism. However, no stable intermediate was calculated where the H was transferred to the Ru, thus oxidative addtion does not occur in this mechanism. Complex $\mathbf{7}^{\mathbf{A}}$ follows the activation transition state in the reaction mechanism and is a distorted octahedral complex with a weak Ru-S(2) interaction at 2.929 Å. In this intermediate there is no π-interaction between Ru and S(2) because the S LP is now bonding with the transferred H, and the filled Ru 4d orbital that was interacting with the S(2) LP is now a nonbonding Ru 4d orbital, shown in **Figure 4.8**. Intermediate $\mathbf{7}^{\mathrm{A}}$ is 9.93 kcal/mol higher in free energy than complex **1** and is the last intermediate before the complex separates in two species. This intermediate is less stable than the separated products by 2.98 kcal/mol on the free energy surface because entropy favors the separation of the two species, but this intermediate is predicted to exist because on the enthalpic surface, where $\mathbf{7}^{\mathbf{A}}$ is more stable than the separated species by 11.10 kcal/mol. The final product, **10b**, where a fourth PMe_3 ligand binds to the vacant site on the separated Ru species is 3.95 kcal/mol higher in free energy than complex **1**, but is more stable than complex $\mathbf{7}^{\mathbf{A}}$ and the separated species.

The equatorial pathway appears to be longer in comparison to the axial pathway because this mechanism requires the PMe_3 methyl groups to rotate mid-reaction to reduce their steric repulsion. Although there are more steps in this mechanism, the

Intermediate **5**^{A}
HOMO -1

Transition State **6**$^{A\text{-}TS}$
HOMO -1

Intermediate **7**^{A}
HOMO -2

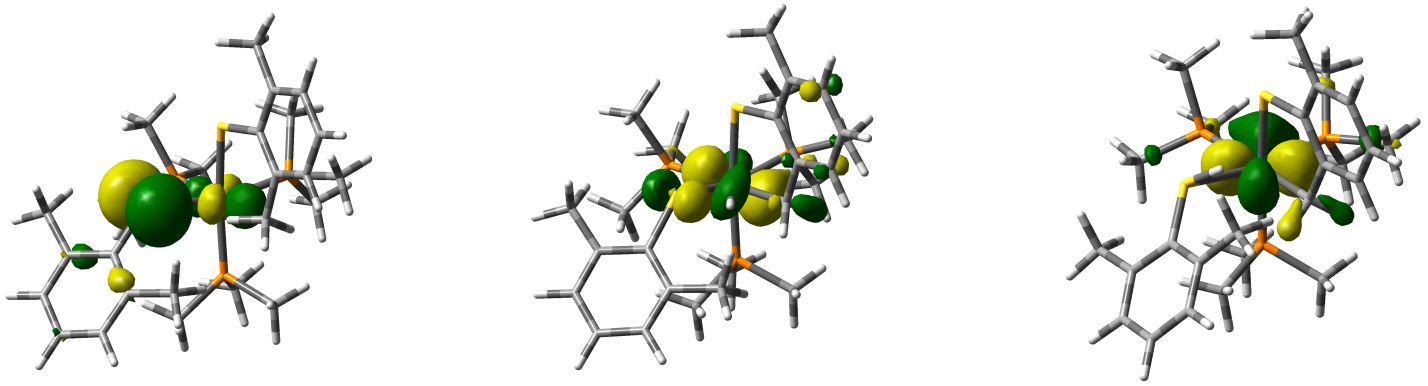

Figure 4.8. The frontier orbitals for **5**^{A}, **6**$^{A\text{-}TS}$, and **7**^{A}. As the axial mechanism proceeds the π-antibonding character between S(2) and the Ru center decreases until there is no π-interaction in **7**^{A}.

overall pathway is lower in energy than the axial mechanism and would dominate during the reaction. The first step in the mechanism is $\mathbf{2}^{\mathbf{E\text{-}TS}}$, the transition state between complex **1** and the first σ-complex intermediate. The $\mathbf{2}^{\mathbf{E\text{-}TS}}$ transition state has a free energy barrier of 3.62 kcal/mol and involves the movement of the S(2) towards P(2) which increases the P(1)-Ru-S(2) angle from 121.6° to 152.6° and decreases the P(2)-Ru-S(2) angle from 142.8° to 109.4°. This transition also brings the C(10) ortho methyl group on the equatorial thiolate into the Ru center while the S LPs maintain their staggered arrangement. As seen in the axial mechanism, the Ru-S(2) bond distance increases from 2.354 Å in complex **1** to 2.466 Å as the S(2) lone pair begins its interact with a filled Ru 4d orbital. The Ru-S(2) bond distance is shorter in the equatorial mechanism because there is less crowding in the equatorial plane, which also relates to the lower energy of $\mathbf{2}^{\mathbf{E\text{-}TS}}$ compared to that of $\mathbf{2}^{\mathbf{A\text{-}TS}}$. The σ-complex intermediate that follows $\mathbf{2}^{\mathbf{E\text{-}TS}}$ is formed with the C-H bond that is adjacent to the axial PMe_3 ligand, and is 2.70 kcal/mol higher in energy than complex **1**. The next step requires a rotation of the P(2)Me_3 methyl groups because the axial thiolate must rotate further towards the P(2) ligand before the second σ-complex can be formed. This transition state, $\mathbf{4}^{\mathbf{E\text{-}TS}}$, has a low free energy barrier of 3.77 kcal/mol. Intermediate $\mathbf{5}^{\mathbf{E}}$ has the phosphine ligands rotated so that C(3) on the axial thiolate can rotate further toward P(2) without an increase in steric repulsion. The low energy barrier transition state, $\mathbf{6}^{\mathbf{E\text{-}TS}}$, which is like the $\mathbf{4}^{\mathbf{A\text{-}TS}}$ in the axial mechanism, rotates the hydrogens on the C(10) ortho methyl group so that the σ-complex is formed by a C-H bond adjacent to S(1). Intermediate $\mathbf{7}^{\mathbf{E}}$ is the σ-complex intermediate before the C-H bond activation transition state, which is more stable than

its axial counterpart, by nearly 6 kcal/mol. This stability is related to the stronger σ-interaction in the equatorial species, which is denoted by longer C-H bond distance in the equatorial species, 1.121 Å compared to the axial 1.116 Å bond distance, and the stabilizing π-π interactions between the two thiolate ligands in $\mathbf{7^E}$, which are not present in $\mathbf{5^A}$**, Figure 4.9**. The C-H bond activation occurs in step $\mathbf{8^{E\text{-}TS}}$ in the equatorial mechanism with a free energy barrier of 20.72 kcal/mol. Transition state $\mathbf{8^{E\text{-}TS}}$ has a Ru-H bond length of 1.809 Å, which is shorter than the $\mathbf{6^{A\text{-}TS}}$ Ru-H bond length of 1.830 Å, but within the M-H bond distance range to still be labeled σ-bond metathesis. The C(10)-H bond distance is 1.593 Å, the S(1)-H bond distance is 1.623 Å, and the C(10)-H-S(1) angle is 168.5°, which, as expected, are comparable to the σ-bond metathesis axial transition state. Again, an attempt was made to locate a stable oxidative addtion intermediate, but, as was seen in the axial mechanism, so seven-coordinate intermediate was calcualted. The shorter C(10)-H bond distance and the longer S(1)-H bond distance suggest that the equatorial transition state is earlier than the axial one, which could be related to the stability of $\mathbf{8^{E\text{-}TS}}$. The final step in the mechanism is complex $\mathbf{9^E}$ where the thiolate ligand is partially dissociated from the Ru complex. The Ru-S bond distance in $\mathbf{9^E}$ is 3.806 Å, which is longer than the 2.928 Å Ru-S bond distance in $\mathbf{7^A}$. However, the intermediate is, again, predicted to be a stable species in the reaction because of the 11.21 kcal/mol enthalpic difference between $\mathbf{9^E}$ and the separated products. The final C-H activated product is the same for both reaction mechanisms and is more stable than the separated products and intermediate $\mathbf{9^E}$. Since the rate determining C-H activation step is predicted to be about 6 kcal/mol lower in energy for the equatorial pathway, this

Intermediate $\mathbf{7}^{\mathbf{E}}$ Transition State $\mathbf{8}^{\mathbf{E\text{-}TS}}$ Intermediate $\mathbf{9}^{\mathbf{E}}$

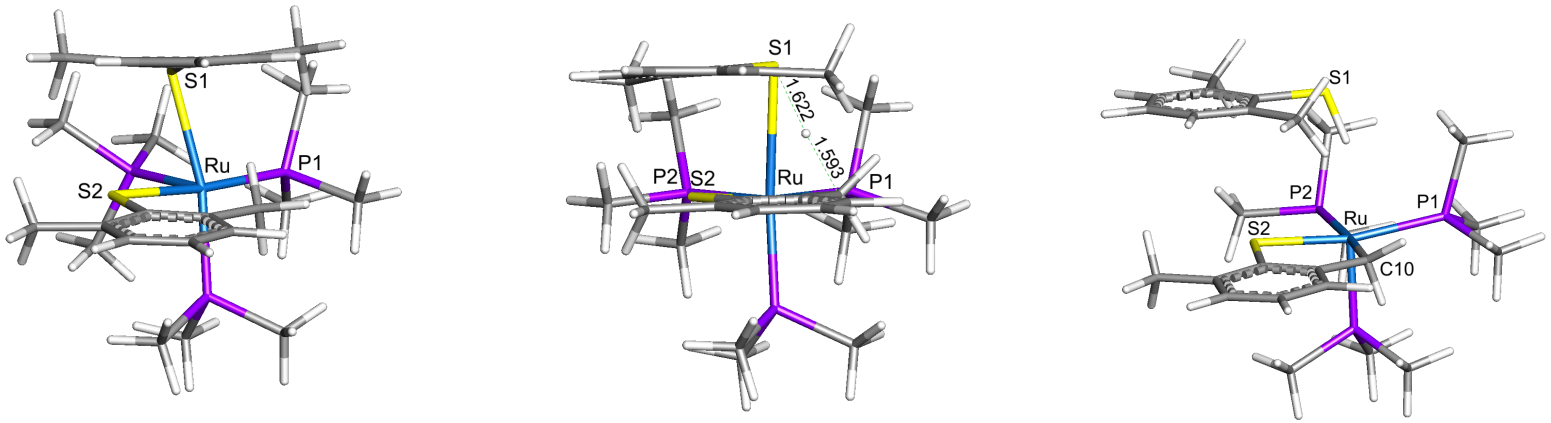

Figure 4.9. Calculated geometry of intermediate $\mathbf{7}^{\mathbf{E}}$, σ-bond metathesis transition state $\mathbf{8}^{\mathbf{E\text{-}TS}}$, and intermediate $\mathbf{9}^{\mathbf{E}}$. The π-π interaction that is formed in $\mathbf{7}^{\mathbf{E}}$ is continued through transition state $\mathbf{8}^{\mathbf{E\text{-}TS}}$ and $\mathbf{9}^{\mathbf{E}}$, but is not seen in the axial mechanism. This stabilizing interaction is related to the lower energy of the equatorial mechanism.

pathway will dominate in the formation of the **10b**, the product seen exclusively in benzene solution.

4.3.3 Solvent Influence

The experimental reaction was predicted to form complex **10m** in 100% yield in methanol without any detection of **1** or the C-H activated product. Although only **10b** is observed as a product in benzene, in methonal there is no CH- activated product observed and the only product seen at essentially 100% yield is **10m**.[109] Because NMR detected no other products in methanol, the solvent must interact or change complex **1** in a way that prevents the formation of a σ-complex and or block the intramolecular C-H activation. Both explicit and implicit approaches to the incorporation of solvents effects, were examined to understand how methanol influences C-H activation in this system so dramatically compared to benzene. The explicit method incorporates a discrete methanol molecule in the gas-phase geometry optimization of **1** to determine the complexes interaction with the solvent molecules. The implicit method optimized the geometry of complex **1** with the PCM method to determine if the geometry of complex **1** is affected by bulk solvation effects.

Complex **1** was optimized with an explicit methanol molecule interacting in two different manners, **Figure 4.10**. The first complex optimized the methanol molecule between the two rings on the thiolate ligands to determine if the solvent stabilized the rings enough to prevent their rotation. The geometry of $\mathbf{1}^{\mathbf{Explicit}}_{\mathbf{Thiolates}}$ has two partially positive hydrogen atoms on the methanol molecule interacting with the negatively charged π-

Complex $\mathbf{1}^{\text{Explicit}}_{\text{Thiolates}}$ Complex $\mathbf{1}^{\text{Explicit}}_{\text{Ru}}$

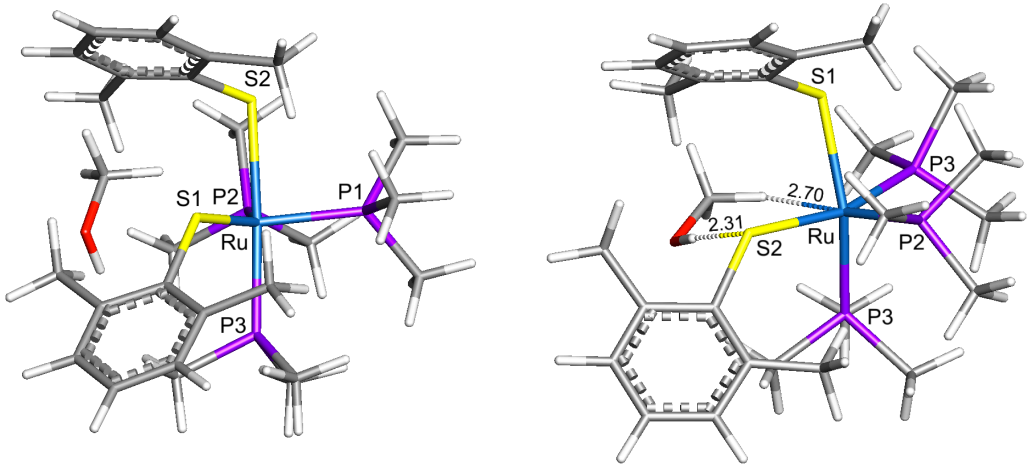

Figure 4.10. Calculated geometires for the explicit solvent method. Complex $\mathbf{1}^{\text{Explicit}}_{\text{Thiolates}}$ has a discrete methanol molecule interacting with the electron π-cloud on both thiolate rings, and $\mathbf{1}^{\text{Explicit}}_{\text{Ru}}$ has a methanol molecule interating with S(2) and the Ru center.

cloud on the both thiolate rings. This electrostatic interaction stabilizes the enthalpic energy of $\mathbf{1}^{\text{Explicit}}_{\text{Thiolates}}$ by 8.62 kcal/mol relative to complex **1**. However, this stabilization does not prevent the rotation of either thiolate ligand. Two scans of the thiolate ligand's movement during $\mathbf{2}^{TS}$ were conducted, but the methanol interaction did not significantly change the energy profile of the scans, which predicted that a single methanol in this orientation would not prevent the production of **10b**. The second geometry tested the methanol's ability to interact with the Ru center. The optimized complex of $\mathbf{1}^{\text{Explicit}}_{\text{Ru}}$ maintained a distorted octahedral geometry, but the methanol molecule did remain close to the Ru. The Ru-CH_3 distance was calculated to be 2.70 Å while the S(2)-OH distance was 2.31 Å, which relates to a stronger interaction between methanol and the thiolate ligand than methanol and the Ru center. An attempt was made to optimize a geometry with the oxygen on the methanol interacting with the Ru, but a converged geometry was not found. Neither of the geometries optimized with explicit solvent yielded a conclusion as to why C-H activation does not occur when solvated with methanol.

The implicit method mimics the effects of bulk solvent interacting with a system and can allow for a more accurate picture of a complex in solution. As shown in **Figure 4.11** and **Table 4.3**, when the geometry of complex **1** was optimized in methanol the final structure of $\mathbf{1}_{\text{ML}}$ was a distorted square-based pyramid geometry with P(1)-Ru-S(2) and P(2)-Ru-S(2) angles of 101.6° and 162.7°, respectively. The axial thiolate ligand is rotated toward the open binding site with a C(2)-S(2)-S(1)-C(1) dihedral angle of 63.6°, compared to the gas phase dihedral angle of 86.7°. This change in geometry is due to the polarity of methanol, which changed the geometry of complex **1** to one with a higher

Complex $\mathbf{1}_{ML}$ Complex $\mathbf{1}_{BZ}$

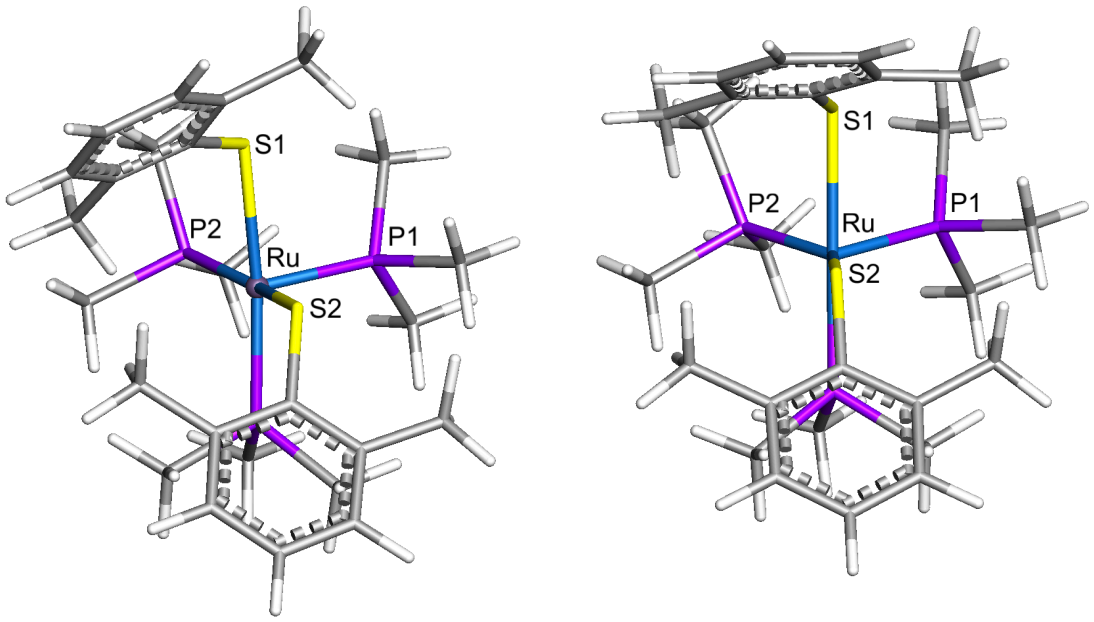

Figure 4.11. Calculated geometies of complex **1** optimized in methanol, $\mathbf{1}_{ML}$, and benzene, $\mathbf{1}_{BL}$. Complex $\mathbf{1}_{ML}$ adopts a distorted square-based pyramidal geometry, but complex $\mathbf{1}_{BZ}$ maintains the distorted trigonal bipyramidal geometry of complex **1**.

Table 4.3. Bond Distances (Å) and Angles (°) for Complex **1** Optimized in the Gas Phase and in Methanol

	Gas Phase	Methanol	Benzene
Ru-S(1)	2.541	2.550	2.551
Ru-S(2)	2.354	2.500	2.365
Ru-P(1)	2.234	2.219	2.243
Ru-P(2)	2.280	2.317	2.278
P(1)-Ru-S(2)	121.6	101.6	125.0
P(2)-Ru-S(2)	142.9	162.7	140.0
P(1)-Ru-P(2)	93.4	93.0	93.1
C(6)-S(2)-S(1)-C(1)	135.1	63.6	170.5

dipole moment; the dipole moment of **1** in the gas phase is 2.73 while the dipole moment of $\mathbf{1_{ML}}$ 5.67. An explicit methanol molecule was optimized in the vacant site of complex $\mathbf{1}_{ML}$ first with the HO- directed towards the Ru, $\mathbf{1_{ML}^{OH}}$, and second with the CH_3- directed towards the Ru, $\mathbf{1_{ML}^{CH_3}}$, **Figure 4.12**. Although a stable interaction was found, the calculated free energies of $\mathbf{1_{ML}^{OH}}$ and $\mathbf{1_{ML}^{CH_3}}$ were higher than complex **1** by 15.47 and 14.22 kcal/mol, respectively. Complex **1** was also optimized with the PCM parameters for benzene to compare the calculated geometry of $\mathbf{1_{ML}}$ with that of the benzene-optimized geometry, $\mathbf{1_{BZ}}$. As shown in **Figure 4.11** and **Table 4.3**, $\mathbf{1_{BZ}}$ converged to the distorted trigonal bipyramidal geometry, with P(1)-Ru-S(2), P(2)-Ru-S(2), and P(1)-Ru-P(2) angles of 125.0°, 140.0°, and 93.1°, respectively. The dipole moment of $\mathbf{1_{BZ}}$ is 3.41, which, as expected, is less than the dipole moment of $\mathbf{1_{ML}}$. The geometry difference between $\mathbf{1_{ML}}$ and $\mathbf{1_{BZ}}$ support the conclusion that the formation of **10m** in methanol is related to the distorted square-based pyramidal geometry that is adopted by complex **1** in methanol. This geometry encourages the binding of a fourth PMe_3 ligand, which produces **10m**. However, the altered geometry of complex **1** would not definitively exclude the formation of **10b**, and further calculations are needed to explore this idea.

4.4 Conclusion

The intramolecular carbon-hydrogen bond activation of an ortho methyl group on one of the 2,6-dimethylbenzenethiolato ligands on the $Ru^{II}(SC_6H_3Me_2\text{-}2,6\text{-}\kappa^1S)_2(PMe_3)_3$ complex occurs in ~30 minutes at standard temperature and pressure. The reactant was determined to proceed to the final C-H activated product, *cis*-Ru[SC_6H_3-(2-CH_2)(6-Me)-

$\kappa^2S_2C](PMe_3)_4$, through an equatorial pathway. The steps in this pathway were influenced by the electronic interactions between the sulfur lone pairs and the Ru 4d orbitals and the steric repulsion between the methyl groups on the five ligands. A change in solvent from benzene to methanol prevents the activation of the ortho methyl group and instead produces an unwanted six-coordinate $Ru(SC_6H_3Me_2\text{-}2,6\text{-}\kappa^1S)_2(PMe_3)_4$ species in 100% yield. This experimental observation was predicted to be a result of the change in geometry of complex **1** when it is solvated in methanol. The polarity of methanol alters the geometry of complex **1** from the less polar distorted trigonal bipyramidal geometry to a more polar distorted square-based pyramidal geometry. Although the geometry is altered when optimized in methanol, it is still unclear if this geometry change would prevent the formation of **10b**.

Complex $\mathbf{1}_{ML}^{OH}$ Complex $\mathbf{1}_{ML}^{CH_3}$

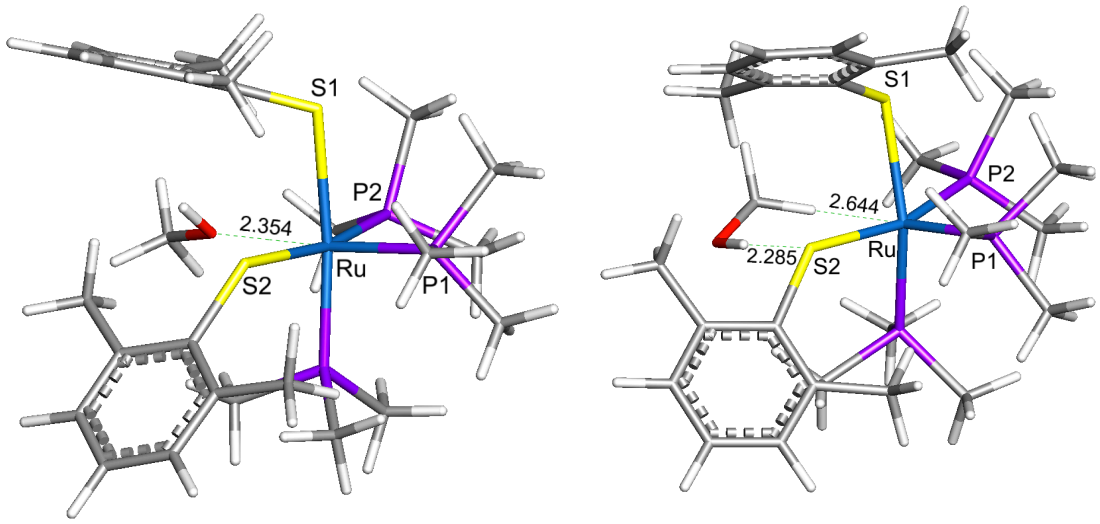

Figure 4.12. Calculated geometies of $\mathbf{1}_{ML}$ with explicit methanol molecules interacting with the open binding site on the distorted square-based pyramidal geometry.

CHAPTER V

CALCULATING A COPPER(I) TRANSFER MECHANISM FOR ATOX1 WITH DENSITY FUNCTIONAL THEORY

5.1 Introduction

Copper, the third most abundant metal in the human body, is essential for proper function.[115] Although copper is needed for many reactions, it is hazardous as an uncomplexed ion. Free copper ions can form radicals and reactive oxygen species (ROS) that are highly destructive and potentially fatal.[116] Understanding how the body maintains proper copper homeostasis is important in preventing or curing diseases associated with a build up or lack of copper. Several diseases known to be caused by an improper Cu(I) balance are Menkes disease,[115] familial amyotrophic lateral sclerosis,[117] and Wilson's disease.[118] Although these diseases are genetic and can not be cured, they can be treated, but improving treatments depends on acquiring a deeper understanding of copper transfer inside the cell.[118] In addition, a build up of copper ions has also been linked to Alzheimer's[119] and prion[120] diseases. To maintain homeostasis, the body relies on ion binding metallochaperones, proteins, and other cuprophilic ligands to move Cu(I) around as a complexed metal. The proteins that bind Cu(I) are highly specific and most have a conserved, CX_1X_2C, binding site motif, where X is a nonconserved amino acid that is not directly involved in the binding of Cu(I).[121]

There are several regulatory pathways for copper inside the cell, and each starts with the uptake of Cu(I) through a Ctr permease. These high-affinity copper transporters

have methionine and cysteine binding sites that coordinate copper as it enters the cell.[122] Once in the cytoplasm there are three destinations for a copper ion, the CcO enzyme in the mitochondria, the copper/zinc superoxide dismutase 1 (SOD1), or the ATPase proteins in the Golgi apparatus, **Scheme 5.1**. The ions are transferred to these destinations via metallochaperones that are specific to each path. Cu(I) is delivered to the CcO enzyme by the Cox17 metallochaperone,[123] and the CCS metallochaperone carries Cu(I) to the SOD1 where it is used to protect the cell against ROS.[124] The Atox1 metallochaperone carries Cu(I) to the Golgi apparatus where it is then transferred to a metal binding domain of ATP7A or ATP7B. These ATPase proteins have four regions, the N-terminal, the transmembrane region, the ATP-binding region, and the phosphatase region. The N-terminal region, which is ~650 amino acids long, is separated into six independently folded, 70-residue long domains. Inside each of the six domains, referred to herein as a metal binding domain (MBD), is a CX_1X_2C Cu(I) binding site that can accept Cu(I) from the Atox1 chaperone.[125] After passing through the regions of the ATP7A or ATP7B the Cu(I) is then incorporated into vesicles or copper-dependent enzymes and is removed from the cell.[126] All of the Cu(I) proteins work in conjunction to maintain balance inside the cell, and although most proteins that participate in each pathway have been elucidated, the mechanisms in which the copper ions are transferred from one protein binding site to the next has not been definitively determined. Since the Atox1 chaperone has been fully characterized via NMR,[127] and most of the MBDs of ATP7A[128-133] and ATP7B[134,135] have also been determined, this copper pathway is among the most extensively studied.

Scheme 5.1. The three main Cu(I) pathways inside the human cell with a metallochaperone specific to each destination. Copper is transferred from the chaperones to the acceptor protein or enzyme depending on the path.

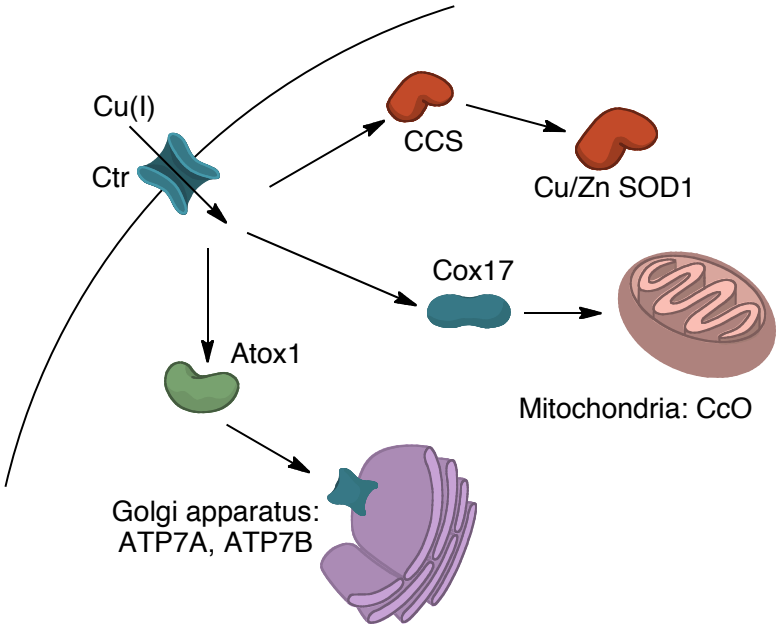

The first mechanism for Cu(I) transfer between two CX_1X_2C binding sites was proposed by O'Halloran and coworkers in 1997.[136] The mechanism included both two- and three-coordinate Cu-bridged intermediates between the yeast chaperone, Atx1, and the acceptor protein, Ccc2 (homologs of the human Atox1 chaperone and the ATP7A or ATP7B acceptor proteins). Cu(I) was proposed to initially bind to the N-terminal Cys on the Ccc2 binding site and form a three-coordinate species, then form a two-coordinate intermediate by the breaking the S-Cu bond of Cys15 on Atx1, followed by a second three-coordinate intermediate by forming a Cu-S bond with the Ccc2 C-terminal Cys,

and concluding with the copper only bound by the two Cys on the Ccc2 binding site **Scheme 5.2**. The validity of this mechanism was supported by experimental NMR structures of the 2-coordiante holo-Atox1 geometry[127] and a crystal structure of an Atox1-Cu(I) dimer[137] which has a 3-coordinate Cu(I) environment. In 2007 the delivery of Cu(I) from Atox1 to the fourth metal binding domain on the ATP7A protein was computationally probed with quantum mechanics/molecular mechanics (QM/MM) calculations. They predicted that a 4-coordinate, tetrahedral intermediate is energetically unfavorable, and the 2-coordinate and 3-coordinate species proposed previously were more likely to play a role in the transfer between binding sites.[138] Another QM/MM study was published in 2010 which argued that 4-coordinate and 2-coordinate intermediates are too high in energy to occur along the transfer pathway, so a transfer incorporating only 3-coordinate species was proposed.[139] Although the relative energies in these studies gave insight into the stabilities of alternative geometries for the intermediates along plausible transfer pathways, no transition states were reported, and without calculated transition states a definitive pathway cannot be predicted.

Scheme 5.2. Proposed mechanism for the transfer of Cu(I) from the Atx1 binding site to the Ccc2 binding site via 2-coordiante and 3-coordinate intermediates. The Atx1 protein is shown in green and the Ccc2 acceptor protein is shown in blue.

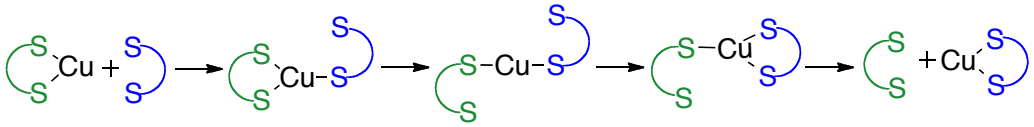

A

comprehensive Cu(I) transfer mechanism for Atox1 is addressed in this work. The first part of this paper is dedicated to exploring the electronic structure and the bonding of Cu(I) methylthiolate model species, $[Cu(SCH_3)_2]^{-1}$, $[Cu(SCH_3)_3]^{-2}$, $[Cu(SCH_3)_4]^{-3}$, with density functional theory (DFT) and molecular orbital theory. These models were studied to determine the most stable coordinations and geometries for Cu(I)-thiolate species. The conclusions from the models were then used to help calculate the transfer of Cu(I) from an Atox1 binding site model to a MBD on the ATP7A or ATP7B protein modeled by the dithiotreitol (DTT) ligand.

5.2 Computational Details

All theoretical calculations were performed with the Gaussian09 suite of programs,[39] and the B3LYP[18,19] functional. The basis set for the 2-coordinate and 3-coordinate Cu(I) methylthiolate models, $[Cu(SCH_3)_2]^{-1}$, $[Cu(SCH_3)_3]^{-2}$, was the Pople-type 6-31G*[41,42] basis set for all C, H, N and O atoms and the 6-311G*[112] basis set for all S atoms. The Stuttgart fully relativistic 10-electron effective core potential and double-ζ basis set were used for Cu.[140] For the 4-coordinate model, $[Cu(SCH_3)_4]^{-3}$, four basis sets were used because the convergence of a tetrahedral 4-coordinate species could not be consistently achieved. Basis set 1 (BS1) was the same basis set as the other 2-coordinate and 3-coordinate models, BS2 used 6-311++G**[84] for C, H, and S atoms and cc-PVDZ[141] for the Cu, BS3 used 6-311++g** for C, H, and S atoms and cc-PVTZ[141] for the Cu, and BS4 used 6-311++g** on C, H, and S atoms and cc-PVQZ[141] for the Cu. Since the models are anionic they were optimized in solution with the polarizable

continuum model (PCM),[46] the radii and non-electrostatic terms for Truhlar and coworkers' SMD solvation model,[47] and the solvation parameters corresponding to water to prevent an inaccurate delocalization of the negative charge toward the formation of a Rydberg-like state which can occur in gas-phase optimizations of anions.

The starting geometry for the Atox1 model was obtained from the protein data bank entry for 1TL4.[125] Since 1TL4 is a published NMR structure thirty separate geometries were reported for this one entry. To ensure a precise minimum energy geometry for the model, five geometries were extracted from the database and optimized. Initial geometries were optimized both in the gas-phase and in solution. The species calculated in the gas phase are not reported in this work because the protein backbone structure in the model was not accurately maintained. However, when the solvent was included in the optimization calculations, the protein backbone in the model maintained an accurate structure, and therefore are reported herein. The structures in the transfer mechanism were also calculated in solution to insure accuracy with the model species, and to prevent delocalization of the negative charge. Analytical frequency calculations were performed on all final structures to ensure that either a minimum or first-order saddle point was achieved. The 3D molecular structures displayed in this article were drawn by using the JIMP2 molecular visualization and manipulation program.[52]

5.3 Results and Discussion

5.3.1 $[Cu(I)(SCH_3)_2]^{-1}$

The 2-coordinate Cu(I) methylthiolate species was used to investigate the electronic structure of the anionic complex that forms in the CX_1X_2C binding site. The Cu(I) methylthiolate model converged to a near linear geometry about the Cu center with a S-Cu-S angle of 177.2°, which is similar to the experimental Atox1 S-Cu-S angle of 160°,[127] and a C-S-S-C dihedral angle optimized to 80.3°, **Figure 5.1**. To examine the π interaction between the S 3p and the Cu 3d orbitals a 360° scan was performed on the S-C-C-S dihedral angle. The scan calculated an energy potential with the lowest energy geometries having a 90° or 270° C-S-S-C dihedral angle and the highest energy confirmations having a 180° or 0° C-S-S-C dihedral angle**, Figure 5.2**. The potential energy for the geometry change is dominated by the interactions of the lone pair (LP) S 3p orbitals that are perpendicular to the C-S-Cu plane with the corresponding Cu 3d orbitals. To confirm that the LP-3d interaction is dictating the geometry of $[Cu(SCH_3)_2]^{-1}$, the electronic energy difference, ΔE, was calculated for the 180° and 90° geometries as a neutral singlet without the Cu atom. At a S-S bond distance of 4.38 Å, the optimized S-S distance for the $[Cu(SCH_3)_2]^{-1}$ model, the ΔE is 0.05 kcal/mol, in favor of the 90° geometry. For the $[Cu(SCH_3)_2]^{-1}$ species the perpendicular geometry is 1.24 kcal/mol more stable than the planar geometry, so the perpendicular geometry, although favored by the S-S interaction is mostly influenced by the LP-3d interaction. As shown in **Figure 5.3**, in the planar (0° or 180°) structure the S LPs form symmetric and antisymmetric confirmations with one of the filled Cu 3d π orbitals. On the other hand, in the

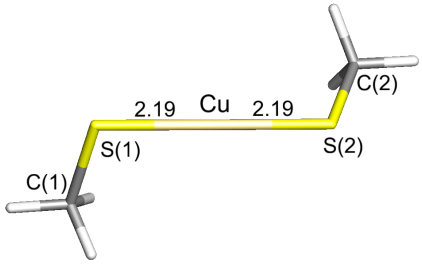

2-coordinate

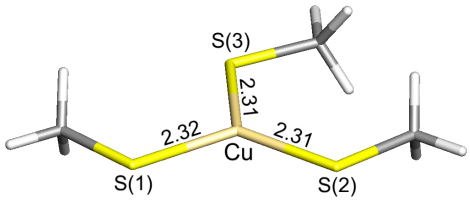

3-coordinate

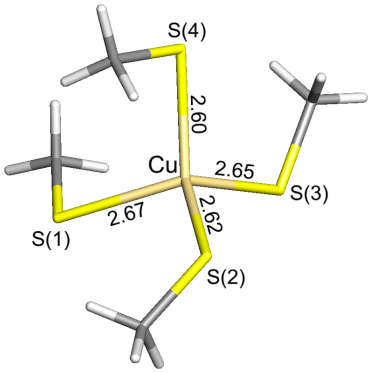

4-coordinate

Figure 5.1. The calculated minimum energy geometries for the Cu(I) methylthiolate model complexes. The 2-coordinate model is most stable in a linear geometry with a C-S-S-C dihedral angle of 80.3°. The trigonal planar, 3-coordinate species has elongated Cu-S bonds compared to the 2-coordinate model, and the C-S-S-C dihedral angles are ~0°. The 4-coordinate complex is not a stable species and was not consistently converged.

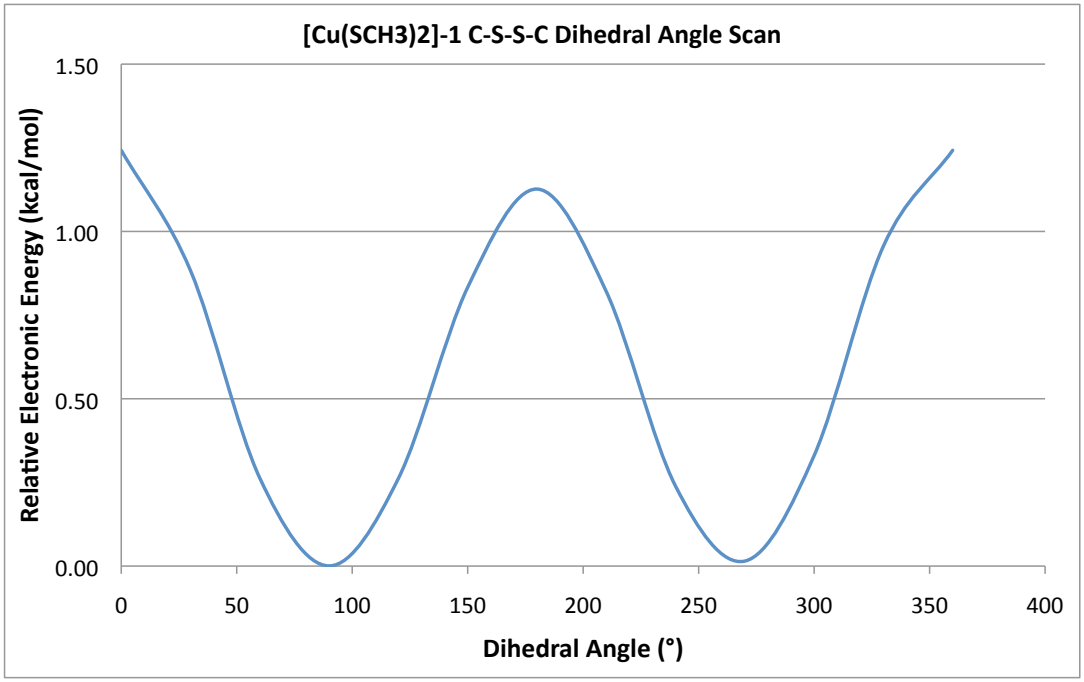

Figure 5.2. The potential energy for the scan of the C-S-S-C dihedral angle of $[Cu(SCH_3)_2]^{-1}$. The most stable angles are 90° and 270° when the methyl groups are staggered, and the least stable angles are 0° and 180° where the methyl groups are either eclipsed or anti.

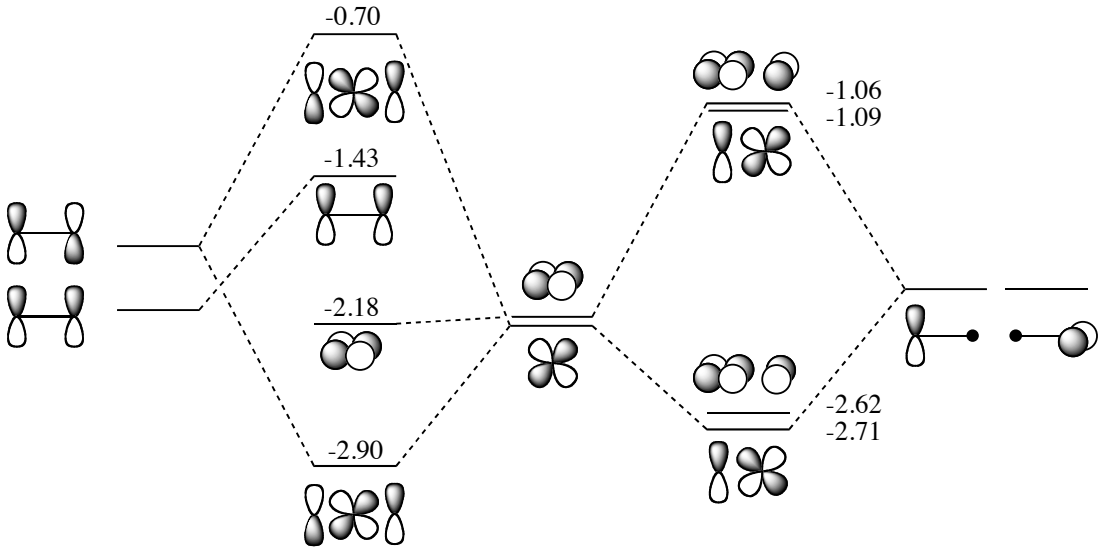

Figure 5.3. Molecular orbital diagrams for the 2-coordinate methylthiolate copper complexes. The two copper d orbitals mix with the sulfur p orbitals differently depending on the C-S-S-C dihedral angle. The 90° dihedral forms near degenerate bonding and antibonding orbitals with the two Cu d orbitals while the 180° dihedral can only mix with one of the Cu d-orbitals.

perpendicular (90° or 270°) geometries the S LPs interact with two Cu 3d π orbitals. The filled Cu 3d orbitals are destabilized when they interact with the filled S LP orbitals because of increased electron repulsion. In this electron-rich structure stability is gained by adopting a geometry that distributes this LP-3d electron repulsion across a maximum number of orbitals. Although distribution destabilizes a greater number of 3d orbitals, the energy increment in which they are destabilized decreases, which leads to a more stable structure overall. The preferred, ~90° dihedral angle is seen in the NMR and crystal structures of the apo-Atox1, and was an important factor when calculating the transfer mechanism.

5.3.2 $[Cu(I)(SCH_3)_3]^{2-}$

The 3-coordinate methylthiolate complex was optimized as a doubly anionic, singlet species. The coordination around the Cu center converged to a trigonal planar geometry with the methyl groups in the same plane as the Cu and S atoms, **Figure 5.1**. Although the placement of the methyl groups is different, the bonding in the 2-coordinate and 3-coordinate models is determined by the same concept. Having all of the atoms in the same plane positions the S LPs perpendicular to the C-S-Cu plane where they form π interactions with the Cu $3d_{xz}$ and $3d_{yx}$ orbitals while the S 3p orbitals in the C-S-Cu plane form the σ interactions with the Cu $3d_{xy}$ and $3d_{x^2-y^2}$ orbitals. The alternative to this geometry would be one in which the methyl groups are not in the S-Cu plane. If the methyl groups were rotated out of the C-S-Cu plane the π interactions would also be rotated, and if the C-S-Cu angle rotated to 90° the S LP would be in the

same plane as the S-Cu σ interactions. This 90° structure is higher in energy than the planar stucture because the two Cu 3d orbitals that were interacting with the S 3p orbitals are now also interacting with the S LPs, so the antibonding orbitals are destabilized by a larger quantity because the distribution of the 3d-LP electron repulsion is decreased.

5.3.3 $[Cu(I)(SCH_3)_4]^{3-}$

The 4-coordinate geometry around Cu(I) has been the most controversial coordination for these systems. Cu(I) forms tetrahedral complexes with one-electron donor ligands with low-lying π antibonding orbitals that can accept electron density like CN^- or CH_3CN, however with soft, two-electron donating ligands like sulfur or phosphorous derivatives, Cu(I) favors a 2- or 3-coordinate geometry. Zn(II), another d^{10} metal, readily forms tetrahedral geometries with ligands, but these geometries are stable because the Zn(II) 3d orbitals are smaller in size than the Cu(I) 3d orbitals and therefore the repulsion between the filled 3d orbitals and filled ligand orbitals is minimized.[137] NMR structures have reported linear, trigonal planar, and tetrahedral bonding schemes between Cu(I) and Atox1, but the tetrahedral geometry is always distorted with an elongated fourth Cu-S bond.[127,137] The 4-coordinate, tetrahedral model was examined to determine the plausability of a 4-coordinate intermediate in the transfer mechanism. Four different basis sets were used, and during the geometry optimization with BS1, BS2, and BS4, two of the methylthiolate ligands broke their Cu-S bonds and rearrange to form interactions with the methyl hydrogens of the two methylthiolate ligands that

remain bound. Upon convergence the species adopted the near linear, 2-coordinate geometry with two unbound ligands. BS3, however, seemed to have the appropriate balance of basis functions to converge a tetrahedral geometry with an average Cu-S bond length of 2.64 Å, **Figure 5.1**. The convergence with BS3 is most likely an artifact of the specific basis set because with BS4, which has a larger Cu basis set and the same S, C, H basis sets, the tetrahedral geometry does not converge. The failure to consistently optimize a tetrahedral structure lends further support to the previous conclusions that the transfer mechanism does not have a 4-coordinate intermediate.

5.3.4 Transfer Mechanism

The binding site of the Atox1 chaperone contains the four residues Cys12-Gly13-Gly14-Cys15, so to create a model of this section the full protein was terminated before Cys12 and after Cys15. To retain more of the protein backbone structure the Cys residues were not truncated at the α-carbon, but were extended a few atoms beyond, as shown below in skeletal rendering of the model.

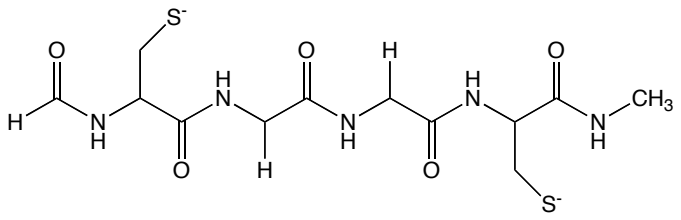

For Cys12 the NH group was included, and to maintain the sp^2 hybridization of the nitrogen a CHO group was also included in the model. Since Cys15 is more imbedded in the protein matrix than Cys12, this end of model was extended further to include the CO group from the Cys15 residue, the NH group from the 16^{th} residue, and was terminated with a methyl. The apoprotein was optimized as a protonated neutral species, a singly deprotonated anionic species, and a fully deprotonated dianion, while the holoprotein was optimized as a deprotonated anionic complex. All four of the converged model geometries show good agreement with the experimental structures when optimized in solution, (Appendix D). The DTT ligand was chosen to act as a model for the acceptor MBD on the ATP7A or ATP7B because its structure is similar to the CX_1X_2C binding site and its small size allowed for DFT calculations to be performed without large computational cost. Also, the S atoms have near free rotation, which is important since different C-S-S-C dihedral angles were shown to stabilize the 2-coordiante and 3-coordinate Cu(I) methylthiolate species. The two chiral carbons on the DTT ligand can have either R,R or R,S chirality, and, although the R,S symmetry is the more stable geometry, the R,R symmetry was used because it mimics the geometry of the acceptor's binding site better than the R,S, **Figure 5.4**.

The transfer mechanism, **Figure 5.5**, begins with the two separated reactants, Cu(I) bound to the Atox1 model and the free anionic DTT ligand, which are the zero relative energy for the transfer mechanism. The first intermediate is the 3-coordinate species, **1,** where the Cu is bound to Cys12 and Cys15 on the Atox1 model, S(1) and S(2), respectively, and one deprotonated S from the DTT ligand, S(3). Complex **1** was

(a)

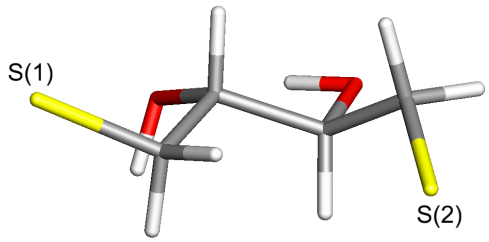

(b)

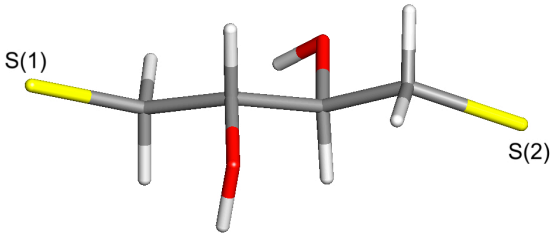

Figure 5.4. The optimized geometries for the doubly anionic diasteromers (a) R,R and (b) R,S confirmations of the DTT ligand. The R,S confirmation has a lower relative energy, but the R,R confirmation was used for the acceptor protein's binding site model in the transfer mechanism because the geometry is more representative of the real acceptor's binding site.

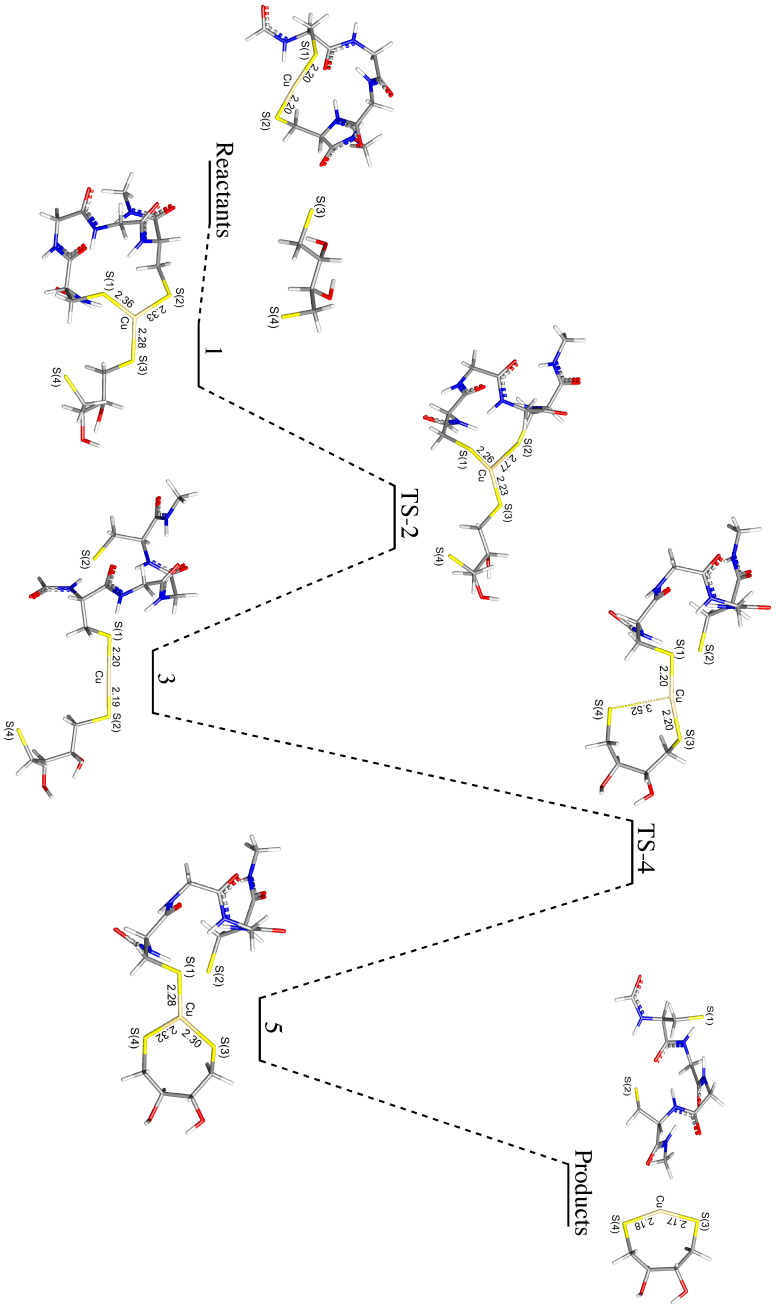

Figure 5.5. Enthalpy surface for the transfer of Cu(I) from the Atox1 binding site model to the DTT ligand. The transfer begins with the Cu-bound Atox1 binding to S(3) from the DTT ligand and ends Atox1 releasing Cu so it is bound solely by DTT.

optimized every 60° of the 360° C-S(3)-Cu-S(2) dihedral rotation, since the DTT ligand has free rotation about the Cu-S(3) bond. Two stable confirmations were converged from this scan, each having a C-S(3)-Cu-S(2) dihedral angle of ~0° (See Supplemental Information). The dihedral angles in these two confirmations are similar to the dihedrals calculated for the 3-coordinate Cu(I) methylthiolate. Aside from the rotation about the Cu-S(3) bond, the DTT ligand can also rotate about the S(3)-C bond in this species, and when scans were run about the S(3)-C bond for the two intermediates, four more geometries were converged. The free energy differences separating the six converged species is less than 1 kcal/mol, so the orientation of the DTT ligand for **1** was chosen by comparing the calculated geometries with the acceptor's binding site geometry. Intermediate **1** has a trigonal planar geometry around the Cu center and an average S-Cu bond length of 2.32 Å. The DTT ligand binds with Cu so that Cu-S(3)-C are planar, but the C-S(1)-S(2)-C dihedral angle is 71.4° so neither of methyl groups on the Atox1 model are in the same plane as the Cu-S(3)-C. The C-S(1)-S(2)-C dihedral angle nearly identical to the 72.0° C-S-S-C dihedral angle in the 2-coordinate Atox1 model, which is believed to be caused by the rigidity of the Atox1 model's backbone. From the analysis of the $[Cu(I)(SCH_3)_3]^{-2}$ model we would assume that this intermediate would be more stable if all three of the C-S-S-C dihedral angles were ~0°, however maintaining a less stable geometry might produce a lower energy transition state and possibly a faster transfer. The first transition state in the mechanism, **TS-2**, is the cleaving of the S(2)-Cu bond on the Atox1 model. The S(2)-Cu bond was broken first instead of the S(1)-Cu bond because Cys15 is located deeper inside the protein matrix than the largely solvent

exposed Cys12, and the Cu-Cys15 bond has been experimentally predicted to break first.[23] Most of the rearrangement in the transition state is concentrated around the S(2) and Cu atoms as their bond is cleaved, but, as this is occurring, the S(1)-Cu-S(3) angle is also expanding to the 2-coordinate, linear geometry. The relative enthalpy barrier for **TS-2** is low, 2.99 kcal/mol, which leads one to assume that the breaking of the S(2)-Cu bond occurs quickly. Intermediate **3** is the lowest energy species during the transfer, and it is the only intermediate with a 2-coordinate geometry, aside from the reactants and products. The Cu-S bond lengths have decreased from an average of 2.32 Å in **1** to 2.19 Å, the S(1)-Cu-S(3) angle has increased to 176.7°, and the C-S(1)-S(3)-C dihedral angle has increased to 78.5°. The bonding at the Cu center is very similar to the bonding in the $[Cu(I)(SCH_3)_2]^{-1}$ complex, where the LPs on the two S atoms form a π intereaction with two Cu 3d orbitals instead of only one. In step four of the transfer, **TS-4**, the second, 3-coordinate complex is formed as S(4) transitions to bond with the Cu. In this transition state the CH_2 group bound to S(3) has to rotate 180° to allow S(4) to bind to the Cu. **TS-4** has a relative enthalpy of 6.14 kcal/mol compared to **1** in the mechanism. For the final intermediate of the mechanism the Cu-S bond distances are elongated back to an average of 2.30 Å while the 3-coordinate, trigonal planar geometry is assumed. The binding scheme in **5** is similar to that of **1** with the roles of the two binding sites reversed. The Atox1 model now has free rotation because it is only bound by S(1), so it assumes a C-S(1)-Cu-S(4) dihedral angle of 3.6° which would allow for the ideal interactoin between the S LP and Cu 3d orbitals. Although the Cu-S binding and orientation is the same in **1** and **5**, the DTT ligand experiences more ring strain overall compared to the Atox1

model, so the relative free energy for **5** is higher than **1**. The final products are higher in energy than the reactants, but for the actual transfer between Atox1 and an ATP7A or ATP7B MBD this is not the case because the binding sites on these proteins have been experimentally determined to have a higher affinity for Cu(I) than Atox1. An intermediate such as **5** in a transfer mechanism where the acceptor is a model of a MBD and not DTT could have a lower energy than the reactants which would mimic the experimental binding affinities. On the other hand, the instability of **5** might encourage breaking the Cu-S(1) bond faster since the 2-coordinate product is more stable.

5.5 Conclusion

The electronic structure of Cu(I) methylthiolate models were used to calculated plausible mechanistic pathway for the transfer of Cu(I) from a model of Atox1's Cu(I) binding site to a DTT ligand. The $[Cu(SCH_3)_2]^{-1}$ model showed an increase in stability with a C-S-S-C dihedral angle of 90° compared to a 180° dihedral which was also observed in the Atox1 and DTT 2-coordinate complexes. In the trigonal planar, 3-coordinate complex stability is obtained by maintaining a more planar geometry around the Cu center which distributes the LP-3d electron repulsion across the maximum number of π-bonding interactions. A 4-coordinate, tetrahedral model of $[Cu(SCH_3)_4]^{-3}$ could not be consistently converged, and from the molecular orbital diagram of the complex, a 4-coordinate geometry is not likely to be stable. These conclusions were applied to calculate a dissociative mechanism that encompassed five steps which include 2-coordinate and 3-coordinate stationary points connected by low energy transition

states.

CHAPTER VI

CONCLUSION

6.1 Conclusion

The electronic structure and mechanistic details of four, late transition metal systems were successfully calculated in this work with density functional theory and moderate sized basis sets. The first system was the reaction between a Br_2 and the Ni^{II}(2-phenylpyridine)(Br)(2-picoline) complex which produced an Ar-Br bond via reductive elimination at the Ni^{II} center. The high energy Ni^{IV} oxidation state is avoided during the reaction by moving from the single state surface to the triplet state surface by forming a Ni^{III}/Br_2^- interaction. Since Ni is a cheaper metal than its d^{10} counterparts this account of singlet/triplet flexibility should encourage the use of Ni in a wider range of reactions.

The second system in this study was the carbon-hydrogen activation of four cycloalkanes with the Cp'Rh^{I}(CO) (Cp' = cyclopentadiene or pentamethylcyclopentadienye) fragment. The experimental lifetime trends were predicted to be a result of the increasing number of unique C-H bonds that can be activated in the increasing size of the cycloalkane ring. The varying C-H bonds form a range of σ-complex stabilities and activation barrier energies that also increase with ring size. As the energy range increases the reaction begins to favor ring-migrations so the lower energy σ-complexes can be activated more readily. Populating the σ-complexes with the lowest energy activation barrier reduces the overall lifetime, but for this to be thermodynamically feasible the migration barriers must be lower in energy than the

activation barriers. For cyclopentane, cyclohexane, and cycloheptane there is little to no decrease in lifetime with the inclusion of ring-migrations in the reaction mechanism because the energy of migrating around the ring is too high in comparison to the activation energies. However, the cyclooctane reactions require the addition of ring-migrations to accurately calculate reaction lifetimes. This difference with cyclooctane is a result of an increase in sterics, which leads to less stable σ-complexes and, therefore, higher energy activation barriers and lower energy migration barriers.

The third system was concerned with the intramolecular carbon-hydrogen bond activation of $Ru^{II}(SC_6H_3Me_2\text{-}2,6\text{-}\kappa^1S)_2(PMe_3)_3$. For this reaction two plausible mechanisms, axial and equatorial, were calculated to produce the final C-H activated product, *cis*-$Ru[SC_6H_3\text{-}(2\text{-}CH_2)(6\text{-}Me)\text{-}\kappa^2S_2C](PMe_3)_4$. The equatorial mechanism provided a lower free energy barrier of activation and was predicted to be the dominating pathway for the reaction. The unactivated product, $Ru(SC_6H_3Me_2\text{-}2,6\text{-}\kappa^1S)_2(PMe_3)_4$, that was formed in methanol was predicted to be a result of the square-based pyramidal geometry that is adopted by complex **1** when solvated in methanol, which has an open binding site where the excess PMe_3 in the reaction can bind.

The final transition metal system dealt with the transfer mechanism of Cu(I) between the Atox1 metallochaperone and the acceptor proteins ATP7A or ATP7B. The electronic strucutre of the $[Cu(SCH_3)_2]^{-1}$ model showed an increase in stability with a C-S-S-C dihedral angle of 90° compared to a 180° dihedral which distributes the LP-3d electron repulsion across the maximum number of π-bonding interactions. The method of stabilization was also observed in the 3-coordinate methylthiolate model, and in the

intermediates along the reaction path between the Atox1 model and DTT ligand. These conclusions were applied to calculate an associative mechanism that encompassed five steps that include 2-coordinate and 3-coordinate stationary points connected by low energy transition states.

6.2 Future Work

Two of the four chemical systems presented in this dissertation require future work. The first system is the carbon-hydrogen activation of cycloalkanes with cyclopentadienylcarbonylrhodium and the second system is the intramolecular carbon-hydrogen activation of bis(2,6-dimethylbenzenethiolato)tris(trimethylphosphine)ruthenium(II).

In the intermolecular C-H activation project all eight of the reactions are scaled with CCSD(T) calculations from the CpRh(CO)-cyclohexane reaction. Although scaling all of the activation and migration barriers with one scaling factor yielded good results, the CCSD(T) calculations will be performed on the Cp*Rh(CO)-cyclohexane reaction to determine if they Cp*Rh(CO) reactions should be scaled by a different factor.

In the intramolecular C-H activation project the support for why the C-H activation does not occur in methanol was not complete. The change in geometry of complex **1** from the distorted triogonal bipyramidal geometry to the distorted square-based pyramidal geometry is an important factor in preventing C-H activation, but the reaction needs to be further explored in methanol to support this conclusion.

This work will be completed before publication of these two systems.

REFERENCES

1. (a) Hagen, J. *Industrial Catalysis A Practical Approach, Second Edition* Wiley VCH, **2006**, Weinheim, Germany. (b) Torrent, M.; Sola, M.; Frenking, G. *Chem. Rev.* **2000**, *100*, 439. (c) Keim, W. *Angew. Chem. Int. Ed.* **1990**, *29*, 235. (d) Thorp, H. H.; Pecoraro, V. L. *Mechanistic Bioinorganic Chemistry* American Chemical Society **1995**, *246*.

2. (a) Hoffman, B. M.; Lukoyanov, D.; Dean, R. D.; Seefeldt, L. C. *Acc. Chem. Res.* **2013**, *46*, 587. (b) Grapperhaus, C. A.; Darensbourg, M. Y. *Acc. Chem. Res.* **1998**, *31*, 451. (c) Tinberg, C. E.; Lippard, S. J. *Acc. Chem. Res.* ***2011****, 44,* 280.

3. (a) Lyons, T.; Sanford, M. S. *Chem. Rev.* **2010**, *110*, 1147. (b) Fekl, U.; Goldberg, K. I. *Advances in Inorganic Chemistry* **2003***, 54*, 259. (c) Colby, D. A.; Tsai, A. S.; Bergman, R. G.; Ellman, J. A. *Acc. Chem. Res.* **2012**, *45*, 814.

4. (a) Boisvert, L.; Goldberg, K. I. *Acc. Chem. Res.* **2012**, *45*, 899. (b) Michelini, M. d. C.; Russo, N.; Sicilia, E. *Inorg. Chem.* **2004**, *43*, 4944. (c) Tolman, W. B. *Acc. Chem. Res.* **1997**, *30*, 227.

5. Davidson, E. R. *Chem. Rev.* **2000**, *100*, 351.

6. Higgs, Andrew J.; Zinn, Paul J.; Simmons, Sarah J.; Sanford, Melanie S. *Organometallics* **2009**, *28*, 6142.

7. Renz, A. L.; Perez, L. M.; Hall, M. B. *Organometallics* **2011**, *11*, 6365.

8. Pitts, A. L.; George, M. W.; Hall, M. B. *In prep.*

9. Hirano, M.; Togashi, S.; Ito, M.; Sakaguchi, Y.; Komine, N.; Komiya, S. *Organometallics* **2010**, *29*, 3146.

10. Huffman, D. L.; O'Halloran, T. V. *Annu. Rev. Biochem.* **2001**, *70*, 677.

11. Pitts, A. L.; Hall, M. B. *Submitted*

12. Roothan, C. C. *J. Rev. Mod. Phys.* **1960**, *32*, 179.

13. (a) Møller, C.; Plesset, M. S. *Phys. Rev.* **1936**, *46*, 618. (b) Pople, J. A.; Binkley, J. S.; Seeger, R. *Int. J. Quantum Chem.* **1976**, *S10*, 1.

14. Bartlett, R. H. *Ann. Rev. Phys. Chem.* **1981**, *32*, 359.

15. Kohn, W.; Sham, L. J. *Phys. Rev. A* **1965**, *140*, 1133.

16. Vosko, S. J.; Wilk, L.; Nussair, M. *Can. J. Phys.* **1980**, 1200.

17. Becke, A. D. *Phys. Rev. A* **1988**, *38*, 3098.

18. Lee, C.; Ynag, W.; Parr, R. G. *Phys. Rev. B* **1988**, *37*, 785.

19. Becke, A. D. *J. Chem. Phys.* **1993**, *98*, 5648.

20. Boese, A. D.; Martin, J. M. L. *J. Chem. Phys.* **2004**, *121*, 3405.

21. Zhao, Y.; Truhlar, D. G. *Theor. Chem. Acc.* **2008**, *120,* 215.

22. Tao, J. M.; Perdew, J. P.; Staroverov, V. N.; Scuseria, G. E. *Phys. Rev. Lett.* **2003**, *91*, 146401.

23. Grimme, S. *J. Comp. Chem.* **2006**, *27*, 1787.

24. Becke, A. D. *J. Chem. Phys.* **1997**, *107*, 8554.

25. Chai, J.-D.; Head-Gordon, M. *Phys. Chem. Chem. Phys.* **2008**, *10*, 6615.

26. (a) Kalyani, D.; Sanford, M. S. *J. Am. Chem. Soc.* **2008**, *130*, 2150. (b) Forster, D. *Adv. Organomet. Chem.* **1979**, *17*, 255. (c) Kakiuchi, F.; Kochi, T.; Mutsutani, H.; Kobayashi, N.; Urano, S.; Sato, M.; Nishiyama, S.; Tanabe, T. *J. Am. Chem. Soc.* **2009**, *131*, 11310.

27. (a) Yin, L.; Liebscher, J. *Chem. Rev.* **2007**, *107*, 133. (b) Martin, R.; Buchwald, S. L. *Acc. Chem. Res.* **2008**, *41*, 1461. (c) Terao, J.; Kambe, N. *Acc. Chem. Res.* **2008**, *41*, 1545. (d) Procelewska, J.; Zahl, A.; Liehr, G.; van Eldik, R.; Smythe, N. A.; Williams, B. S.; Goldberg, K. I. *Inorg. Chem.* **2005**, *44*, 7732.

28. (a) Low, J. J.; Goddard, W. A. *Organometallics* **1986**, *5*, 609. (b) Hartwig, J. F.; *Inorg. Chem.* **2007**, *46*, 1936. (c) Crumpton-Bregel, D. M.; Goldberg, K. I. *J. Am. Chem. Soc.* **2003**, *125*, 9442. (d) Low, J. J.; Goddard, W. A. III *J. Am. Chem. Soc.* **1984**, *106*, 8321.

29. Vigalok, A. *Chem. Eur. J.* **2008**, *14*, 5102.

30. (a) Whitfield, S. W.; Sanford, M. S. *J. Am. Chem. Soc.* **2007**, *129*, 15142. (b) Furuya, T.; Ritter, T. *J. Am. Chem. Soc.* **2008**, *130*, 10060. (c) Arnold, P. L.; Sanford, M. S.; Pearson, S. M. *J. Am. Chem. Soc.* **2009**, *131*, 13912.

31. (a) Roy, A. H.; Hartwig, J. F. *J. Am. Chem. Soc.* **2003**, *125*, 13944. (b) Roy, A. H.; Hartwig, J. F. *J. Am. Chem. Soc.* **2004**, *23*, 1533.

32. Powers, D. C.; Ritter, T. *J. Am. Chem. Soc.* **2009**, *1*, 302.

33. (a) Ball, N. D.; Sanford, M. S. *J. Am. Chem. Soc.* **2009**, *131*, 3796. (b) Furuya, T.; Benitez, D.; Tkatchouk, E.; Strom, A. E.; Tang, P.; Goddard, W. A. III; Ritter, T. *J. Am. Chem. Soc.* **2010**, *132*, 3793.

34. (a) Roy, A. H.; Hartwig, J. F. *J. Am. Chem. Soc.* **2001**, *123*, 1232. (b) Goldberg, K. I.; Yan, J. Y.; Winter, E. L. *J. Am. Chem. Soc.* **1994**, *116*, 1573. (c) Goldberg K. I.; Yan, J. Y.; Breitung, E. M. *J. Am. Chem. Soc.* **1995**, *117*, 6889. (d) Yahav-Levi, A.; Goldberg, I.; Vigalok, A.; Vedernikov, A. N. *J. Am. Chem. Soc.* **2008**, *130*, 724. (e) Giri, R., Chen, X. & Yu, J. Q. *Angew. Chem. Int. Edn Engl.* ***2005****, 44*, 2112.

35. C. M. Frech, D. Milstein, J. Am. Chem. Soc. **2006**, 128, 12434.

36. (a) Koo, K.; Hillhouse, G. L.; *Organometallics* **1995**, *14*, 4421. (b) Lin, B. L.; Clough, C. R.; Hillhouse, G. L. *J. Am. Chem. Soc.* **2002**, *124*, 2890.

37. (a) Cotton, F. A.; Wilkinson, G. *Advanced Inorganic Chemistry, 5th Ed.* **1988**, 741. (b) Klein, H.-F.; Bickelhaupt, A.; Jung, T.; Cordier, G. *Organometallics* **1994**, *13*, 2557. (c) Dimitrov, V.; Linden, A. *Angew. Chem., Int. Ed.* **2003**, *42*, 2631.

38. Higgs, Andrew J.; Zinn, Paul J.; Sanford, Melanie S. *Organometallics* **2010**, *29*, 5446.

39. M. J. Frisch, G. W. Trucks, H. B. Schlegel, G. E. Scuseria, M. A. Robb, J. R. Cheeseman, G. Scalmani, V. Barone, B. Mennucci, G. A. Petersson, H. Nakatsuji, M. Caricato, X. Li, H. P. Hratchian, A. F. Izmaylov, J. Bloino, G. Zheng, J. L. Sonnenberg, M. Hada, M. Ehara, K. Toyota, R. Fukuda, J. Hasegawa, M. Ishida, T. Nakajima, Y. Honda, O. Kitao, H. Nakai, T. Veven, J. A. Montgomery, Jr., J. E. Peralta, F. Ogliaro, M. Bearpark, J. J. Heyd, E. Brothers, K. N. Kudin, V. N. Staroverov, R. Kobayashi, J. Normand, K. Raghavachari, A. Rendell, J. C. Burant, S. S. Iyengar, J. Tomasi, M. Cossi, N. Rega, J. M. Millam, M. Klene, J. E. Knox, J. B. Cross, V. Bakken, C. Adamo, J. Jaramillo, R. Gomperts, R. E. Stratmann, O. Yazyev, A. J. Austin, R. Cammi, C. Pomelli, J. W. Ochterski, R. L. Martin, K. Morokuma, V. G. Zakrzewski, G. A. Voth, P. Salvador, J. J. Dannenberg, S. Dapprich, A. D. Daniels, O. Farkas, J. B. Foresman, J. V. Ortiz, J. Cioslowski, and D. J. Fox, *Gaussian 09, Revision A.02;* Gaussian, Inc., Wallingford CT, 2009.

40. (a) Becke, A. D. *Phys. Rev. A* **1988**, *38*, 3098. (b) Perdew, J. P. *Phys. Rev. B* **1986**, *34*, 7406.

41. Hariharan, P. C.; Pople, J. A. *Theoret. Chimica Acta* **1973**, *28*, 213.

42. (a) Petersson, G. A.; Al-Laham, M. A. *J. Chem. Phys.* **1991**, *94*, 6081. (b) Petersson, G. A.; Bennett, A.; Tensfeldt, T. G.; Al-Laham, M. A.; Shirley, W. A.; Mantzaris, J. *J. Chem. Phys.* **1988**, *89*, 2193.

43. Bergner, A.; Dolg, M.; Kuumlchle, W.; Stoll, H.; Preuszlig, H. *Mol. Phys.* **1993**, *80*, 1431.

44. (a) Hay, P. J.; Wadt, W. R. *J. Chem. Phys.* **1985**, *82*, 270. (b) Hay, P. J.; Wadt, W. R. *J. Chem. Phys.* **1985**, *82*, 284. (c) Hay, P. J.; Wadt, W. R. *J. Chem. Phys.* **1985**, *82*, 299.

45. Höllwarth, A.; Böhme, M.; Dapprich, S.; Ehlers, A. W.; Gobbi, A.; Jonas, V.; Köhler, K. F.; Stegmann, R.; Veldkamp, A.; Frenking, G. *Chem Phys Letters* **1993**, *208*, 237.

46. Scalmani G.; and Frisch, M. J. **2009**, in prep.

47. Marenich, A. V.; Cramer, C. J.; and Truhlar, D. G. *J. Phys. Chem. B* **2009**, *113*, 6378.

48. (a) Møller, C.; Plesset, M. S. Phys. Rev. 1934, 46, 618. (b) Pople, J. A.; Binkley, J. S.; Seeger, R. Int. J. Quantum Chem. 1976, 10, 1.

49. Shiozaki, T.; Kamiya, M.; Hirata, S.; Valeev, E. F. *Phys. Chem. Chem. Phys.* **2008**, *10*, 3358.

50. Cossi, M.; Rega, N.; Scalmani, G.; Barone, V. J. Comput. Chem. **2003**, *24*, 669.

51. Krishnan, R.; Binkley, J. S.; Seeger, R.; Pople, J. A. *J. Chem. Phys.* **1980**, *72*, 650.

52. (a) Manson, J.; Webster, C. E.; Hall, M. B. *JIMP2, Version 0.091, a free program for Visualizing and manipulating molecules*; Texas A&M University: College Station, TX, 2006. (b) Hall, M. B.; Fenske, R. F. *Inorg. Chem.* **1972**, *11*, 768.

53. Beaudoin, S.; Zargarian, D.; Belanger-Gariepy, F.; Fontaine, F. *Acta Cryst. Sec. E* **2001**, E57, m433-m434.

54. Unreacted molecular bromine is in a singlet state with a bond distance of 2.28 Å. Adding an electron to the LUMO (σ^*) makes the Br_2^- molecule with a doublet spin ground state and an elongated Br-Br bond distance of 2.98 Å.

55. On the singlet PES, structures **6** and **7-TS** were predicted with the smaller basis set, but were nonexistant with the larger basis set.

56. Labinger, J. A.; Bercaw, J. E. *Nature* **2002**, *417*, 507.

57. Arndtsen, B. A.; Bergman, R. G.; Mobley, T. A.; Peterson, T. H. *Acc. Chem. Res.* **1995**, *28*, 154.

58. Parshall, G. W. *Acc. Chem. Res.* **1975**, *8*, 113.

59. Jensen, C. M. *Chem. Commun.* **1999**, 2443.

60. Crabtree, R. H. *J. Chem. Soc., Dalton Trans.* **2001**, 2437.

61. Chat, J.; Davidson, J. M. *J. Chem. Soc.* **1965**, 843.

62. Sen, A. *Acc. Chem. Res.* **1998**, *31*, 550.

63. Lewis, J. C.; Bergman, R. G.; Ellman, J. A. *Acc. Chem. Res.* **2008**, *41*, 1013.

64. Janowicz, A. H.; Bergman, R. G. *J. Am. Chem. Soc.* **1982**, *104*, 352.

65. Hoyano, J. K.; Graham, W. A. G. *J. Am. Chem. Soc.* **1982**, *104*, 3723.

66. Crabtree, R. H; Mellea, M. F. Mihelcie, J. M.; Quick, J. M. *J. Am. Chem. Soc.* **1982**, *104*, 3723.

67. Jones, J. K.; Feher, F. J. *J. Am. Chem. Soc.* **1982**, *104*, 4240.

68. Janowicz, A. H.; Bergman, R. G. *J . Am. Chem. Soc.* **1983**, *105*, 3929.

69. Weiller, B. H.; Wasserman, E. P.; Bergman, R. G.; Moore, C. B.; Pimentel, G. C. *J. Am. Chem. Soc.* **1989**, *111* , 8288.

70. Saillard, J.-Y.; Hoffman, R. *J. Am. Chem. Soc.* **1984**, *106*, 2006.

71. (a) Ziegler, T.; Tschinke, V.; Ursenbach, C. *J. Am. Chem. Soc.* **1987**, *109*, 4825. (b) Ziegler, T.; Tschinke, V. Becke, A. D. *J. Am. Chem. Soc.* **1987**, *109*, 1351. (c) Ziegler, T.; Tschinke, V.; Versluis, L.; Baerends, E. J.; Ravenek,

W. *Polyhedron* **1988**, *7*, 1625. (d) Ziegler, T.; Wendan, C.; Baerends, E. J.; Ravenek, W. *Inorg. Chem.* **1988**, *27*, 3458.

72. Ziegler, T.; Tschinke, V.; Fan, L.; Becke, A. D. *J. Am. Chem. Soc.* **1989**, *111*, 9177.

73. Song, J.; Hall, M. B. *Organometallics*, **1993**, *12*, 3118.

74. Cundari, T. R. *J. Am. Chem. Soc.* **1994**, *116*, 340.

75. Low, J. J.; Goddard, W. A. *J. Am. Chem. Soc.* **1986**, *108*, 6115.

76. Koga, N.; Morokuma, K. *J. Am. Chem. Soc.* **1990**, *94*, 5454.

77. Balcells, D.; Clot, E.; Eisenstein, O. *Chem. Rev.* **2010**, *110*, 749.

78. Niu, S.; Hall, M. B. *Chem. Rev.* **2000**, *100*, 353.

79. Clot, E.; Eisenstein, O.; Jones, W. D. *Proc. Nat. Acad. Sci. U. S.A.* **2007**, *104*, 6939.

80. George, M. W.; Hall, M. B.; Jina, O. S.; Portius, P.; Sun, X-Z.; Towrie, M.; Wu, H.; Yang, X.; Zaric, S. D. *Proc. Natl. Acad. Sci. U. S. A.* **2010**, *107*, 20178.

81. George, M. W.; Hall, M. B.; Portius, P.; Renz, A. L.; Sun, X-Z.; Towrie, M.; Yang, X. *Dalton Trans.* **2011**, *40*, 1751.

82. (a) Perdew, J. P.; Burke, K.; Ernzerhof, M. *Phys. Rev. Lett.* **1997**, *78*, 1396. (b) Grimme, S. *J. Comp. Chem.* **2006**, *27*, 1787.

83. Krishnan, R.; Binkley, J. S.; Seeger, R.; Pople, J. A. *J. Chem. Phys.* **1980**, *72,* 650.

84. McLean, A. D.; Chandler, G. S. *J. Chem. Phys.* **1980**, *72*, 5639.

85. Clark, T.; Chandrasekhar, J.; Spitznagel, G. W.; Schleyer, P. v. R. *J. Comp. Chem.* **1983**, *4,* 294.

86. (a). Andrea, D.; Haeussermann, U.; Dolg, M.; Stoll, H.; Preuss, H. *Theor. Chim. Acta* **1990**, *77*, 123. (b). Martin, J. M. L.; Sundermann, A. *J. Chem. Phys.* **2001**, *114*, 3408.

87. Cossi, M.; Rega, N.; Scalmani, G.; Barone, V. *J. Comput. Chem.* **2003**, *24*, 669.

88. Hinsberg, W.; Houle, F.; Allen, F.; Yoon, E. *Chemical Kinetics Simulator 1.0.1*; International Business Machines Corporation, Alamaden, CA, 1998.

89. (a) Chat, J.; Davidson, J. M. *J. Chem. Soc.* **1965**, 843. (b) Parshall, G. W. *Acc. Chem. Res.* **1975**, *8*, 113.

90. (a) Janowicz, A. H.; Bergman, R. G. *J. Am. Chem. Soc.* **1982**, *104*, 352. (b) Hoyano, J. K.; Graham, W. A. G. *J. Am. Chem. Soc.* **1982**, *104*, 3723. (c) Crabtree, R. H; Mellea, M. F. Mihelcie, J. M.; Quick, J. M. *J. Am. Chem. Soc.* **1982**, *104*, 3723. (d) Jones, J. K.; Feher, F. J. *J. Am. Chem. Soc.* **1982**, *104*, 4240.

91. Labinger, J. A.; Bercaw, J. E. *Nature* **2002**, *417*, 507.

92. Jones, W. D.; Feher, F. J. *Acc. Chem. Res.* **1989**, *22*, 91. (b) Arndtsen, B. A.; Bergman, R. G.; Mobley, T. A.; Peterson, T. H. *Acc. Chem. Res.* **1995**, *28*, 154. (c) Crabtree, R. H. *Chem. Rev.* **1995**, *95*, 987. (d) Sen, A. *Acc. Chem. Res.* **1998**, *31*, 550. (e) Jones, W. D. *Top. Organomet. Chem.* **1999**, *3*, 9. (f) Ritleng, V.; Sirlin, C.; Pfeffer, M. *Chem. Rev.* **2002**, *102*, 1731. (g) Lewis, J. C.; Bergman, R. G.; Ellman, J. A. *Acc. Chem. Res.* **2008**, *41*, 1013.

93. (a) Watson, P. L.; *J. Am. Chem. Soc.* **1983**, *105*, 6491. (b) Watson, P. L.; Parshall, G. W. *Acc. Chem. Res.* **1985**, *18*, 51.

94. (a) Green, M. L. H.; Knowles, P. J.; *J. Chem. Soc. Chem. Commun.* **1970**, 1677. (b) Crabtree, R. H. *Chem. Rev.* **1985**, *85*, 245.

95. (a) Webster, C. E.; Fan, Y.; Hall, M. B.; Kunz, D. Hartwig, J. F. *J. Am. Chem. Soc.* **2003**, *125*, 858. (b) Hartwig, J. F.; Cook, K. S.; Hapke, M.; Incarvito, C. D.; Fan, Y.; Webster, C. E.; Hall, M. B. *J. Am. Chem. Soc.* **2005**, *127*, 2538.

96. (a) Oxgaard, J.; Muller, R. P.; Goddard, W. A., III; Periana, R. A. *J. Am. Chem. Soc.* **2004**, *126*, 352.

97. Perutz, R. N.; Sabo-Etienne, S. *Angew. Chem., Int. Ed.* **2007**, *46*, 2578.

98. (a) Ng, S. M.; Lam, W. H.; Mak, C. C.; Tsang, C. W.; Jia, G.; Lin, Z.; Lau, C. P. *Organometallics* **2003**, *22*, 641-651. (b) Lam, W. H.; Jia, G.; Lin, Z.; Lau, C. P.; Eisenstein, O. *Chem.sEur. J.* **2003**, *9*, 2775-2782. (c) Lin, Z. *Coord. Chem. Re*V. **2007**, doi:10.1016/j.ccr.2006.11.006.

99. (a) Vastine, B. A.; Hall, M. B. *J. Am. Chem. Soc.* **2007** *129*, 12068. (b) Vastine, B. A.; Hall, M. B. *Coord. Chem. Rev.* **2009**, *253*, 1202. (c) Ess, D. H.; Goddard, W. A. III; Periana, R. A. *Organometallics* **2010**, *29*, 6459.

100. Kubas, G. J. *Metal Dihydrogen and σ-Bond Complexes Structure, Theory, and Reactivity* Kluwer; Academic/Plenum Publishers: New York, 2001.

101. (a) Jones, W. D.; Feher, F. J. *J. Am. Chem. Soc.* **1985**, *107,* 620-631. (b) Janowicz, A. H.; Bergman, R. G. *J. Am. Chem. Soc.* **1983**, *105*, 3929. (c) McAlister, D. R.; Erwin, D. K.; Bercaw, J. E. *J. Am. Chem. Soc.* **1978**, *100*, 5966. (d) Jimenez-Catano, R.; Hall, M. B. *Organometallics* **1996**, *15*, 1889. (e) Strout, D. C.; Niu, S.; Zaric, S.; Hall, M. B. *J. Am. Chem. Soc.* **1996**, *118*, 6068. (f) Niu, S.; Hall, M. B. *J. Am. Chem. Soc.* **1998**, *120*, 6169.

102. (a) Ryabov, A. D. *Chem. Rev.* **1990**, *90*, 403. (b) M. E. van der Boom, D. Milstein, *Chem. Rev.* **2003**, *103*, 1759. (c) Lyons, T. W.; Sanford, M. S. *Chem. Rev.* **2010**, *110,* 1147. (d) Albrecht, M. *Chem. Rev.* **2010**, *110*, 576.

103. (a) Arndtsen, B. A.; Bergman, R. G.; Moley, T. A.; Peterson, T. H. *Acc. Chem. Res.* **1995**, *28*, 154. (b) Crabtree, R. H. *Chem. Rev.* **1985**, *85*, 254. (d) Shilov, A. E.; Shteinman, A. A. *Coord. Chem. Rev.* **1977**, *24*, 97. (c) Wasserman, E. P.; Moore, C. B.; Bergman, R. G. *Science* **1992**, *255*, 315. (d) Kakiuchi, F.; Murai, S. Acc. Chem. Res. 2002, 35, 826. (e) Djukic, J.-P.; Sortais, J.-B.; Barloy, L.; Pfeffer, M. *Eur. J. Inorg. Chem.* **2009**, 817.

104. (a) Levison, J. J.; Robinson, S. D. *J. Chem. Soc., Chem. Commun.* **1968**, 1405. (b) Levison, J.; Robinson, S. D. *J. Chem. Soc.* **1970**, 639.

105. Parshall, G. W.; Knoth, W. H.; Schunn, R. A. *J. Am. Chem. Soc.* **1969**, *91*, 4990.

106. Lewis, L. N.; Smith, J. F. *J. Am. Chem. Soc.* **1986**, *108*, 2728.

107. James, B. R.; Markham, L. D.; Wang, D. K. W. *J. Chem. Soc., Chem. Commun.* **1974**, 439.

108. Toner, A.; Matthes, J.; Gründemann, S.; Limbach, H. H.; Chaudret, B.; Clot, E.; Sabo-Etienne, S. *Proc. Natl. Acad. Sci. USA* **2007**, *104*, 6945.

109. Hirano, M.; Togashi, S.; Ito, M.; Sakaguchi, Y.; Komine, N.; Komiya, S. *Organometallics* **2010**, *29*, 3146.

110. Jiménez-Cataño, R.; Hall, M. B. *Organometallics* **1996**, *15*, 1889.

111. Niu, S.; Hall, M. B. *J. Am. Chem. Soc.* **1998**, *120*, 6169.

112. (a) Krishnan, R.; Binkley, J. S.; Seeger, R.; Pople, J. A. *J. Chem. Phys.* **1980**, *72,* 650. (b) McLean, A. D.; Chandler, G. S. *J. Chem. Phys.* **1980**, *72*, 5639.

113. (a) Peterson, K. A.; Figgen, D.; Dolg, M.; Stoll, H.; *J. Chem. Phys.* **2007**, *126*, 124101.

114. Riehl, J.-F; Jean, Y.; Eisenstein, O.; Pelissier, M. *Organometallics* **1992**, *11*, 729.

115. Tumer, Z.; Moller, L. B. *European Journal of Human Genetics* **2010**, *18*, 511.

116. Cuillel, M. *J Incl Phenom Macrocycl Chem* **2009**, *65*, 165.

117. Rosen, D. R. *Nature* **1993**, 362, 59.

118. Das, K. S.; Ray, K. *Nature* **2006**, *2*, 482.

119. Huang, X. D.; Cuajungco, M. P.; Atwood, C. S.; Hartshorn, M. A.; Tyndall, J. D. A.; Hanson, G. R.; Stokes, K. C.; Leopold, M.; Multhaup, G.; Goldstein, L. E.; Scarpa, R. C.; Saunders, A. J.; Lim, J.; Moir, R. D.; Glabe, C.; Bowden, E. F.; Masters, C. L.; Fairlie, D. P.; Tanzi, R. E.; Bush, A. I. J. Biol. Chem. **1999**, 274, 37111.

120. Viles, J. H.; Cohen, F. E.; Prusiner, S. B.; Goodin, D. B.; Wright, P. E.; Dyson, H. J. Proc. Natl. Acad. Sci. U.S.A. **1999**, 96, 2042.

121. Banci, L.; Bertini, I.; McGreevy, K. S.; Rosato, A. *Nat. Prod. Rep.* **2010**, *27*, 695.

122. Kim, B. E.; Nevitt, T.; Thiele, D. J. *Nat. Chem. Biol.* **2008**, *4*, 176.

123. Cobine, P. A.; Pierrel, F.; Bestwick, M. L.; Winge, D. R. *J. Biol. Chem.* **2006**, *281*, 36552.

124. O'Halloran, T. V.; Culotta, V. C. *J. Biol. Chem.* **2000**, *275*, 25057.

125. Banci, L.; Bertini, I.; Cantini, F.; Della-Malva, N.; Migliardi, M.; Rosato, A. *J. Biol. Chem.* **2007**, *282*, 23140.

126. Itoh, S.; Kim, H. W.; Nakagawa, O.; Ozumi, K.; Lessner, S. M.; Aoki, H.; Akram, K.; McKinney, R. D.; Ushio-Fukai, M.; Fukai, T. *J. Biol. Chem.* **2008**, *283*, 9157.

127. Anastassopoulou, I.; Banci, L.; Bertini, I.; Cantini, F.; Katsari, E.; Rosato, A. *Biochem.* **2004**, *43*, 13046.

128. Gitschier, J.; Moffat, B.; Reilly, D.; Wood, W. I.; Fairbrother, W. J. *Nat. Struct.*

Biol. **1998**, *5*, 47.

129. Banci, L.; Bertini, I.; Del Conte, R.; D'Onofrio, M.; Rosato, A. *Biochemistry* **2004**, *43*, 3396.

130. Banci, L.; Bertini, I.; Cantini, F.; Chasapis, C. T.; Hadjiliadis, N.; Rosato, A. *J. Biol. Chem*. **2005**, *280*, 38259.

131. Banci, L.; Bertini, I.; Cantini, F.; Migliardi, M.; Rosato, A.; Wang, S. *J. Mol. Biol*. **2005**, *352*, 409.

132. DeSilva, T. M.; Veglia, G.; Opella, S. J. *Proteins* **2005**, *61*, 1038.

133. Banci, L.; Bertini, I.; Cantini, F.; DellaMalva, N.; Herrmann, T.; Rosato, A.; Wuthrich, K. *J. Biol. Chem*. **2006**, *281*, 29141.

134. Banci, L.; Bertini, I.; Cantini, F.; Rosenzweig, A. C.; Yatsunyk, L. A. *Biochemistry* **2008**, *47*, 7423.

135. Achila, D.; Banci, L.; Bertini, I.; Bunce, J.; Ciofi-Baffoni, S.; Huffman, D. L. *Proc. Natl. Acad. Sci. U.S.A*. **2006** 103, 5729.

136. Pufahl, R. A.; Singer, C. P.; Peariso, K. L.; Lin, S.-J.; Schmidt, P. J.; Fahrni, C. J.; Culotta, V. C.; Penner-Hahn, J. E.; O'Halloran, T. V. *Science* **1997**, *278*, 853.

137. Wernimont, A. K.; Huffman, D. L.; Lamb, A. L.; O'Halloran, T. V.; Rosenzweig, A. C. *Nat. Struct. Biol*. **2000**, *7*, 766.

138. Holt, B. T. O.; Merz, K. M., Jr. *Biochem*. **2007**, *46*, 8816.

139. Rodriguez-Granillo, A.; Crespo, A.; Estrin, D. A.; Wittung-Stafshede, P. *J. Phys. Chem. B* **2010**, *114*, 3698.

140. (a). Figgen, D.; Rauhut, G.; Dolg, M.; Stoll, H. *Chem. Phys*. **2005**, *311*, 227. (b). K.A. Peterson, K. A.; Puzzarini, C.; *Theor. Chem. Acc*. **2005**, *114*, 283.

141. Dunning, T. H., Jr. *J. Chem. Phys*. **1989**, *90*, 1007.

142. Cotton, F. A.; Wilkinson, G. *Advanced Inorganic Chemistry 5th Edition* **1988,** 755.

APPENDIX A

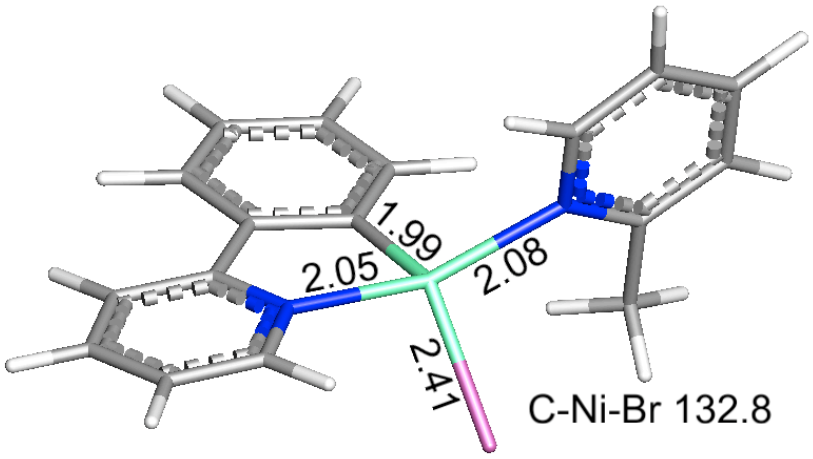

Figure A.1. The triplet state structure of complex **1**. Tetrahedral structure 18.7 kcal/mol higher in energy than the singlet state, square planar structure.

Table A.1. Relative electronic, gas phase enthalpy, gas phase free energy, and solvated free energy differences between the singlet state and triplet state of complex **11.**

	ΔE		ΔH		ΔG_{gas}		ΔG_{sol}	
Functional	**Sing**	**Trip**	**Sing**	**Trip**	**Sing**	**Trip**	**Sing**	**Trip**
BMK	17.76	0.00	18.29	0.00	19.99	0.00	19.25	0.00
B3LYP	9.65	0.00	9.41	0.00	13.86	0.00	13.36	0.00
M06	0.01	0.00	1.46	0.00	0.17	0.00	0.00	1.00
TPSS	0.00	0.60	0.00	0.59	1.15	0.00	0.61	0.00
BP86	0.00	3.73	0.00	3.58	0.00	0.86	0.00	1.38

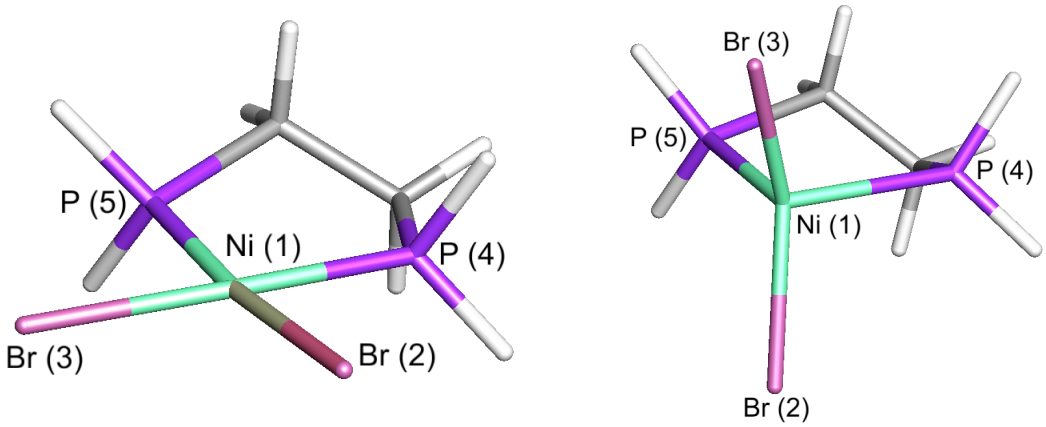

Figure A.2. The abbreviated structures from $\mathbf{11}^{S}$ and $\mathbf{11}^{T}$. The phenyl rings from the dppe ligand have been removed and replaced with hydrogen atoms.

Table A.2. Selected bond distances (Å) and angles (°) for the abbreviated models of **11** calculated with the BP86 density functional

Stuttgart basis set on Ni and Br; 6-31g* on C, H, N			
11_h^S		**11_h^T**	
Ni(1)-Br(2)	2.35	Ni(1)-Br(2)	2.34
Ni(1)-Br(3)	2.35	Ni(1)-Br(3)	2.35
Ni(1)-P(4)	2.13	Ni(1)-P(4)	2.27
Ni(1)-P(5)	2.13	Ni(1)-P(5)	2.27
P(4)-Ni(1)-P(5)	89.6	P(4)-Ni(1)-P(5)	88.8
Br(2)-Ni(1)-Br(3)	100.7	Br(2)-Ni(1)-Br(3)	142.5

Table A.3. Selected bond distances (Å) and angles (°) for the abbreviated models of **11** calculated with the BP86 density functional

6-311++g(2d,p) basis set on all atoms			
11_h^S		**11_h^T**	
Ni(1)-Br(2)	2.35	Ni(1)-Br(2)	2.32
Ni(1)-Br(3)	2.35	Ni(1)-Br(3)	2.36
Ni(1)-P(4)	2.12	Ni(1)-P(4)	2.23
Ni(1)-P(5)	2.12	Ni(1)-P(5)	2.24
P(4)-Ni(1)-P(5)	89.7	P(4)-Ni(1)-P(5)	89.0
Br(2)-Ni(1)-Br(3)	101.9	Br(2)-Ni(1)-Br(3)	140.8

Table A.4. Selected bond distances (Å) and angles (°) for the abbreviated models of **11** calculated at the MP2 level of theory

Stuttgart basis set on Ni and Br; 6-31g* on C, H, N			
11_h^S		**11_h^T**	
Ni(1)-Br(2)	2.25	Ni(1)-Br(2)	2.34
Ni(1)-Br(3)	2.25	Ni(1)-Br(3)	2.36
Ni(1)-P(4)	1.98	Ni(1)-P(4)	2.41
Ni(1)-P(5)	1.98	Ni(1)-P(5)	2.41
P(4)-Ni(1)-P(5)	90.8	P(4)-Ni(1)-P(5)	85.7
Br(2)-Ni(1)-Br(3)	99.5	Br(2)-Ni(1)-Br(3)	144.5

Table A.5. Selected bond distances (Å) and angles (°) for the abbreviated models of **11** calculated at the MP2 level of theory

6-311++g(2d,p) basis set on all atoms			
11_h^S		**11_h^T**	
Ni(1)-Br(2)	2.26	Ni(1)-Br(2)	2.33
Ni(1)-Br(3)	2.26	Ni(1)-Br(3)	2.37
Ni(1)-P(4)	1.93	Ni(1)-P(4)	2.39
Ni(1)-P(5)	1.93	Ni(1)-P(5)	2.39
P(4)-Ni(1)-P(5)	90.5	P(4)-Ni(1)-P(5)	85.6
Br(2)-Ni(1)-Br(3)	102.6	Br(2)-Ni(1)-Br(3)	146.0

Table A.6. Electronic energy for the abbreviated models of **11** with the geometry calculated with the BP86 functional or MP2 level of theory (kcal/mol)

Stuttgart basis set on Ni and Br; 6-31g* on C, H, N		
Structure	**BP86**	**MP2**
11_h^S	0.00	11.93
11_h^T	3.73	0.00

Table A.7. Electronic energy for the abbreviated models of **11** with the geometry calculated with the BP86 functional or MP2 level of theory (kcal/mol)

6-311++g(2d,p) basis set on all atoms		
Structure	**BP86**	**MP2**
11_h^S	0.00	0.00
11_h^T	10.21	8.67

Table A.8. Electronic energy values for HF, MP2, MP3, CCSD, CCSD(T), MP4(SDTQ) single point calculations with geometries calculated from BP86 (kcal/mol)

BP86 Geometry(Stuttgart basis set on Ni and Br, 6-31g* on C, H, N)						
Structure	**HF**	**MP2**	**MP3**	**CCSD**	**CCSD(T)**	**MP4(SDTQ)**
11_h^S	80.37	16.34	46.81	17.20	8.61	0.00
11_h^T	0.00	0.00	0.00	0.00	0.00	1.00

Table A.9. Electronic energy values for HF, MP3, CCSD, CCSD(T), MP4(SDTQ) single point calculations with geometries calculated from MP2 (kcal/mol)

MP2 Geometry(Stuttgart basis set on Ni and Br, 6-31g* on C, H, N)						
Structure	**HF**	**MP2**	**MP3**	**CCSD**	**CCSD(T)**	**MP4(SDTQ)**
11_h^S	123.4	11.93	71.90	33.27	23.41	0.00
11_h^T	0.00	0.00	0.00	0.00	0.00	9.33

Table A.10. Electronic energy values for HF, MP2, MP3, CCSD, CCSD(T), MP4(SDTQ) single point calculations with geometries calculated from BP86 (kcal/mol)

	BP86 Geometry(6-311++g(2d,p) on all atoms)					
Structure	**HF**	**MP2**	**MP3**	**CCSD**	**CCSD(T)**	**MP4(SDTQ)**
11_h^S	73.83	1.04	41.60	9.32	0.00	0.00
11_h^T	0.00	0.00	0.00	0.00	0.78	20.29

Table A.11. Electronic energy values for HF, MP3, CCSD, CCSD(T), MP4(SDTQ) single point calculations with geometries calculated from MP2 (kcal/mol)

	MP2 Geometry(6-311++g(2d,p) on all atoms)					
Structure	**HF**	**MP2**	**MP3**	**CCSD**	**CCSD(T)**	**MP4(SDTQ)**
11_h^S	134.50	0.00	81.39	34.21	21.15	0.00
11_h^T	0.00	8.67	0.00	0.00	0.00	37.42

APPENDIX B

Table B.1. Scaled Free Energies and Rate Constants For the CpRh(CO)-Cyclopentane Reaction

	CpRh(CO)-Cyclopentane			
	$\Delta G_{forward}$	$\Delta G_{reverse}$	$k_{forward}$	$k_{reverse}$
A + B => C	5.09		1.15E+09	
C => Z	5.94		2.73E+08	

Table B.2. Scaled Free Energies and Rate Constants For the CpRh(CO)-Cyclohexane Reaction

	CpRh(CO)-Cyclohexane			
	$\Delta G_{forward}$	$\Delta G_{reverse}$	$k_{forward}$	$k_{reverse}$
A + B <=> C	4.99			
A + B <=> D	4.99			
C <=> D	0.95	0.83	1.25E+12	1.53E+12
C <=> C	12.00	12.00	9.77E+03	9.77E+03
D <=> D	7.97	7.97	8.84E+06	8.84E+06
C => Z	6.97			
D => Z	6.52			

Table B.3. Scaled Free Energies and Rate Constants For the CpRh(CO)-Cycloheptane Reaction

	CpRh(CO)-Cycloheptane			
	$\Delta G_{forward}$	$\Delta G_{reverse}$	$k_{forward}$	$k_{reverse}$
A + B => C	5.04		1.25E+09	
A + B => D	5.04		1.25E+09	
A + B => E	5.04		1.25E+09	
A + B => F	5.04		1.25E+09	
A + B => G	5.04		1.25E+09	
A + B => H	5.04		1.25E+09	
A + B => I	5.04		1.25E+09	
C <=> G	0.00	0.00	6.21E+12	6.21E+12
H <=> D	0.99	1.06	1.17E+12	1.04E+12
I <=> E	0.00	0.00	6.21E+12	6.21E+12
F <=> G	7.72	7.54	1.35E+07	1.83E+07
F <=> J	8.06	4.52	7.59E+06	3.00E+09
D <=> J	9.03	6.02	1.47E+06	2.38E+08
C <=> K	10.19	7.34	2.08E+05	2.56E+07
D <=> L	8.37	5.24	4.50E+06	8.89E+08
K <=> I	5.34	8.15	7.51E+08	6.52E+06
I <=> L	8.16	4.79	6.41E+06	1.90E+09
F <=> D	7.58	7.14	1.71E+07	3.59E+07
C <=> E	7.33	7.19	2.61E+07	3.30E+07
D <=> C	7.06	7.34	4.11E+07	2.56E+07
D <=> I	7.69	7.93	1.42E+07	9.46E+06
C => Z	6.88		5.57E+07	
D => Z	7.11		3.78E+07	
E => Z	7.02		4.40E+07	
F => Z	7.18		3.36E+07	
G => Z	6.95		4.95E+07	
H => Z	7.26		2.93E+07	
I => Z	7.46		2.09E+07	

Table B.4. Scaled Free Energies and Rate Constants For the CpRh(CO)-Cyclooctane Reaction

	CpRh(CO)-Cyclooctane			
	$\Delta G_{forward}$	$\Delta G_{reverse}$	$k_{forward}$	$k_{reverse}$
A + B => C	5.37		7.14E+08	
A + B => D	5.37		7.14E+08	
A + B => E	5.37		7.14E+08	
A + B => F	5.37		7.14E+08	
A + B => G	5.37		7.14E+08	
A + B => H	5.37		7.14E+08	
A + B => I	5.37		7.14E+08	
A + B =>J	5.37		7.14E+08	
A + B => K	5.37		7.14E+08	
A + B => L	5.37		7.14E+08	
G <=> H	0.02	0.04	6.00E+12	5.81E+12
J <=> I	1.04	1.11	1.07E+12	9.52E+11
L <=> K	1.12	1.89	9.37E+11	2.55E+11
F <=> E	1.82	1.45	2.87E+11	5.36E+11
D <=> C	0.00	0.00	6.21E+12	6.21E+12
L <=> N	8.23	4.69	5.70E+06	2.25E+09
N <=> G	6.10	10.32	2.08E+08	1.67E+05
N <=> H	4.30	8.53	4.35E+09	3.43E+06
J <=> M	8.74	5.40	2.41E+06	6.79E+08
F <=> O	8.70	5.18	2.58E+06	9.84E+08
E <=> M	7.81	5.12	1.16E+07	1.09E+09
D <=> E	7.90	7.31	9.95E+06	2.69E+07
L <=> G	7.20	7.88	3.24E+07	1.03E+07
C <=> I	7.18	8.64	3.36E+07	2.85E+06
C => Z	9.96		3.07E+05	
D => Z	7.58		1.71E+07	
E => Z	6.96		4.87E+07	
F => Z	6.74		7.06E+07	
G => Z	8.51		3.55E+06	
H => Z	6.58		9.25E+07	
I => Z	8.32		4.89E+06	
J => Z	7.57		1.74E+07	
K => Z	7.42		2.24E+07	
L => Z	6.88		5.57E+07	

Table B.5. Scaled Free Energies and Rate Constants For the Cp*Rh(CO)-Cyclopentane Reaction

	Cp*Rh(CO)-Cyclopentane			
	$\Delta G_{forward}$	$\Delta G_{reverse}$	$k_{forward}$	$k_{reverse}$
A + B => C	5.58		5.01E+08	
C => Z	5.74		3.82E+08	

Table B.6. Scaled Free Energies and Rate Constants For the Cp*Rh(CO)-Cyclohexane Reaction

	Cp*Rh(CO)-Cyclohexane			
	$\Delta G_{forward}$	$\Delta G_{reverse}$	$k_{forward}$	$k_{reverse}$
A + B <=> C	5.34			
A + B <=> D	5.34			
C <=> D	2.89	2.80	4.71E+10	5.48E+10
C <=> C				
D <=> D	7.07	7.07	4.04E+07	4.04E+07
C => Z	7.10		3.84E+07	
D => Z	6.45		1.15E+08	

Table B.7. Scaled Free Energies and Rate Constants For the Cp*Rh(CO)-Cycloheptane Reaction

	Cp*Rh(CO)-Cycloheptane			
	$\Delta G_{forward}$	$\Delta G_{reverse}$	$k_{forward}$	$k_{reverse}$
A + B => C	5.380		7.02E+08	
A + B => D	5.380		7.02E+08	
A + B => E	5.380		7.02E+08	
A + B => F	5.380		7.02E+08	
A + B => G	5.380		7.02E+08	
A + B => H	5.380		7.02E+08	
A + B => I	5.380		7.02E+08	
C <=> G	1.91	1.91	2.47E+11	2.47E+11
H <=> D	2.39	1.56	1.10E+11	4.45E+11
I <=> E	0.50	0.70	2.67E+12	1.90E+12
F <=> G	8.47	8.29	3.80E+06	5.15E+06
F <=> J	9.14	4.50	1.22E+06	3.10E+09
D <=> J	7.56	4.75	1.77E+07	2.03E+09
C <=> K	10.44	6.10	1.36E+05	2.08E+08
D <=> L	7.36	4.20	2.48E+07	5.15E+09
K <=> I	3.89	7.57	8.70E+09	1.74E+07
I <=> L	7.67	4.41	1.47E+07	3.61E+09
F <=> D	8.96	7.14	1.66E+06	3.59E+07
C <=> E	7.64	7.82	1.54E+07	1.14E+07
D <=> C	7.79	8.54	1.20E+07	3.37E+06
D <=> I	8.44	8.68	4.00E+06	2.66E+06
C => Z	6.59		9.09E+07	
D => Z	7.63		1.57E+07	
E => Z	7.81		1.16E+07	
F => Z	7.90		9.95E+06	
G => Z	7.11		3.78E+07	
H => Z	7.93		9.46E+06	
I => Z	7.31		2.69E+07	

Table B.8. Scaled Free Energies and Rate Constants For the Cp*Rh(CO)-Cyclooctane Reaction

	Cp*Rh(CO)-Cyclooctane			
	$\Delta G_{forward}$	$\Delta G_{reverse}$	$k_{forward}$	$k_{reverse}$
A + B => C	5.70		4.09E+08	
A + B => D	5.70		4.09E+08	
A + B => E	5.70		4.09E+08	
A + B => F	5.70		4.09E+08	
A + B => G	5.70		4.09E+08	
A + B => H	5.70		4.09E+08	
A + B => I	5.70		4.09E+08	
A + B =>J	5.70		4.09E+08	
A + B => K	5.70		4.09E+08	
A + B => L	5.70		4.09E+08	
G <=> H	0.01	0.01	6.11E+12	6.11E+12
J <=> I	2.50	2.39	9.10E+10	1.10E+11
L <=> K	3.46	2.24	1.80E+10	1.41E+11
F <=> E	1.77	0.94	3.12E+11	1.27E+12
D <=> C	0.79	0.41	1.64E+12	3.11E+12
L <=> N	8.96	4.54	1.66E+06	2.90E+09
N <=> G	4.73	9.49	2.10E+09	6.78E+05
N <=> H	3.61	9.37	1.40E+10	8.30E+05
J <=> M	7.60	4.16	1.65E+07	5.51E+09
F <=> O	8.15	2.92	6.52E+06	4.48E+10
E <=> M	6.18	2.65	1.82E+08	7.06E+10
D <=> E	7.63	7.70	1.57E+07	1.39E+07
L <=> G	6.82	7.17	6.17E+07	3.41E+07
C <=> I	7.75	8.01	1.28E+07	8.26E+06
C => Z	11.07		4.70E+04	
D => Z	7.38		2.39E+07	
E => Z	7.21		3.19E+07	
F => Z	6.91		5.30E+07	
G => Z	7.53		1.86E+07	
H => Z	8.02		8.12E+06	
I => Z	8.48		3.73E+06	
J => Z	8.03		7.99E+06	
K => Z	6.32		1.43E+08	
L => Z	8.02		8.12E+06	

APPENDIX C

Table C.1. Single Point ωB97XD//B97D Electronic Energies for the Axial and Equatorial Mechanisms

Axial Mechanism		Equatorial Mechanism	
Structure	**ΔE**	**Structure**	**ΔE**
1	0.00	**1**	0.00
2^{A-TS}	8.41	**2^{E-TS}**	0.68
3^{A}	5.28	**3^{E}**	-0.16
		4^{E-TS}	0.85
		5^{E}	0.60
4^{A-TS}	6.61	**6^{E-TS}**	1.20
5^{A}	6.54	**7^{E}**	-0.60
6^{A-TS}	28.84	**8^{E-TS}**	21.34
7^{A}	12.51	**9^{E}**	14.74
Separated Products	28.12	**Separated Products**	28.12
10b	0.76	**10b**	0.76

APPENDIX D

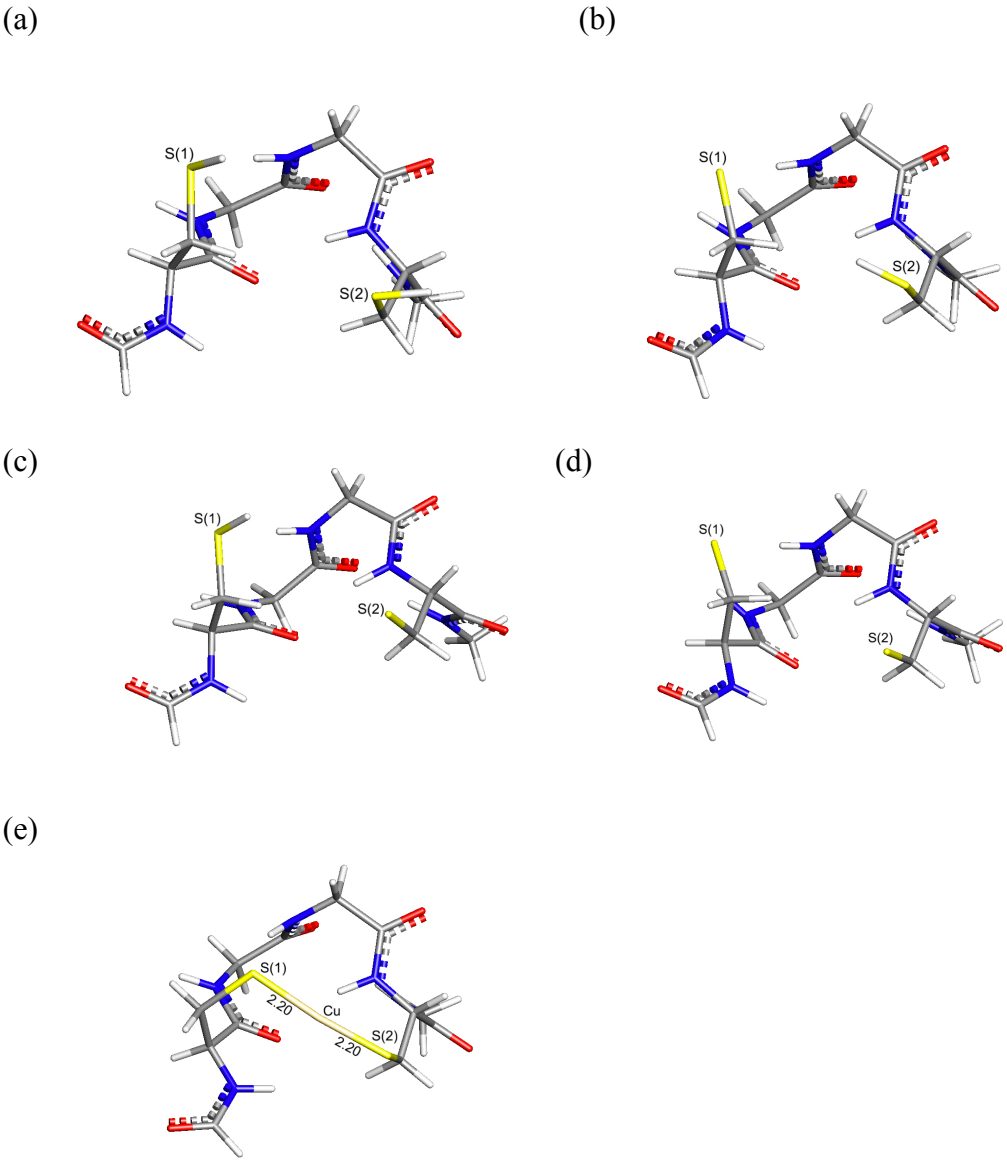

Figure D.1. Calculated geometries for the CGGC residue fragment from the Atox1 binding site. (a) Fully protonated, singlet; (b) S(2) deprotonated, anionic singlet; (c) S(1) deprotonated, anionic singlet; (d) Fully deprotonated, doubly anionic singlet; (e) Cu(I) with doubly anionic binding site, overall anionic, singlet.

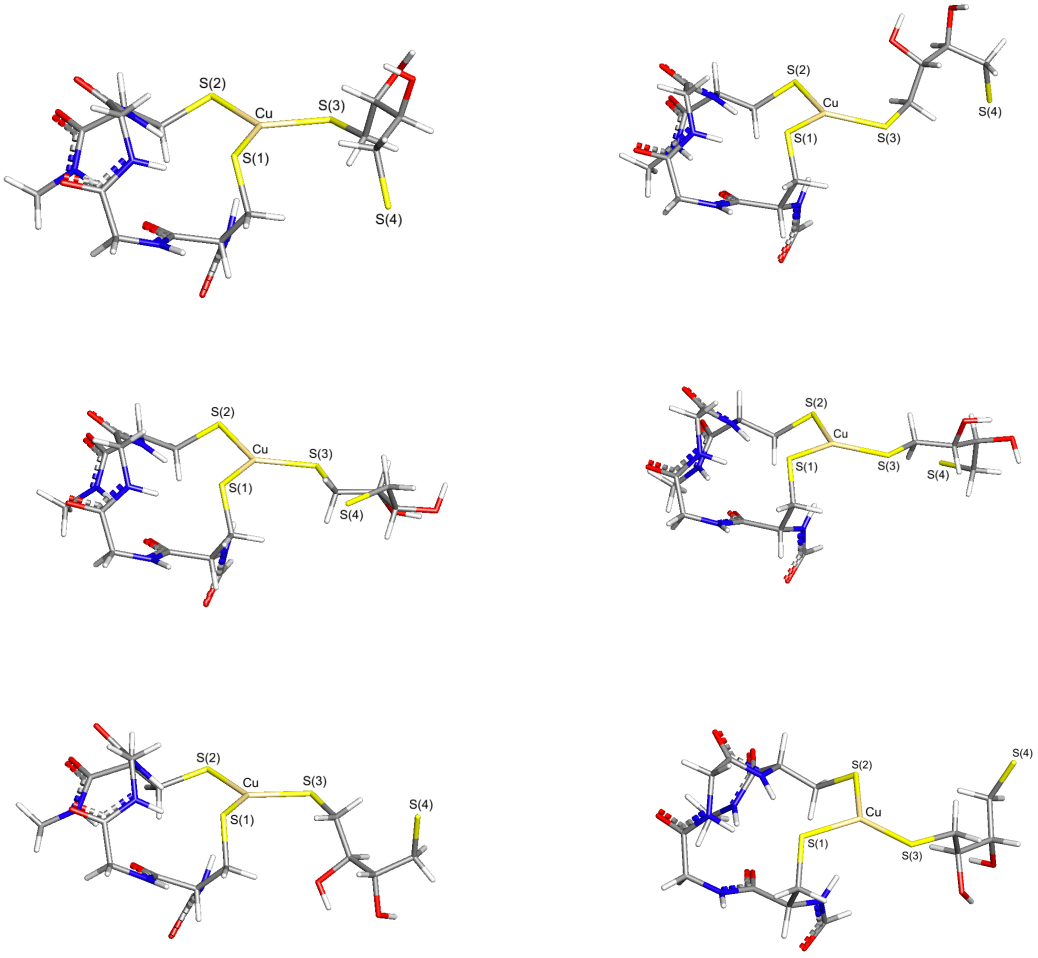

Figure D.2. Six optimized confirmations of intermediate **1** due to the rotation of the DTT about the Cu-S(3) bond and the S(3)-C bond. The rotation of the Cu-S(3) bond forms two stable geometries, both with a C-S(3)-Cu-S(2) dihedral angle of ~0°. The rotation of the S(3)-C bond forms four more stable geometries as the ligand rotates around the sp^3 carbon.